

TOOL WEAR STUDY IN TURNING TI-6AL-4V AND EDGE TRIMMING OF CARBON
FIBER REINFORCED PLASTICS (CFRP)

By

Ryan Muhammad Khawarizmi

A DISSERTATION

Submitted to
Michigan State University
in partial fulfillment of the requirements
for the degree of

Mechanical Engineering – Doctor of Philosophy

2022

ABSTRACT

TOOL WEAR STUDY IN TURNING TI-6AL-4V AND EDGE TRIMMING OF CARBON FIBER REINFORCED PLASTICS (CFRP)

By

Ryan Muhammad Khawarizmi

Lightweight materials such as titanium alloys and carbon fiber reinforced plastics (CFRP) are highly desirable due to their low density and high strength properties for many aerospace, chemical, petroleum, automotive, and sports applications. However, both materials are considered difficult to machine due to various factors.

In machining titanium alloys, the low thermal conductivity and highly reactive nature of titanium with cutting tools cause the temperature to rise quickly, producing a segmented or “saw-tooth” chip. Chip segmentation caused a periodic loading on the tool and affected the cutting process. Ti-6Al-4V depending on the heat treatment, produces four distinct types, elongated (ELO), mill-annealed (MIL), solution treated and aged (STA), and lamellar (LAM). In this dissertation, four different microstructures of Ti64, ELO, MIL, STA, and LAM, are machined at 61, 91, and 122 m/min. The machining chips were collected and characterized to study the impact of the microstructure. In addition, the crater wear for different types of Ti64 was measured and compared.

A finite element numerical simulation was developed using the chip morphology measured, which enables estimating the cutting temperature for Ti64-STA. Electron backscatter images of the cutting chips (EBSD) and crater wear surfaces were also analyzed to verify the wear mechanism. The findings suggested a high interface temperature during cutting enables faster tool diffusion. Another machinability study of turning Ti64-STA using a variety of coated tools was conducted. The coated tool materials include TiAlN, AlTiN, AlMgB₁₄(BAM), ZrN, and

(AlCrSi/Ti)N. The performance of these cutting tools was assessed using cutting force data, flank wear, and crater wear measurements. In conjunction with the coating experiments, another machining study was conducted in minimum quantity lubrication (MQL) using oil mixed with solid additives such as hBN, WS₂, MoS₂, and xGnP.

For CFRP, the abrasion from the fibers was the leading cause of tool wear. Three distinctly different types of CFRPs with T300 PAN-based carbon fibers as standard modulus (SM), IM-7 PAN-based carbon fibers as intermediate modulus (IM), and K13312 pitch-based carbon fibers as high modulus (HM) are used. Tool wear during the edge-trimming process of three types of CFRP laminates is analyzed for four different ply angles, namely 0°, 45°, 90°, 135°, to investigate the interactions between the fiber type and the fiber orientation.

.

To my beloved family...

ACKNOWLEDGMENTS

First, I am deeply indebted to my advisor Prof. Patrick Kwon. The long and winding road to accomplishing a Ph.D. would not be possible without his endless guidance, support, and patience. I am also sincerely thankful to the committee members of this dissertation: Prof. Yang Guo, Prof. Tom Bieler, and Prof. Himanshu Sahasrabudhe. They provided valuable input for my research and access to many different pieces of equipment.

Secondly, I would like to appreciate many different collaborators highly. Mr. Lars Haubold & Mr. Michael Petzold from Fraunhofer CCD graciously assisted us with the PVD coating of various carbide tools and allowed us to use a lot of their equipments. Prof. Dave Kim from Washington State University, with his students Sayem & Yinyin, for the collaboration in the CFRP project. The support from Mike, Roy, & Jon from the ME Machine Shop was essential for our daily experiments throughout the years.

It takes a “village” to survive graduate school. The sense of camaraderie, insightful discussions, and encouragement from fellow grad students has been highly influential for the past four years. I want to give my appreciation to Dr. Dinh Nguyen, Juan Sandoval, Jiawei Lu, Jisheng Chen, Melih Yesili, Amr Saleh, Aaqib Ali, Bibek Poudel, Hoa Nguyen, Darshan Thakkar, Tyler Bauder, Jack Song, Hawke Suen, and many others that I cannot mention them all.

My deepest gratitude goes to my parents, Yandra & Titi, my Opa-Arkeman, my in-laws, Syafriman & Euis, and all my families in Indonesia for believing in me and supporting from afar. They always reminded me to be patient and keep pushing through difficulties. Finally, I want to thank my wife, Astri Briliyanti, for keeping me motivated throughout the tough years by providing stability & happiness in my life.

TABLE OF CONTENTS

LIST OF TABLES	viii
LIST OF FIGURES	x
CHAPTER 1: LITERATURE REVIEW	1
1.1 Machining of Ti-6Al-4V	1
1.2 Chip Segmentation in Machining Titanium Alloys	7
1.3 Temperature Increase during Machining Titanium Alloys	8
1.4 Coated Tools for Machining Titanium Alloys	9
1.5 Minimum Quantity Lubrication for Machining Titanium Alloys	10
1.6. Edge Trimming of Carbon Fiber Reinforced Plastics	12
1.7. Organization of Dissertation	15
CHAPTER 2: TOOL WEAR AND CHIP SEGMENTATION OF DIFFERENT TYPES OF TI-6AL-4V	17
2.1 Motivation	17
2.2 Experimental Setup	19
2.2.1 Turning experiments	19
2.2.2 Turning Force Measurements	20
2.2.3 Orthogonal cutting experiments	21
2.2.4 Chip Mounting	22
2.2.5 Crater Wear Measurements	22
2.3 Results	24
2.3.1 Chip Morphology	24
2.3.2 Crater Wear	30
2.3.3 Measured Cutting Force	32
2.4 Discussions	34
2.5 Conclusions	38
CHAPTER 3: COMPARISON BETWEEN EXPERIMENTAL AND FINITE ELEMENT ANALYSIS ON TURNING OF TI64-SOLUTION TREATED AND AGED (STA)	40
3.1 Motivation	40
3.2 Experimental	40
3.2.1 Work Material	40
3.2.2 Turning Experiments	41
3.2.3 Electron Microscopy	43
3.2.4 Finite Element Analysis	44
3.3 Results	47
3.3.1 Chip Morphology Analysis	47
3.3.2 Wear Measurements	48
3.3.3 Finite Element Method Results	49
3.3.4 Electron Backscattered Diffraction (EBSD) Analysis	52

3.4 Discussion.....	53
3.5 Conclusions.....	58
CHAPTER 4: A MACHINABILITY STUDY OF COATED INSERTS DURING THE MACHINING OF TI-6AL-4V SOLUTION TREATED AND AGED	60
4.1 Motivation.....	60
4.2 Experimental Setup.....	61
4.3 Wear Measurement	64
4.4 Results.....	66
4.4.1 Cutting Force	67
4.4.2 Tool Wear	68
4.5 Discussion.....	72
4.6 Conclusions.....	80
CHAPTER 5: MINIMUM QUANTITY LUBRICATION (MQL) USING DIFFERENT SOLID ADDITIVES OR MACHINING TI64-STA.....	82
5.1 Motivation.....	82
5.2 Experimental.....	82
5.3 Results & Discussions	86
5.4 Conclusions.....	91
CHAPTER 6: THE EFFECT OF CARBON FIBER TYPES ON TOOL WEAR DURING EDGE TRIMMING OF 0°, 45°, 90°, AND 135° CARBON FIBER REINFORCED PLASTIC LAMINATES	92
6.1. Experimental.....	92
6.1.1 Workpiece Materials	92
6.1.2 Experimental Set-up.....	94
6.1.3 Tool wear evaluation methods	96
6.2 Results and Discussions.....	98
6.2.1 Tool wear measurements by digital light microscope	98
6.2.2 Tool wear and machined CFRP surface investigations by SEM & Roughness.....	102
6.3. Conclusions.....	109
APPENDICES	111
APPENDIX A – Histogram of the Segmentation Distance in Ti64.....	112
APPENDIX B – Cooling Rate in Turning Ti64-ELO	114
APPENDIX C – Matlab Code For Tensor Calculation [93].....	115
BIBLIOGRAPHY.....	120

LIST OF TABLES

Table 1. Comparison between 3 different commonly used aerospace materials from [5][6][7], [8]	1
Table 2. Mechanical properties of four different Ti64 microstructures from [4]	3
Table 3. Details of The Cutting Tools Geometry	20
Table 4. ELO, MIL, STA, and LAM etched chip captured at 50x	24
Table 5. Measured chip morphologies for Ti64: Average segmentation length (d) and its standard deviation (s_d); Average valley height (h1) and its standard deviation (s_{h1}), Average peak height (h2) and its standard deviation (s_{h2}); Average shear angle (ϕ) and its standard deviation (s_ϕ)	29
Table 6. Average force and standard deviation during turning of Ti64 MIL, STA, and LAM	32
Table 7. Average force and standard deviation during orthogonal cutting of Ti64 ELO, MIL, STA, and LAM	33
Table 8. The average constituent grain size in different microstructure of Ti64 [11]	37
Table 9. Material and Chemical Properties of Ti64-MIL and Ti64-STA [12]	41
Table 10. Material Constants and Parameters for Johnson Cook material model of Ti64-STA ..	45
Table 11. Summary of Maximum Temperature and Effective Strain from FEA Simulation.....	51
Table 12. Uncoated And Coated Inserts Layer Thickness.....	63
Table 13. Crater Wear Rate at Different Cutting Speeds.....	77
Table 14. Room Temperature Hardness of Various Coating Materials and Substrate	78
Table 15. Solubility Limit at Different Cutting Speeds. (*) means the element is fully soluble in Ti.	78
Table 16. Wear Rates of Different Coating Materials at 122 m/min and 1000°C	80
Table 17. Experimental Details.....	83
Table 18. Solid additives (platelets) mixed with oil	85
Table 19. Properties of each carbon fiber type and its CFRP laminate used for the experiments	94

Table 20. End mill dimensions 95

LIST OF FIGURES

Figure 1. Hexagonal Closed Package (HCP) and Body-Centered Cubix (BCC) crystal structures[10]	2
Figure 2. Different Ti64 Microstructures alpha dark grains, beta white grains, lamellar is a colony of alpha and beta [11].....	2
Figure 3. Heat treatments used to obtain different Ti64 grades [12]......	3
Figure 4. Schematic of typical tool wear modes in machining.....	5
Figure 5. The hardness in the alpha grain as the function of the declination angle (gamma), adapted from [17].....	5
Figure 6. Titanium segmented chip at the cutting speed of 3.8 sfm (surface feet per minute) [25]7	
Figure 7. Typical cross-ply CFRP laminates (0/90 and 45/35)	12
Figure 8. Dissertation Chapters.....	16
Figure 9. Tool Geometry for Turning and Orthogonal Cutting Experiments.....	20
Figure 10. Experimental Setup to Measure Cutting Force and Typical Force Signal in Turning Experiments. Inset shows the three force components Fx,Fy, and Fz.....	21
Figure 11. Orthogonal Machining Setup and Typical Cutting Force Signal. Inset shows the three force components Fx,Fy, and Fz.....	21
Figure 12. Ti64 chip mounted and imaged using SEM backscatter.	22
Figure 13. A) Worn tool of Ti64-STA at 122 m/min B) Height encoded image of worn tools prior to ethching showing built-up edges (BUE) C) Height encoded image of the worn tool after etching D) processed tool profile using MATLAB E) 2-D crater wear profiles selected from D)	23
Figure 14. ELO chip at 122 m/min showing the composition of the microstructure	25
Figure 15. A) MIL chip at 91 m/min and B) STA chip at 91 m/min.....	25
Figure 16. Enlarged LAM 61 chips with highly sheared region (left) and LAM 91 chip with larger α region in the laths.	26
Figure 17. Illustration of different lamellar cluster orientation in the irregular LAM 122 chips .	26
Figure 18. Typical box plot chart of measured data points.....	27

Figure 19. Different measured chip morphology of different Ti64 from machining at different speeds A) Valley Height B) Peak Height C) Segmentation Length D) Shear Angle	28
Figure 20. Crater wear progression for LAM 61, LAM 91, and LAM 122.....	30
Figure 21. Crater wear chart for different Ti64 at A) 61 m/min B) 91 m/min and C)122 m/min	31
Figure 22. Crater wear rate at different cutting speeds for Ti64 ELO, MIL, STA, and LAM	31
Figure 23. Bar chart of average force during turning of Ti64, whiskers indicates ± 1 standard deviation of the measurements.....	32
Figure 24. Bar chart of average force during orthogonal cutting, whiskers indicates ± 1 standard deviation of the measurements.....	33
Figure 25. Friction coefficient estimated for turning Ti64 MIL, STA, and LAM.....	34
Figure 26. The difference in chip segmentation at low and high cutting speed according to Recht [25].....	35
Figure 27. Widmanstatten microstructure of secondary α grains [85]	36
Figure 28. Lamellar grains (layered α) transformed into β grains at 940°C, from [88].....	38
Figure 29. A) Uncoated tungsten carbide tool B) Severe fracture on the tool after machining Ti64-STA at 122 m/min.....	38
Figure 30. WC grains in the cutting tools.....	42
Figure 31. A) Dark field optical micrographs of etched Ti64-STA chips from 61, 91, and 122 m/min and metrics that characterize morphology. (B) Measured experimental and simulation chip morphology parameters: d, h1, and h2. Number of sample serrations measured: experimental, n=100; simulation, n= 4.(C) Measured shear angle, frequency, and compressed chip ratio.	43
Figure 32. (A) Crater wear image after fracture when cutting STA at 122 m/s, white dotted line indicates the chip flow during machining; (B) 2-D profile of crater wear progression for MIL and STA at 122 m/s at different cutting lengths, with a schematic of chip formation and identification of cutting force directions in the cutting zone; (C) Crater wear at different cutting speeds for MIL and STA	44
Figure 33. (A) Flow stress of Ti64-STA & Ti64-MIL calculated by modified JC model at 700 °C; (B) Measured experimental and simulated cutting force at different speeds	47
Figure 34. (A) Temperature field and (B) Effective strain in the Ti64-STA chip and tool with 1.2 mm depth of cut at 122 m/min, (C) values along marked elements and overlaid experimental crater wear profile at 122 m/min and 201 m cut length, (D) Strain field of Ti64-STA chip along marked elements	49

Figure 35. Shear Stress Field (σ_{xy}) in Turning Ti64-STA at 122 m/min (left) and The corresponding stress tensor inside the chip (right)	51
Figure 36. Experimental Chip for Ti64-STA at 122 m/min cutting obtained near tool fracture ..	52
Figure 37. Backscattered electron image of Ti64-STA chip obtained at 122 m/min, showing the contrast of primary α (darker phase) and lamellar transformed β (brighter regions); (B) EBSD scan of the light green dashed boxed area shown in (A) revealing the α phase; (C) Grain reference orientation deviation (GROD) map showing orientation difference from the average α grain orientation	53
Figure 38. Experimental and Predicted Crater Wear Rate for Ti64-MIL and Ti64-STA.....	55
Figure 39. Diffusivity of Tool Constituents (W,C, and Co) in Titanium	56
Figure 40. SEM images at 80x, 2000x for Ti64-STA at 122 m/min. With Elemental detection for Ti, W, and Co.....	58
Figure 41. SEM images and quantitative element results for particles attached to the chip	58
Figure 42. SEM Images at 10000x showing crater face of the carbide tool at different cutting speed	58
Figure 43. (A) Multilayer (AlCrSi/Ti)N Coating (B) Nanocomposite Structure of AlCrSiN layer	63
Figure 44. SEM image of the cross section of the coated tool and energy dispersive x-ray spectroscopy signal, showing the coating thickness.....	64
Figure 45. Calote Test method [102]	64
Figure 46. Tool Wear Measurement Using 3D Confocal Images (A) HEI Images, (B) 3D Processed Surface (C) 2D Profile of Flank Wear and (D) 2D Profile of Crater Wear.....	65
Figure 47. Flank Surface Image of TiAlN Coated Insert.....	66
Figure 48. Scanning Electron Microscope Images of the MM1115 And MM1125 Coated Tool.	67
Figure 49. (A) Cutting Forces Components in Turning (B) Measured Cutting Forces of Uncoated Carbide Tool at 122 m/min.....	68
Figure 50. (A) Average Normal, Tangential, and Cutting Forces change to F_x , F_y , F_z and (B) Force Variations in F_x , F_y , and F_z for Each Coating and Cutting Speed	71
Figure 51. (A) Flank Wear And (B) Crater Wear Confocal Images of The Worn Tool After Turning Titanium Alloys for All Cutting Speeds	72
Figure 52. Flank Wear Curves of (A) 61 m/min, (B) 91 m/min, and (C) 122 m/min	75

Figure 53. Crater Wear at the Cutting Speeds of (A) 61, (B) 91, and (C) 122 m/min.....	77
Figure 54. Diffusivity data of different elements in Ti.....	78
Figure 55. Cutting Tool SCMT 12 04 08-KR H13A.....	83
Figure 56. Experimental Setup of the MQL turning(left), “bird-nest” effect from turning (right)	84
Figure 57. (AlCrSi/Ti)N Coating on the carbide tools	84
Figure 58. Scanning Electron Microscope of various additives at different magnification	85
Figure 59. Mixture stability after 72 hours (A) hBN 0.5wt% (B) WS ₂ 0.5wt% (C) MoS ₂ 0.5wt%	85
Figure 60. Average force of turning uncoated and coated tools for different lubrication	86
Figure 61. Flank face of the fresh and worn tool after machining with MoS ₂ lubrication	87
Figure 62. Confocal Images of flank wear during fracture.....	87
Figure 63. Flank wear chart for WC and AlCrSiN tools	88
Figure 64. Crater wear progression in AlCrSiN tools during dry cutting.....	88
Figure 65. Rake face of the fresh and worn tool after machining with MoS ₂ lubrication	89
Figure 66. Confocal Images of crater wear during fracture.....	89
Figure 67. Crater wear chart for WC and AlCrSiN tools	90
Figure 68. Cross section of CFRP workpieces at 0° ply angle at 50x magnification	94
Figure 69. Edge trimming setup and fiber ply orientation	96
Figure 70. (A) 3-D profile of tool cutting edge and extracted 2-D profile. (B) Three tool wear measurement methods on a 2-D tool edge profile: the flank wear land, the edge radius (the dotted circle), and the worn area (the shaded area).	97
Figure 71. Two locations of SEM investigations in a worn tool surface (A: edge rounding zone; B: the flank wear zone).....	97
Figure 72. Normalized edge radii for different plies (A) 0° (B) 45°(C) 90°(D) 135°.....	99
Figure 73. Normalized flank wear for different plies (A) 0° (B) 45°(C) 90°(D) 135°.....	100
Figure 74. Normalized worn area for different plies (A) 0° (B) 45°(C) 90°(D) 135°.....	100

Figure 75. Normalized surface roughness (Ra) for different plies (A) 0° (B) 45°(C) 90°(D) 135°	101
Figure 76. Hard and Soft Abrasion in WC tool from CFRP, adapted from [133].....	103
Figure 77. SEM images of the cutting edges for three fiber types at four different fiber orientations (20,000×; yellow arrow refers to soft abrasion (dislodged carbide grains)	104
Figure 78. SEM images of the machined CFRP surface after cutting 16 m for three fiber types at four different orientations (1000×and 5000×)	106
Figure 79. Raw surface roughness measurements at 16 m cutting distance.....	107
Figure 80. Histogram for measured segmentation distance in ELO chips	112
Figure 81. Histogram for measured segmentation distance in MIL chips	112
Figure 82. Histogram for measured segmentation distance in STA chips.....	113
Figure 83. Histogram for measured segmentation distance in LAM chips	113

CHAPTER 1: LITERATURE REVIEW

1.1 Machining of Ti-6Al-4V

Despite its desirable advantages over other metallic alloys, Ti alloys are known to be difficult-to-machine materials because the tool life is short. The cutting speed is limited to the range between 30 and 60 m/min with uncoated carbide tools [1], in contrast to cast iron which can be cut as fast as 1000 m/min [2]. One of the reasons for the poor machinability is its low thermal conductivity, as shown in Table 1. Low thermal conductivity causes heat to be trapped in the cutting zone, leading to localized high temperatures, plastic instability, high chemical reactivity, and accelerated tool wear. The extremely high temperature also causes the chip to ‘weld’ to the tool, causing increased friction and attrition [3]. Pure titanium undergoes an allotropic phase transformation at $\sim 882^{\circ}\text{C}$ [4], changing from the α – phase, hexagonal closed package (HCP) to the β -phase, Body Centered Cubic (BCC) in Figure 1. Alloying elements stabilize the α or β phase and increase phase transformation temperature. For Ti-6Al-4V, Al stabilizes the α phase, and conversely, V stabilizes the β phase.

Table 1. Comparison between 3 different commonly used aerospace materials from [5][6][7], [8]

Material	Ti-6Al-4V	Al 7075	4340 Steel
Density (g/cm^3)	4.43	2.81	7.85
Hardness (HRC)	30-36	7	17
Ultimate Tensile Strength (MPa)	950	572	745
Yield Strength (MPa)	880	503	470
Elasticity Modulus (GPa)	113.8	71.7	210
Thermal Conductivity (W/mK)	6.7	130	44.5
Fracture Toughness ($\text{Mpa m}^{1/2}$)	75	20-29	139.1

Different Ti64 alloy microstructures and mechanical properties are obtained with varying heat treatments. Four of the commonly produced Ti64 types are: fully equiaxed (ELO), mill-annealed (MIL), solution treated and aged (STA) or bi-modal, and fully lamellar (LAM) [4], [9]. The different microstructures are shown in Figure 2. The differences in the microstructure are mainly characterized by the geometrical arrangement of the two main crystal structures, hexagonal closed package (HCP or α) and body-centered cubic (BCC or β). Two standard structural arrangements are α grains in clusters and lamellar colonies, which have alternating layers of α and β . It is unknown if the different mechanical properties, as shown in Table 2, affect the machinability.

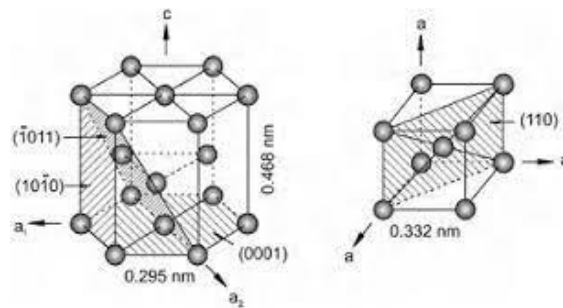


Figure 1. Hexagonal Closed Package (HCP) and Body-Centered Cubix (BCC) crystal structures[10]

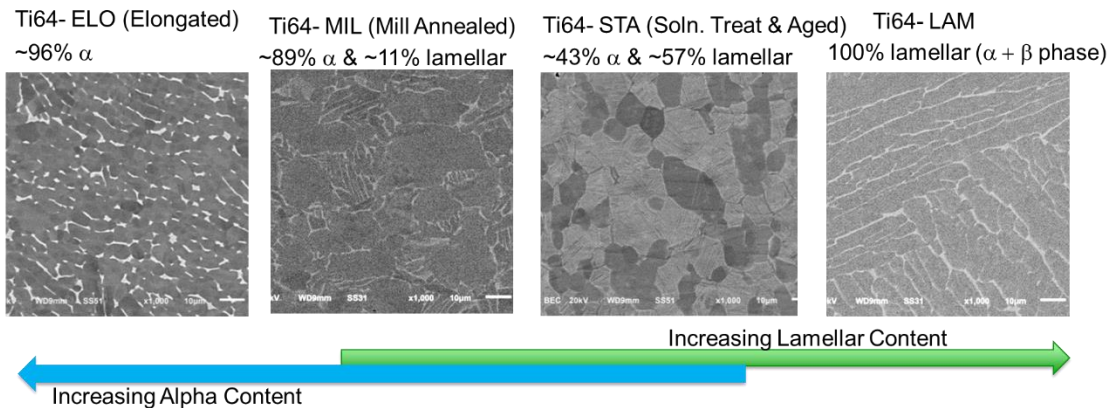


Figure 2. Different Ti64 Microstructures alpha dark grains, beta white grains, lamellar is a colony of alpha and beta [11]

Table 2. Mechanical properties of four different Ti64 microstructures from [4]

Grade	Ultimate Tensile Strength (MPa)	Tensile yield strength (MPa)	Elongation,%	Reduction of area %
Ti64-ELO	1000	931	10	25
Ti64-MIL	930	860	10	20
Ti64-STA	1270	1181	16	41.5
Ti64-LAM	990	910	11	20

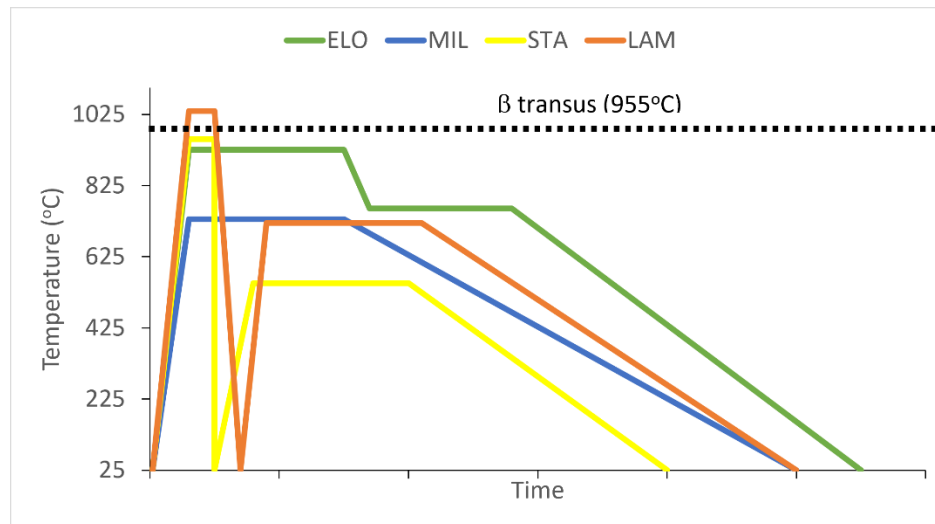


Figure 3. Heat treatments used to obtain different Ti64 grades [12].

To produce ELO, it starts with 925 °C heat treatment for 4 hours, rapid cooling to 760 °C, and air-cooled. The resulting microstructure is 96% equiaxed α phase and 4% β phase. The MIL type was processed by annealing at 730°C and then slowly cooled. MIL has equiaxed α grains (~89%) and a small fraction (~11%) of lamellar grains. Lamellar grains consist of a cluster where

the α phase is layered together with the β phase. To obtain STA microstructure, it is heated to 940°C for 1 hour (slightly below the β transus temperature). Then it is water quenched and aged at 510-550°C for 4 hours. This heat treatment yields an increased fraction of lamellar grains up to 57%.

Additionally, the width of the α phase in the lamellar grains is much thinner than in the Ti64-MIL, as the cooling rate and the aging treatment controls the width. The STA microstructure has the highest strength and ductility, as seen in Table 1. LAM was produced by heating at 1035°C, higher than the β transus temperature of 955 °C. Then it is soaked for 30 minutes, and furnace cooled at the rate of 4-5°C/min. The resulting microstructure is fully lamellar grains with an average cluster size of ~700 μm . Despite the increased lamellar content, the tensile strength of Ti64 LAM is lower than STA.

In machining titanium alloys, many different tool wear modes [13] are presented in Figure 4. Flank wear generally shows uniform worn area on the flank face, due to the abrasion and rubbing from the workpiece during machining. Conversely, the friction and temperature increase between the chip flow and the rake face is crater wear. Crater surfaces are typically smooth and indicate a chemical dissolution-diffusion process from the tool into the chip [14]. Nose wear occurs on the tool's edge via attrition or plastic deformation. In WC-Co tools, an increased cobalt content resulted in a tendency to plastically deform tools during machining [15][16]. Notch wear slightly differs from flank wear, showing isolated fractured patches on the flank face. Notch wear typically occurs in ceramic tools such as cubic boron nitride [13] or low cobalt WC tools[15].

In machining Ti alloys is that no clear hard phase or inclusions that provided abrasion causing wear like the steel cementite phase. However, a harder orientation is present in the alpha phase, as reported by Lu [17] and Britton [18] and presented in Figure 5. When indentation

directions are parallel to the crystal c-axis in the alpha phase orientation, the hardness is the highest at 7 GPa, and as the orientation declines (γ), the hardness reduces to 5 GPa.

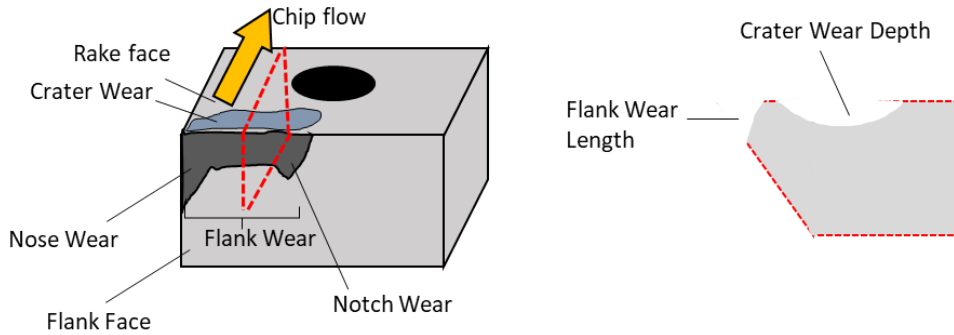


Figure 4. Schematic of typical tool wear modes in machining

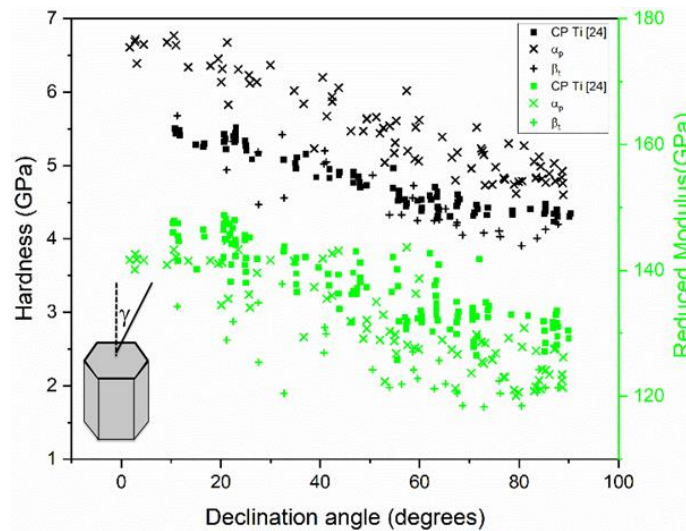


Figure 5. The hardness in the alpha grain as the function of the declination angle (γ), adapted from [17]

Nguyen *et al.* [19] conducted experiments on machining Ti64 alloys with an equiaxed microstructure with tungsten carbide and PCD tools. They found that the root causes for the flank wear in machining Ti64 are primarily due to the variety in microstructure coming from the α - grains or clusters of α -grains in the hard orientations, which abrade and fracture the cutting tools. Nguyen *et al.* [11] studied the difference in flank wear on machining Ti64 for different

microstructures (ELO, MIL, STA, and LAM). They directly linked the root causes of the flank wear to the hard α -clusters and the lamellar colonies in their respective microstructures. At a low cutting speed (61 m/min), the effect of the hard α -cluster on flank wear are similar for ELO and LAM. As the cutting speed increased, the lamellar phase became much more detrimental to flank wear. At the high cutting speed (122 m/min), the flank wear was about four times higher in the LAM sample than in the ELO and MIL samples.

Crater wear in Ti64 was extensively studied by Hartung and Kramer [14]. The steel grade tools (HfC, TiC, Al₂O₃) have a higher crater wear rate (>50 $\mu\text{m}/\text{min}$) than the uncoated carbide and diamond tools (< 3 $\mu\text{m}/\text{min}$) during turning Ti64 at cutting speed of 61 m/min. Dearnley and Grearson [15] studied the performance of cemented carbide and various ceramic tools : Al₂O₃, ZrO₂, Sialon, and CBN. They reported that the crater wear rate in turning Ti64 at 75 m/min is extremely high for the ceramic tool, more than 100 $\mu\text{m}/\text{min}$. The cemented carbide tool wear rate is 24 $\mu\text{m}/\text{min}$. Hartung and Kramer [14] found that the steel grade tool is highly soluble in titanium while the tungsten carbide tool has low solubility (0.6% wt). Additionally, the material transport rate into the chip is governed by the diffusivity of the tool elements. The smooth crater surface confirms that a dissolution-diffusion mechanism occurred at the tool rake face. At 61 m/min, there exists a TiC reaction layer, which limits the diffusion of tool into the chip material and retarded the crater wear. However, at higher cutting speeds, the reaction layer was removed. Formation of a TiC layer was also confirmed by [15], [20], [21]. Hua and Shivpuri proposed a competing theory in which cobalt diffusion is more influential in the crater wear mechanism [16]. Cobalt diffuses four orders of magnitude faster than tungsten and carbon in titanium. Their hypothesis stated that carbide grains would be removed in a brittle manner initiated by cobalt matrix leaching out of the tool. The predicted crater wear rate at different cutting speeds matched the experimental crater

wear rate trend. The study of crater wear is essential because it is widely known as a precursor to tool fracture.

1.2 Chip Segmentation in Machining Titanium Alloys

Because of the high strength of titanium alloys and its low thermal conductivity, it produces a segmented or "saw-tooth" chip geometry. This geometry then causes a periodic loading on the tool and affects the machined surface quality. There are two hypotheses regarding the formation of segmented chips. First, the thermal instability in a localized area can cause an adiabatic shear band. As reported by Komanduri, localized adiabatic heat in the primary shearing zone lowers the flow stress and leads to strain softening [22]. The other hypothesis is that segmentation is caused by crack initiation and propagation, as studied by Vyas and Shaw [23]. According to Bai and Dodd [5], an adiabatic shear band may be a precursor to fracture [24]. Recht [25] performed orthogonal machining experiments showing that Ti alloys produced segmented chips at speeds as low as 0.02 m/s, while mild steel started to show segmentation at 6.6 m/s. An instability criterion for periodic shearing in the chip was also defined as $d\tau/d\varepsilon = 0$. Childs [26] reported minimum machining parameters or chip load (hv_c), where h and v_c are the feed rate and cutting speed that produce segmented chips for different materials. The minimum chip load to initiate segmentation in Ti alloys is $70 \text{ mm}^2/\text{s}$.

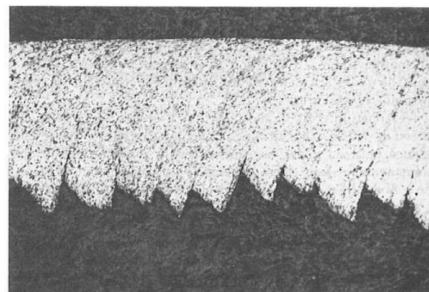


Figure 6. Titanium segmented chip at the cutting speed of 3.8 sfm (surface feet per minute) [25]

Molinari studied the behavior of adiabatic shear bands in orthogonal machining of Ti64 mill annealed (MIL) for cutting speeds up to 73 m/s using a ballistic impact setup. A relation between force, chip segmentation, and cutting speed was derived from the study in which the spacing between shear bands decreases with a cutting speed greater than 12 m/s. They also observed transformed shear bands in segmented chips at cutting speeds between 12 and 36 m/s [27]. On the other hand, Cotterel studied chip formation for Ti64 with an equiaxed microstructure and extra low interstitial composition (ELI) with orthogonal cutting at a speed between 0.06 and 2.33 m/s. They observed deformed shear bands inside the chip and that segmentation frequency and chip thickness increase with cutting speed [28]. Bayoumi performed turning experiments in Ti64-MIL with cutting speeds from 0.5 to 3.5 m/s. Based on X-ray diffraction patterns (XRD), there is evidence for transformed shear bands in the segmented chip due to the loss of β peaks after machining. This indicates that the temperature was high enough to cause phase transformation; the reduction in the β phase resulted from rapid cooling from the transus temperature [29]. Sun *et al.* studied turned Ti64 MIL at cutting speeds of 0.16 to 4 m/s and found that the segmented chip is related to the cyclic force measured. With increasing the cutting speed from 0.8-1.25 m/s, the cutting force increased as well, which was attributed to an increase in the yield stress with an increasing strain rate [30].

1.3 Temperature Increase during Machining Titanium Alloys

Dearnley performed a turning experiment on Ti64 annealed (IMI 318) and estimated that temperature could reach 900° C within 10 seconds of cutting at 75 m/min [31]. One indirect method of measuring the cutting temperature is to observe the fraction phase transformation in the iron binder (ferrite -> austenite) inside the customized carbide tool used [32]. One of the most common direct temperature techniques is to use a thermocouple, where elevated temperature is converted

into electrical potential. Li and Shih performed drilling of commercially pure (CP) titanium and measured the temperature by embedding a thermocouple externally to the drill flank face. The peak temperatures were 480°C for 24 m/min of cutting speed and 1060°C for 73.2 m/min of cutting speed [33]. Hoyne *et al.* determines by using a thermocouple in turning experiment that the temperature of Ti64 can reach up to 1300°C at cutting speed of 110 m/min with feed rate of 0.2 mm/ rev [34]. One issue with the using thermocouple for temperature measurement in machining is the cost and the complexity of the setup, as the chip formed during the machining can tangle into the sensor causing damage and faulty.

Another approach widely used to estimate the cutting temperature is the finite element method. Schrock *et. al* performed turning and finite element method (FEM) of Ti64 using tungsten carbide and polycrystalline diamond tool (PCD) and found cutting temperature can reach 1200°C at 122 m/min of cutting speed [35]. However, the FEM simulation did not account for segmented chip formation, which might reduce the cutting temperature. Calamaz *et al.* developed a new material constitutive law that introduces strain softening effect to produce shear band and chip segmentation in the Ti64 MIL chip formation simulation. The simulation produced a peak temperature 700 °C for 180 m/min of cutting speed [36]. The simulation used a mixed-mode friction model with a low Coulomb friction coefficient of 0.3. Hence, the estimated temperature was lower than other experimental titanium machining temperatures. The modified material model which can yield segmented chip formation was also used in [37]–[40].

1.4 Coated Tools for Machining Titanium Alloys

Coated carbide tools have been extensively used to improve the tool life of ferrous alloys since 1970. The coating materials have been improved since then and have significantly impacted the machining of various ferrous alloys. Some advanced coatings have been used for difficult-to-

machine alloys including Ti alloys. Dearnley et al.[41] reported that the tungsten boride (WB) coating reduced crater wear by about 20% when cutting commercially pure (CP) titanium at 200 m/min due to its high strength and chemical inertness. Perez et al. used high speed steel tools coated with TiCN for milling on Ti-6Al-4V alloys at 51 m/min, and the coating prolonged the tool life by 12% compared to uncoated carbide tools [42]. Jaffrey et al. [43] conducted turning experiments on Ti alloys with uncoated and various coated carbide tools including NbN, AlCrN (Alcrona), and Ti₆Al at cutting speeds of 50, 75, 100, and 150 m/min. Alcrona-based coatings performed 16-25% better than the uncoated carbide well at 75 and 100 m/min. In comparison, Ti₆Al coating worked 20% better at 150 m/min due to the stabilization of a titanium aluminide layer that protects the tool. Liu et al. [44] reported the performance of uncoated carbide and two nano-composite coated (AlTiN/Si₃N₄ and AlCrN/Si₃N₄) carbides after turning Ti-6Al-4V alloys at 120 m/min. The thicknesses for these coatings were between 1 and 4 μm for AlTiN/Si₃N₄ and between 1 and 7 μm for AlCrN/Si₃N₄. The AlTiN/Si₃N₄ tools performed 50% better in terms of tool life than the uncoated carbide. Park & Kwon reported that BAM (compound of Boron, Aluminum, Magnesium) coating prevents titanium adhesion on carbide tool in drilling a stack of CFRP (Carbon Fiber Reinforced Plastic)/Ti material [45]. Next, Nguyen *et.al* [46] compared three different coatings, DLC (diamond-like carbon), nanocomposite (AlCrSi/Ti)N and BAM, to drill Ti-6Al-4V plate at 800 rpm. BAM was the most wear resistant coating allowing to drill more holes in the titanium plates.

1.5 Minimum Quantity Lubrication for Machining Titanium Alloys

Minimum quantity lubrication (MQL), is a technique to apply a miniscule amount of lubricant into the cutting zone during machining to reduce friction and improve machinability [47]. It is highly desirable to use MQL instead of traditional flood cooling due to the lower cost, reduced

pollution, and reduced health risk for the user [48]. MQL has been used in machining steels [49][50], nickel-based alloys [51], [52], and titanium alloys.

Nguyen [53] reported on milling, enhanced by MQL of Ti64 by mixing oil with exfoliated graphite nanoplatelets or xGnP. 1% of xGnP c750 addition to the oil increased the tool life. However, MQL is only effective at a low speed of 55 m/min. At 77 m/min, the MQL performance is less significant due to oil dissociation at high cutting temperatures. Gupta [54] performed MQL for the turning process of commercially pure titanium (grade 2) using a cubic boron nitride tool with three additives in vegetable oil: nano-scale graphite, MoS₂, or Al₂O₃. The graphite-based nano-fluids achieved the best surface finish and minimal tool wear. The heat-carrying capacity of graphite is higher than other powders, reducing the cutting temperature.

Sartori *et al.* [55] turned Ti64 with extra low interstitial atoms (ELI) using a TiAlN-coated carbide tool. MQL combination of oil and PTFE particles (polytetrafluoroethylene) was used and compared with minimum quantity cooling (MQC). MQC is a water-based coolant mixed with graphite particles. MQC yields the lowest crater and longer tool life, while MQL reduced the nose wear. Nguyen *et al.* [56] used MQL for turning Ti64-STA using uncoated tungsten carbide with the addition of xGnP at varying concentration and nozzle positions. They evaluated the tool's flank and crater wear during different cutting conditions. The results show xGnP at 0.5% wt, and a certain nozzle position (at rake face with 15° yaw and 15° roll angle) produced the least amount of flank and crater wear. Liu *et al.* [44] performed a series of turning experiments of the PVD (physical vapor deposition) coated inserts on Ti-6Al-4V alloy enhanced with MQL on the flank side. They reported that MQL significantly reduced tool wear on the AlTiN/Si₃N₄ nanocomposite tool by 35% compared to the uncoated carbide. Adhesive wear was the primary mode of tool wear.

1.6. Edge Trimming of Carbon Fiber Reinforced Plastics

Edge-trimming is a typical machining process to shape a carbon fiber reinforced plastic (CFRP) composite laminate to its near-net dimension made for various manufacturing applications [57]. CFRP materials are primarily used in high-strength and low-weight applications such as aerospace, defense, automotive, marine, and renewable energy industries [58], [59]. CFRP applications in such industries often require tighter dimensional tolerance. However, machining CFRP to near-net shape with high dimensional accuracies is often challenging due to tool wear [24-28]. The main tool wear mode commonly observed in machining CFRP is edge rounding [60][61][62]. It is caused by the abrasive action of carbon fibers, which imposes hard abrasion by fracturing carbide grains and soft abrasion by removing the soft cobalt binder and exposing and eroding carbide grains [62]. Worn-out tools increase cutting force and temperature during machining to exacerbate machining defects in CFRP workpieces, such as delamination, spalling, fiber pull-outs, and burning.

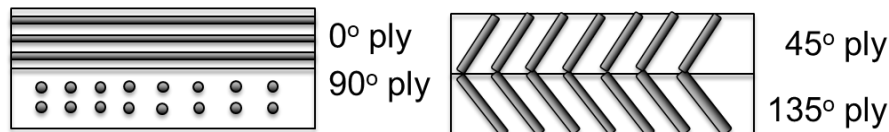


Figure 7. Typical cross-ply CFRP laminates (0/90 and 45/35)

Various tool wear mechanisms for CFRP machining processes have been reported, namely: drilling [62], turning [63], and milling [64]. In addition to the machining parameters, both workpiece material properties and fiber ply angle distinctly affect the tool wear and the cutting force required [65]. Nguyen *et al.* [66] reported the wear in edge-trimming of CFRP for a high modulus fiber was mainly influenced by the ply angle. The 45° plies yielded the worst flank wear, while the 90° plies yielded the worst edge radii. Merino-Pérez *et al.* [67] investigated the influence

of cutting speed and workpiece types on the thrust force and torque in the conventional dry drilling of woven CFRP. They studied high-strength (HS) fibers (CF0300) and high-modulus (HM) carbon fibers (CF2216). They reported mixed results as higher tool wear occurred when cutting the high modulus fibers at lower cutting speeds and the high-strength fibers at higher cutting speeds. They claimed the cutting temperature caused the discrepancy in tool wear in the corresponding experiment.

Merino-Pérez *et al.* [68], [69] also investigated the effects of the types of resin and carbon fibers on the thermal gradient [34], thermal damage, and mechanical damage in drilling CFRPs [35]. They reported less damage and defects on CFRP with high-modulus fibers than with high-strength fibers. However, they did not discuss the effects of carbon fiber properties on tool wear due to the insignificant amount of wear ($< 200\mu\text{m}$) in their investigations. Hodzic *et al.* [70] investigated the influence of cutting speed and feed on tool wear using high-strength (CF0300) and high-modulus (CF2216) carbon fibers with MTM28B and MTM44-1 matrix. They studied the applicability of Taylor's tool life model to the drilling process of CFRP using uncoated WC-Co tools. They measured tool wear in terms of flank wear, rate of edge radius change, and flank wear rate as a function of speeds between 1000 RPM and 18000 RPM. Based on the tool wear measurements, they concluded that the higher-strength fibers caused higher tool wear. However, these studies have not discussed the tool wear mechanisms based on carbon fiber properties.

A few studies compare machinability measures besides tool wear when machining CFRPs with various carbon fibers. In a performance evaluation study of three different drill types, Feito *et al.* [71] studied the delamination behavior of intermediate modulus (IM7) and standard modulus (AS-4) carbon fibers in various matrix systems. They studied the effects of feed on torque, force, and delamination corresponding to the drills making up to 60 holes. According to their results, force,

torque, and delamination depend on both drill and composite types. Although they did not evaluate the tool wear, composite and fiber properties influence force and torque. Xu et al. [72] compared the machinability of high-strength (T800S and T800) fibers with standard-modulus (T300) fibers in drilling. T800S has 66.5% and 27.8% higher tensile strength and tensile modulus than T300 fiber used in low-strength CFRP. The T800S fibers showed worse delamination behavior in the drilling process. However, they did not study tool wear in this experiment but optimized the process parameters to improve the surface finish.

As shown in the studies [33-38], tool wear in machining CFRP is related to the abrasive nature of carbon fibers on the material system. Polyacrylonitrile (PAN) and Pitch are two of the most used precursors to produce carbon fibers. PAN-based copolymers were first decomposed by pyrolysis and yielded 50- 55% carbon content [73]. This high carbon content makes the PAN-based carbon fibers to be widely used. In contrast, pitch precursors come as a byproduct of petroleum, asphalt, and coal tar industries, which have a lower carbon content. The production of pitch-based fibers begins with a mesophase pitch precursor formed by the isotropic heating pitch at 350-400°C [74]. The mesophase pitch is liquid crystalline and spun at high temperature to develop a graphitic crystalline structured fiber, enhancing modulus and thermal conductivity to the carbon fibers [75][76][77][78]. Due to their graphitic nature, pitch-based carbon fibers have lower compressive and transverse properties than PAN-based fibers [75]. Pitch-based carbon fibers are generally used in applications requiring ultra-high modulus and high-temperature conductivity. The effects of fiber orientation on tool wear in edge trimming of CFRP and the corresponding wear mechanism have been studied in our previous investigation [66], keeping the workpiece properties (fiber type) the same.

1.7. Organization of Dissertation

While many studies have been performed regarding the machining of Ti64 and CFRP, there are still key gap in the current knowledge. For Ti64, some aspect that needs to be addressed are the effect of various microstructure and strategies to improve machining. In this study, the different Ti64 microstructure selected for machining has not been widely reported elsewhere. The method of improving tool life by using coated carbide tools and MQL also different from other studies. For CFRP one aspect that was still unknown is the effect of mechanical properties to the tool wear. Therefore, this dissertation aims to understand the fundamental knowledge in the tool wear mechanism during the turning of different Ti64 grades and edge trimming of CFRP. The scientific questions are presented as:

1. What is the effect of the heat treatment history of the Ti64 to its machinability? If there is an influence, could it be characterized by the chip segments or the cutting force? How different is the crater wear between each grade?
2. What is the estimated temperature in machining Ti64 and as temperature increases, how can it affect the chip formation?
3. What is the best coating material that can apply to machine Ti64? How much improvement can be achieved and what are the limitations?
4. What are the best additives that can be mixed with oil to improve machinability of Ti64? Does coated tool performance increase when MQL is applied?
5. Would the different mechanical properties, such as tensile strength and elastic modulus in CFRP machining, influence the tool wear?

Therefore, the dissertation is organized as below. Following the literature review presented in Chapter 1, The tool wear and chip characteristics of different Ti64 microstructures are presented

in Chapter 2. Chapter 3 explains the finite element and crater wear mechanism of Ti64 STA microstructure. Chapter 4 shows the coating performance of turning Ti64 STA. Chapter 5 reports the minimum quantity lubrication (MQL) of the uncoated and coated tool when turning Ti64-STA. Chapter 6 presents the tool wear during the milling/ edge-trimming of CFRP with different fiber properties. Conclusions are presented separately in each chapter.

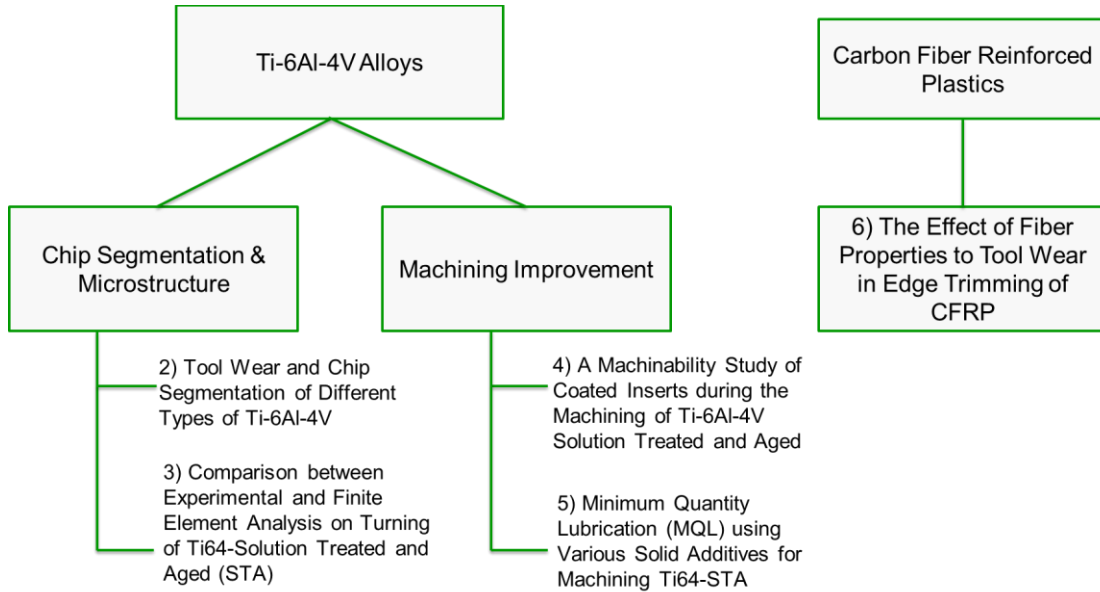


Figure 8. Dissertation Chapters

CHAPTER 2: TOOL WEAR AND CHIP SEGMENTATION OF DIFFERENT TYPES OF TI-6AL-4V

2.1 Motivation

Four different Ti64 microstructures reported in Chapter 1 may have different responses in the tool wear and the chip behavior. The four types are elongated (ELO), mill-annealed (MIL), solution-treated and aged (STA), and lamellar (LAM), which can be attained based on the heat treatment history applied during the processing of Ti64 [12]. ELO starts with 925 °C heat treatment for 4 hours, rapid cooling to 760 °C, and air cooled. The resulting microstructure is 96% equiaxed α phase and 4% β phase. The MIL type was processed by annealing at 730°C and then slowly cooled. MIL has equiaxed α grains (~89%) and a small fraction (~11%) of lamellar grains. Lamellar grains consist of a cluster of laths where the α phase is layered together with β phase. To obtain the STA microstructure, it is heated to 940°C for 1 hour (slightly below the β transus temperature). Then it is water quenched and aged at 510-550°C for 4 hours. This heat treatment yields an increased fraction of lamellar grains up to 57%. Additionally, the width of the α phase in the lamellar is much thinner than in the Ti64-MIL, as the cooling rate and the aging treatment controls the width. The STA microstructure has the highest strength and ductility, as seen in Table1. The LAM microstructure was produced by heating at 1035°C, above the β transus temperature of 955 °C. soaked for 30 minutes, and furnace cooled at the rate of 4-5°C/min. The resulting microstructure is fully lamellar grains (which are called colonies, as they have two phases) with an average colony size of ~700 μm . Despite the increased lamellar content, the tensile strength of Ti64 LAM is lower than STA, because the spacing between laths is much larger.

Machining studies of different microstructures for Ti64 are relatively limited. Attanasio *et al.* [79] reported on the machinability of different Ti64 using the micro-milling process at the

cutting speed of 15 m/min. The machining of LAM microstructure has better tool life and reduced built-up edge. The better machinability was due to its low hardness and weaker tensile properties. On another note, Nguyen *et. al* [11] performed turning experiments on different Ti64 grades at 61-122 m/min and observed the significant difference in the machinability. LAM microstructure yielded the highest flank wear. With larger lamellar cluster sizes, it enabled wider flank gouges on the surface. The flank wear rate also increased when the lamellar content is increased from the microstructure of ELO (0%) to LAM (100%). Additionally, finite element simulation was utilized to estimate the cutting temperature in the flank side.

The relationship between titanium microstructure and crater wear is better studied. Arrazola *et. al* [21] conducted turning experiments for Ti555.3 and Ti64 at 50-90 m/min. Ti 555.3 is a near β titanium alloy with higher tensile strength and lower β transus temperature. Ti555.3 showed poorer machinability compared to Ti64 due to higher cutting force and microstructure differences. The increased shear bands on the chips of Ti555.3 increase fluctuation in mechanical and thermal load on the rake face as well. Armendia *et.al* [20] compared the machinability of Ti64 and Timetal54M (Ti54M). Ti54M has similar mechanical properties with Ti64 but has more molybdenum content. At 90 m/min cutting speed, the Ti54M has better machinability than Ti64 with lower flank wear and crater wear depth. The good performance when machining Ti54M was related to its slightly lower specific force and the difference in the microstructure. Hatt *et. al*[80] performed diffusion couple experiments between tungsten carbide tool and different titanium microstructures. Timetal 407 which contained less β has higher TiC adhesion layer than Ti64 and was expected to have better tool performance. In contrast, Ti6426 which showed no TiC formation during the diffusion couple experiments, would have poor machinability. TiC layer was found to be effective in reducing crater wear at low cutting speed of titanium (61 m/min) as reported by

Hartung and Kramer [14], however, at high cutting speeds the TiC layer is removed and crater happens rapidly.

To the best of author's knowledge, the microstructural impact of Ti64 on crater wear is not well known. Additionally, the chip segments from generated from the machining of different Ti64 grades could indicate the characteristics in the crater wear. This section conducts turning experiments for different Ti64 grades while measuring crater wear and analyzing the chip segments.

2.2 Experimental Setup

2.2.1 Turning experiments

Turning experiments were conducted with the four Ti64 cylindrical bars, ELO, MIL, STA, and LAM, with 5" diameters and lengths between 14"-25" [11]. The straight turning process was carried out in dry condition using a Daewoo PUMA 300L CNC lathe. Each sample was turned at three different surface cutting speeds of 61, 91, and 122 m/min until tool fracture. The depth of cut and feed rate was kept constant at 1.2 mm and 0.127 mm/rev. Uncoated tungsten carbide inserts by Sandvik Coromant with H13A grade are 1 μm carbide grain size and 6 wt% of cobalt binder. The rake and relief angles were 0° and 7° , respectively. The inserts have a 15° leading angle. Figure 9 and Table 3 show the geometry of the inserts used for turning experiments. After turning the titanium alloy for 30 seconds, the chips are collected.

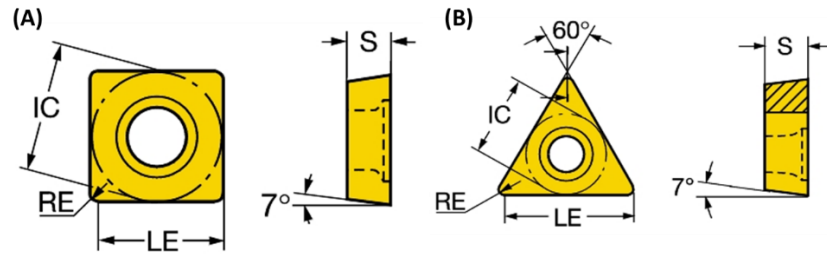


Figure 9. Tool Geometry for Turning and Orthogonal Cutting Experiments

Table 3. Details of The Cutting Tools Geometry

	Lathe Turning	Orthogonal Cutting
Inscribed Circle Diameter (IC)	12.7 mm	6.35 mm
Corner Radius (RE)	0.794 mm	0.397 mm
Cutting Edge Effective Length (LE)	11.9 mm	10.34 mm
Insert Thickness (S)	4.762 mm	3.175 mm

2.2.2 Turning Force Measurements

Another set of turning experiments was conducted by utilizing a Haas TL01 Lathe. The additional experiments measured the cutting forces with the Kistler Piezo Multicomponent Dynamometer type 9257B with a sampling rate of 100 Hz. Details of the experimental setup are shown in Figure 10. The forces were measured for the first 30 seconds at three different cutting speeds. The three force components recorded are the feed force (F_x), radial force (F_y), and cutting force (F_z). Because the workpiece was consumed for ELO grades, force data was not measured.

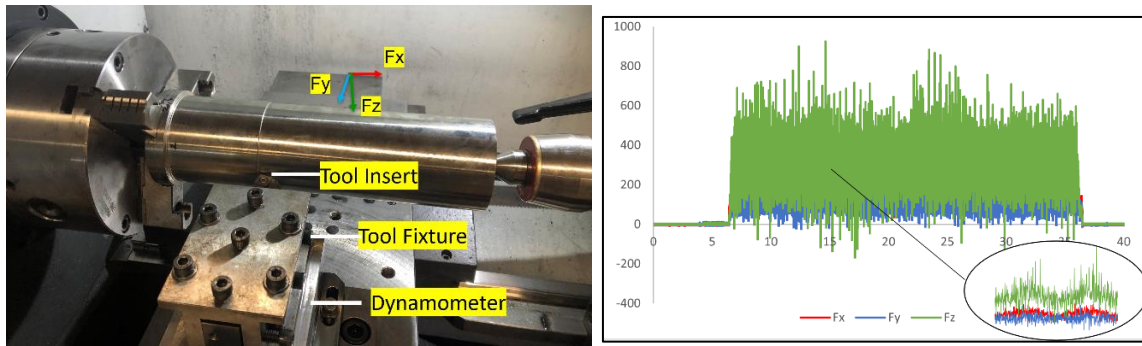


Figure 10. Experimental Setup to Measure Cutting Force and Typical Force Signal in Turning Experiments. Inset shows the three force components F_x , F_y , and F_z .

2.2.3 Orthogonal cutting experiments

Orthogonal cutting experiments were conducted using thin disk of Ti64 as the workpiece obtained by wire electrical discharge machining (EDM). The disk thickness was 2.2 mm, with a diameter of 52.2 mm. All Ti64 grades were cut at different speeds (61, 91, and 122 m/min) with a feed rate of 0.127 mm/rev. The Kistler dynamometer was set up to record the cutting process for 5 seconds with a sampling rate of 5kHz. Details on the orthogonal machining setup are presented in Figure 11.

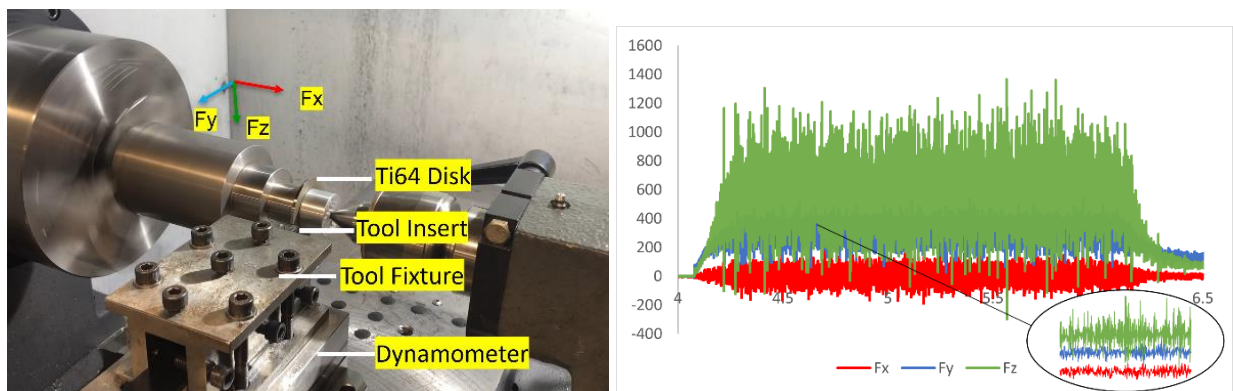


Figure 11. Orthogonal Machining Setup and Typical Cutting Force Signal. Inset shows the three force components F_x , F_y , and F_z .

2.2.4 Chip Mounting

The chip produced within the first 30s of the cutting time of the turning experiment was collected at each cutting speed. Each chip was mounted using a conductive mounting powder, then ground and polished with different silicon carbide papers (600, 800, and cloth pad) to reveal the cross-section. The segmented chip surface was etched using Kroll's reagent for 1 minute using a swab. The cross-section of the etched chip was then imaged using both a Nikon light microscope at 50x and a JSM-6610 JEOL scanning electron microscope (SEM) at 50x using a backscattered electron (BSE) imaging setting. Figure 12 shows the typical chip morphology for a Ti64 chip BSE image, from which the chip characteristics, such as chip segmentation distance (d), valley height (h_1), peak height (h_2), and shear angle (ϕ), were measured

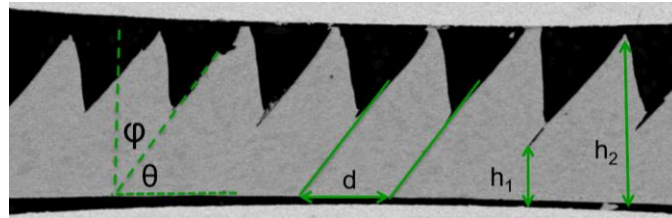


Figure 12. Ti64 chip mounted and imaged using SEM backscatter.

2.2.5 Crater Wear Measurements

Crater wear was measured on the worn tools by first etching the adhesion layer and built-up edges using a hydrofluoric (HF) acid mixture. The composition of the etchant is 1 part of HF 48%, 1 part of peroxide (H_2O_2) and 20 part of water. The etching process is 15-20 minutes. Then the surface of worn tools were characterized using an Olympus Fluoview FV1000 Confocal Laser Scanning Microscopy (CLSM) system using the reflection laser at the magnification of 10x and the step size of 1 μm . The CLSM images at different z-height were overlapped to generate the height-encoded images (HEI). The wavelet-based algorithm constructed in MATLAB [81] was

used to eliminate the noise in the HEI images. Figure 13 shows the crater wear processing steps from the height encoded image to the 2-D crater profile.

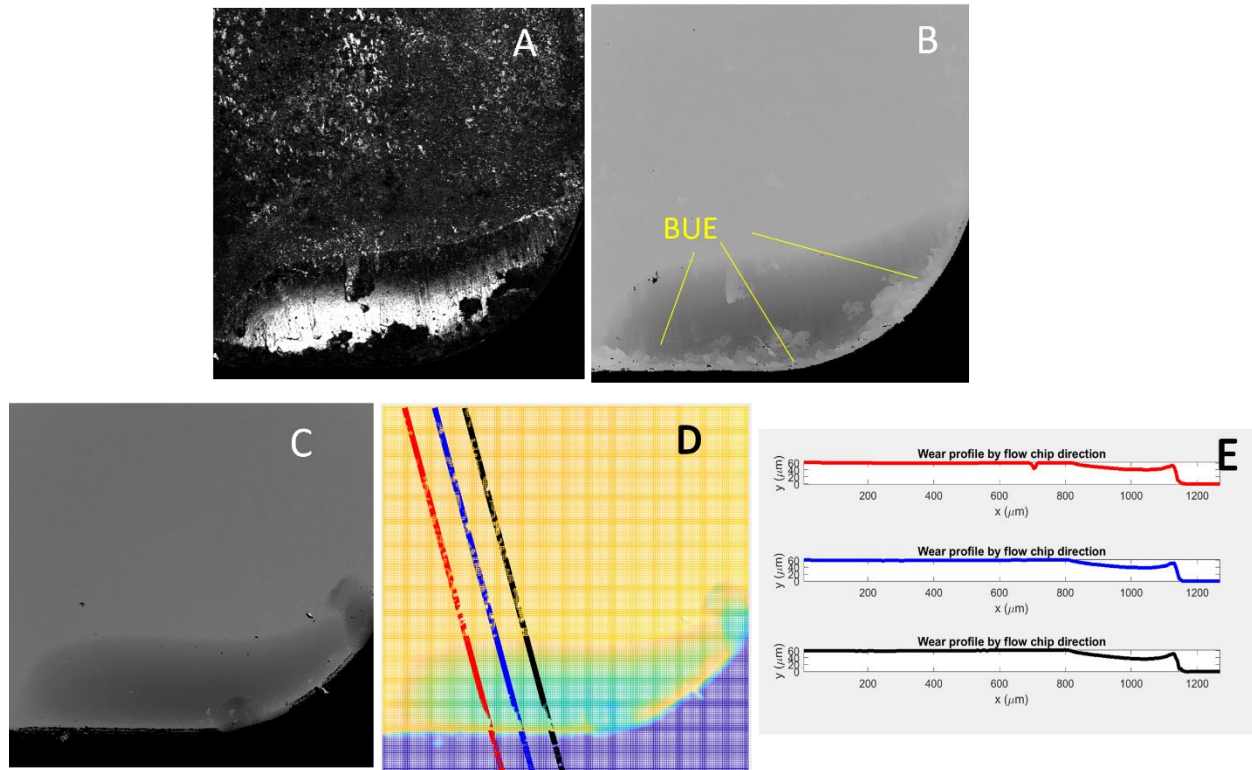
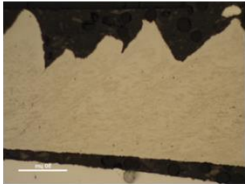
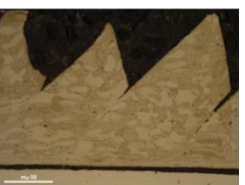
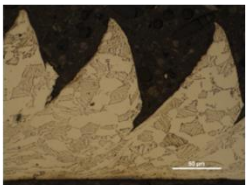


Figure 13. A) Worn tool of Ti64-STA at 122 m/min B) Height encoded image of worn tools prior to etching showing built-up edges (BUE) C) Height encoded image of the worn tool after etching D) processed tool profile using MATLAB E) 2-D crater wear profiles selected from D)

2.3 Results

2.3.1 Chip Morphology

Table 4. ELO, MIL, STA, and LAM etched chip captured at 50x

Cutting Speed	ELO	MIL	STA	LAM
61 m/min				
91 m/min				
122 m/min				

The chip images from optical microscopy of different microstructures and speeds were assembled in Table 4. All the chips are segmented or saw-tooth shaped. The region between each of the 'teeth' of the chip is called the primary shear zone or the shear band. First, the different Ti64 grades show distinct microstructural differences. In the image, light grains show the α phase, while the dark grains show the β phase that were etched by the reagent. The ELO chips generated at low and medium speeds consist of stretched α grains and surrounding β . The stretched α grains indicate that extensive deformation occurred during the turning process. At high speed, the chip shows that α phase become more equiaxed. Upon inspection, adjacent to the dark β grains are the thin-shaped secondary α grains (see figure 14)

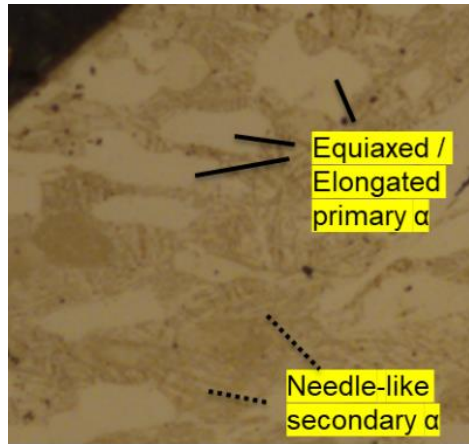


Figure 14. ELO chip at 122 m/min showing the composition of the microstructure

The MIL chips generated at different speeds have similar appearances, a combination of equiaxed α phase and lamellar clusters. The MIL grade lamellar cluster comprises layered α and β , with the α phase width around 2 μm . For STA chips, it showed a weaker response to etching. Therefore, the chip microstructure was not visible, as the lamellae α phase width for the STA chip is thinner. During measurements shown in Figure 15, MIL primary α grains were measured to have an average size of 27.9 μm , and STA was 14.3 μm . For the STA, the primary α grains appear to be more elongated and sheared between two 'teeth' of the chip.

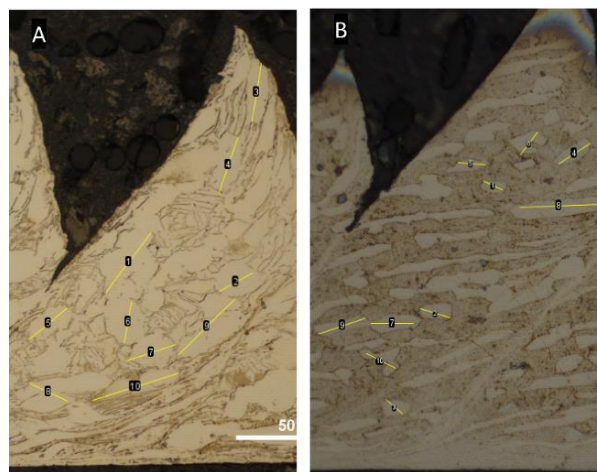


Figure 15. A) MIL chip at 91 m/min and B) STA chip at 91 m/min

LAM chips showed a large lamellar cluster of layered $\alpha+\beta$ phase. At 61 m/min, the LAM chip shows uniform lamellar cluster with a highly deformed region in the primary shear zone. Figure 16 shows LAM 61 chip and the primary shear zone. At 91 m/min, the chip shows larger α phase that is different from layered $\alpha+\beta$. The microstructure is not due to heat treatment but is another orientation of lamellar cluster. Figure 17 shows different lamellar orientation inside the LAM 122 chips. As the chip is highly irregular, the peak height can reach up to 400 μm .

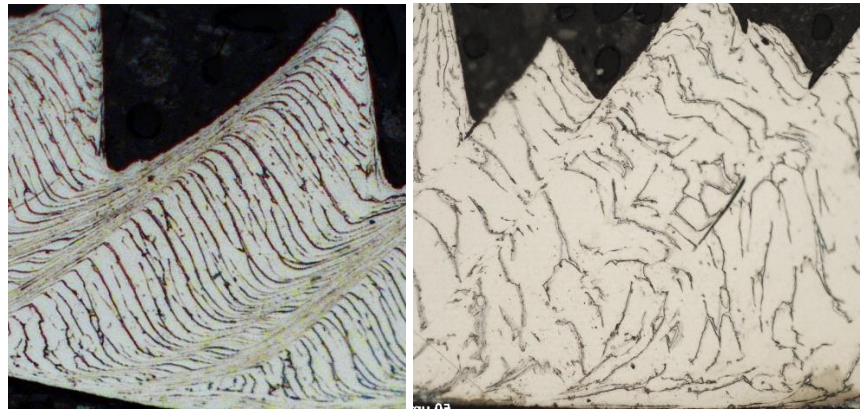


Figure 16. Enlarged LAM 61 chips with highly sheared region (left) and LAM 91 chip with larger α region in the laths.

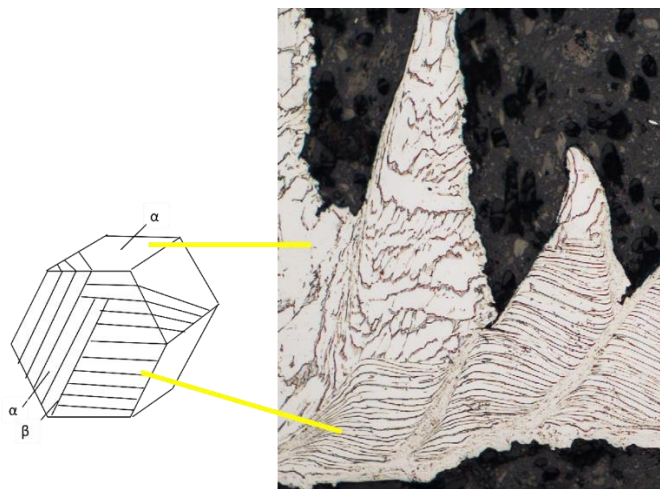


Figure 17. Illustration of different lamellar cluster orientation in the irregular LAM 122 chips

Figure 19 shows the quantitative analysis of the chip formation from the different morphologies. A total of 100 "tooth" /segments of the chip were measured for each turning experiment. The calculated results are presented in a box plot chart. Figure 18 shows the typical box plot chart which reports the statistical variation. The chart consists of the median , interquartile range, and whiskers, which is $1.5 \times \text{IQR}$ from each quartile (Q1 or Q3). Outliers are the data points outside of the whiskers. The mean for the data is also marked with an x symbol. Additionally, the histogram for the measured chip segmentation distance is presented in Appendix A

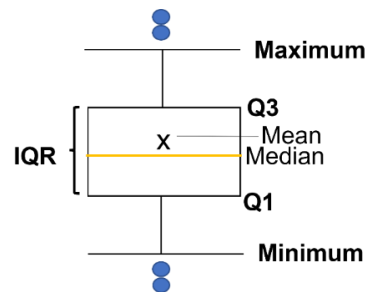


Figure 18. Typical box plot chart of measured data points

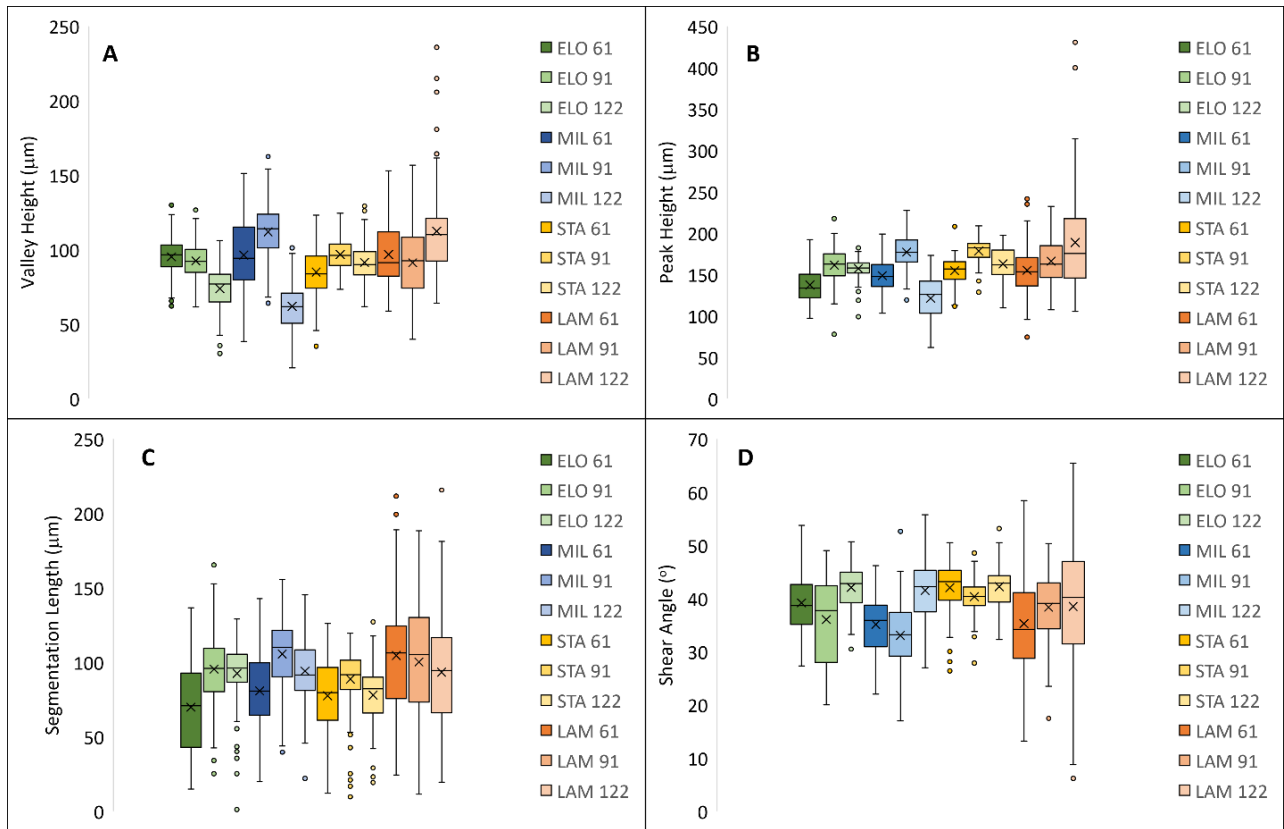


Figure 19. Different measured chip morphology of different Ti64 from machining at different speeds A) Valley Height B) Peak Height C) Segmentation Length D) Shear Angle

The labeling in Figure 19 differs based on the microstructure type and cutting speed. For example, ELO data were colored green and labeled ELO61, ELO91, and ELO 122. The results were also organized numerically in Table 5 for each parameter's average and standard deviation. Figure 17A shows the measured valley height from the chip crack to the smooth surface of the chip, as shown in Figure 10. The general trend shows the valley height with values between 61-112 μm (shown in Table 5) for Ti64 grades cut in the experiment. The lowest valley height was recorded for MIL122, while the highest valley height was recorded on LAM122. The low value of valley height infers either crack or shear occurs more intensely. The topic of titanium chip producing cracks or shear bands is discussed in [17].

Peak height measurements (h_2) show the maximum chip height for each ‘tooth’. Typically, in metal machining, the chip height is close to the value of feed of the machining parameter. Then, the chip height can be used to approximate the shear angle of the cutting process [82]. The peak height for Ti64 was measured between 121-189 μm . The lowest peak height is recorded for MIL122 while the highest is LAM 122.

Table 5. Measured chip morphologies for Ti64: Average segmentation length (d) and its standard deviation (s_d); Average valley height (h_1) and its standard deviation (s_{h_1}), Average peak height (h_2) and its standard deviation (s_{h_2}); Average shear angle (φ) and its standard deviation (s_φ)

Ti64 Grades	ELO			MIL			STA			LAM		
Cutting speed (m/min)	61	91	122	61	91	122	61	91	122	61	91	122
d (μm)	69.8	95.4	92.5	80.8	105.6	94.1	77.5	88.7	77.9	104.6	100.2	93.3
s_d (μm)	30.3	25.5	20.7	25.3	23.9	21.1	23.9	20.5	21.1	38.2	38.7	42.1
h_1 (μm)	95.1	92.4	73.7	96.3	111.9	61.9	84.9	96.7	91.4	96.8	91.2	112.3
s_{h_1} (μm)	12.6	11.6	14.4	23.0	18.9	15.6	16.1	10.4	13.4	19.8	26.2	30.3
h_2 (μm)	137.3	161.2	156.9	148.4	177.0	121.1	154.5	178.3	162.7	155.0	165.9	188.6
s_{h_2} (μm)	19.6	21.5	12.6	18.3	20.1	26.5	15.8	15.3	19.3	28.5	27.5	63.4
φ ($^\circ$)	39.2	36.0	42.1	35.1	33.1	41.5	42.0	40.3	42.2	35.3	38.3	38.5
s_φ ($^\circ$)	5.3	8.1	4.0	5.4	6.7	5.7	4.7	3.3	3.6	8.9	6.3	12.3

The results in Figure 19 and Table 5 shows the segmented length increased for MIL from low speed (61 m/min) to medium speed (91 m/min). The segmented distance of MIL61 is 80.8 μm and it increased to 105.6 μm at MIL91. From medium to high speed (122 m/min), the segmented distance is slightly decreases to 94.1 μm . This trend is similar for ELO and STA. On the other hand, the segmented length for LAM is decreasing as the cutting speed increased. LAM61 has the segmented distance of 104 μm and is reduced to 100 μm at LAM 91 and 93 μm at LAM122.

The final chip morphology that measured is the chip shear angle. Merchant’s theory for metal cutting [82] suggests that the shear angle increases with a lower cutting force, and vice versa.

Table 5 shows that the measured shear angle was between 35 and 43°, close to the ideal shear angle of 45°. As the cutting speed increases, the average shear angle increases for all cases, indicating the reduced cutting force at a higher speed. However, it is noted that the LAM chip has a wide range of shear angles in the range of 10°-60°.

2.3.2 Crater Wear

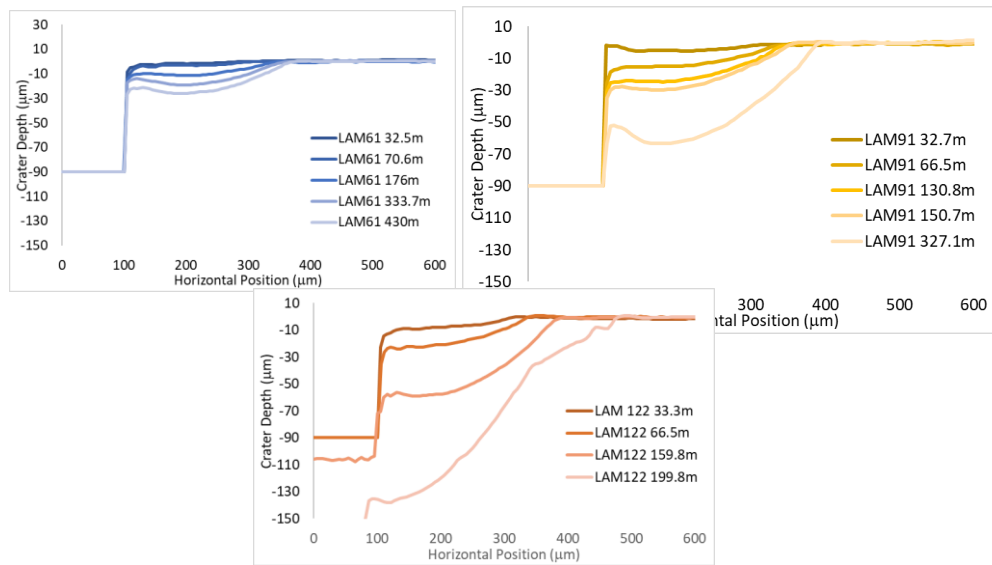


Figure 20. Crater wear progression for LAM 61, LAM 91, and LAM 122

The worn tool was measured after etching using the confocal laser microscope. Figure 20 shows the progression of the crater wear profile for turning Ti64-LAM. The crater depth at 430m of cutting length is relatively small at low cutting speed, around 30 μm . While at 122 m/min the crater depth reached $\sim 150 \mu\text{m}$ at 200 m cutting length. Figure 21 (A) shows the crater wear depth with cutting length at the low speed (61 m/min). There is a similar crater wear progression between all grades, except STA, which has the lowest crater depth, but an early fracture. At 91 m/min, the machining of Ti64-STA also caused premature failure. At 122 m/min Ti64-LAM has the deepest crater depth at 150 μm . Crater wear rate is calculated by dividing the crater wear depth to the time

the tool fractured. The crater wear rate is then summarized in Figure 22 for each cutting speeds, indicating that the LAM grade has the greatest wear rate at 122 m/min.

$$\text{crater wear rate } (\mu\text{m}/\text{min}) = \frac{\text{crater depth at fracture}}{\text{time at fracture}} \text{ Eq. 1}$$

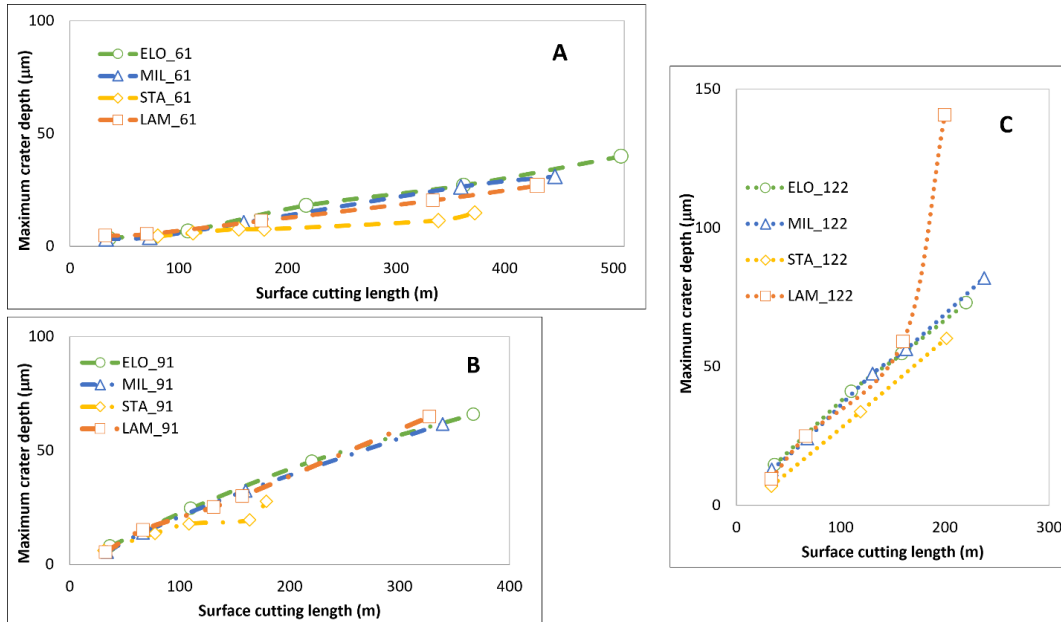


Figure 21. Crater wear chart for different Ti64 at A) 61 m/min B) 91 m/min and C) 122 m/min

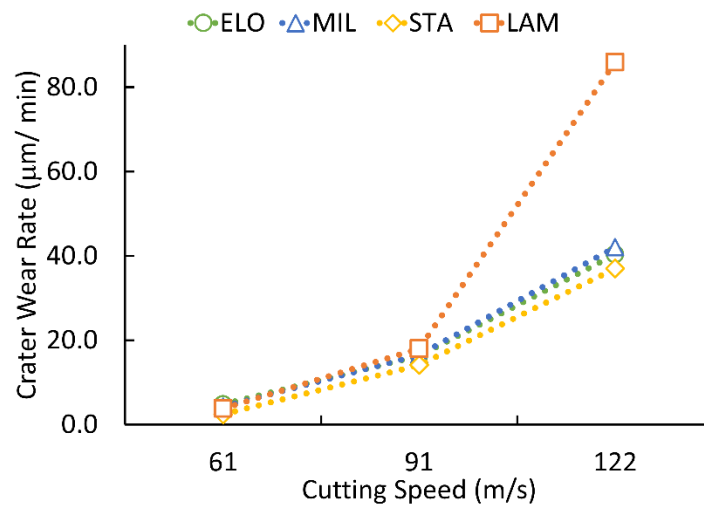


Figure 22. Crater wear rate at different cutting speeds for Ti64 ELO, MIL, STA, and LAM

2.3.3 Measured Cutting Force

The measured cutting force from turning force is expressed in three directions (F_x , F_y , and F_z). While in orthogonal cutting the F_x is zero due to the minimum side flow, therefore F_y and F_z were measured. Next, the average and standard deviation of the cutting force were normalized to the chip width for the different cutting types (Turning: 1.2 cm and Orthogonal: 2.2 cm). Average and variation of the force for turning and orthogonal cutting are presented in Figures 23 and 24. In addition, the values for the measured turning and orthogonal cutting force are presented in Table 6 and Table 7.

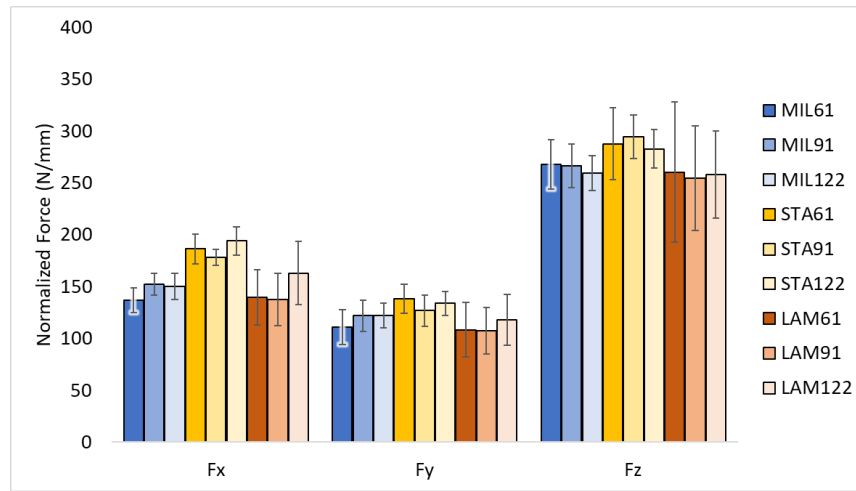


Figure 23. Bar chart of average force during turning of Ti64, whiskers indicates ± 1 standard deviation of the measurements.

Table 6. Average force and standard deviation during turning of Ti64 MIL, STA, and LAM

Ti64 Grades	MIL			STA			LAM			
	Cutting speed (m/min)	61	91	122	61	91	122	61	91	122
F_x (N/mm)		137.2	152.3	150.3	186.4	178.3	194.0	139.5	137.6	162.9
s_{F_x} (N/mm)		11.9	10.7	12.5	14.3	7.8	13.5	26.8	24.9	30.4
F_y (N/mm)		110.9	122.0	122.3	138.4	126.9	134.0	108.3	107.2	117.8
s_{F_y} (N/mm)		16.8	15.1	12.1	14.0	15.1	11.6	26.3	22.5	24.6
F_z (N/mm)		267.7	266.6	259.3	287.8	294.3	282.7	260.4	254.7	258.3
s_{F_z} (N/mm)		23.9	21.1	16.7	34.7	21.0	18.5	67.6	50.4	42.1

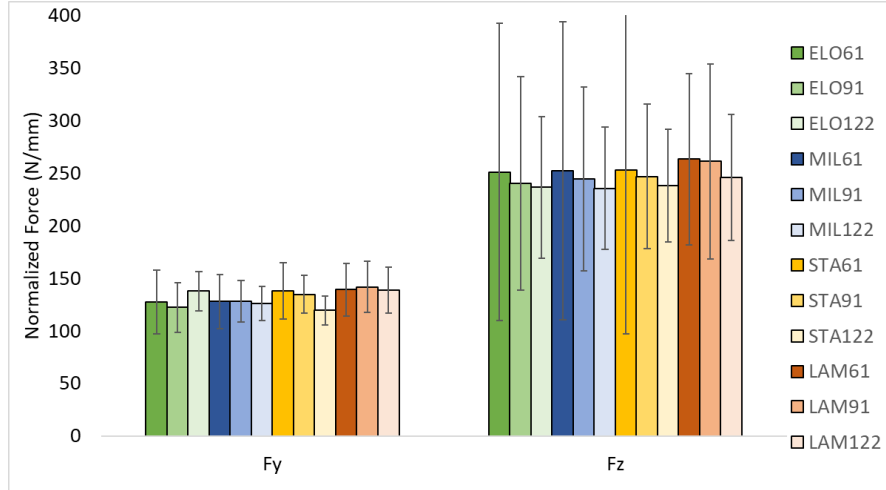


Figure 24. Bar chart of average force during orthogonal cutting, whiskers indicates ± 1 standard deviation of the measurements.

Table 7. Average force and standard deviation during orthogonal cutting of Ti64 ELO, MIL, STA, and LAM

Ti64 Grades	ELO			MIL			STA			LAM		
Cutting speed (m/min)	61	91	122	61	91	122	61	91	122	61	91	122
F_y (N/mm)	127.4	122.3	137.8	127.8	128.2	126.0	138.2	134.8	119.4	139.2	141.8	138.8
s_{F_y} (N/mm)	30.3	23.8	18.9	25.5	19.9	16.3	27.0	18.1	14.0	24.9	24.6	21.9
F_z (N/mm)	251.1	240.4	236.7	252.4	244.5	235.7	253.0	247.0	238.3	263.5	261.2	246.2
s_{F_z} (N/mm)	141.5	101.3	67.3	142.0	87.6	58.4	155.9	68.7	53.8	81.6	92.7	60.1

In general, cutting forces from turning (F_x , F_y , F_z) from the turning experiments are higher on average than orthogonal cutting forces (F_y , F_z). One reason for the lower orthogonal cutting force is the workpiece setup is less rigid for the thin disk when compared to turning a solid bar. Therefore, the cutting force from the orthogonal cutting has more variation / swings. Another reason is turning experiments are conducted for a longer cutting time (30s) than orthogonal cutting (5s). Longer cutting time allows for increased temperature on the cutting interface and built-up edge (BUE) on the tool, increasing the cutting force.

For turning Ti64, STA was measured to have the highest feed (F_x), radial (F_y), and cutting (F_z) force in comparison to MIL and LAM. Chapter 1 shows the tensile strength of the Ti64-STA is the highest. On the other hand, during the orthogonal cutting, there is no significant difference between feed force (F_y) and cutting force (F_z) for the different grades. Therefore, the cutting force recorded from the turning process is better for analyzing the chip formation of the different Ti grades. The cutting force from the turning process was used to estimate the friction coefficient between the tool and the chip. According to [82], the friction coefficient of metal cutting is the ratio between the measured feed force and the cutting force perpendicular to the tool. Due to the turning process with a leading angle of 15° , then friction coefficient can be calculated as:

$$\mu = \frac{F_x \sin 15^\circ + F_y \cos 15^\circ}{F_z} \quad \text{Eq. 2}$$

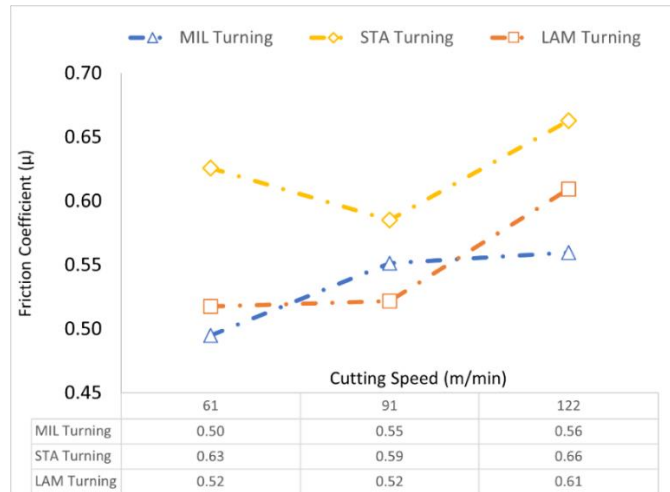


Figure 25. Friction coefficient estimated for turning Ti64 MIL, STA, and LAM

2.4 Discussions

The segmented chip was always formed when turning Ti64-ELO, MIL, STA, and LAM. As cutting speed from 61 m/min increased to 91 m/min, the segmentation distance (d) generally increased. Recht [25] reported in titanium cutting for 1 m/min and 42 m/min, the chip segments is

larger for the higher speed. The widening of the chip segments is related to the increased temperature in the adiabatic shear band. Figure 26 illustrates the chip formation at different speeds. The chip segments are shorter for the slower speed due to the low temperature in the shear zone (blue line). In contrast, the high temperature in the higher cutting speed allows for thermal softening and more shear & cracks.

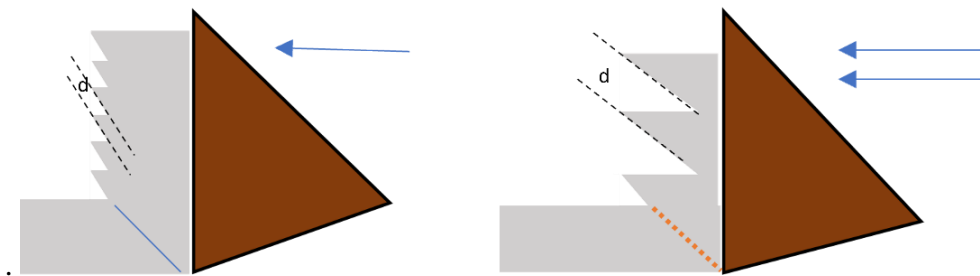


Figure 26. The difference in chip segmentation at low and high cutting speed according to Recht [25]

At 122 m/min, the segmented chip distance is expected to increase as the cutting speed is faster and the temperature is higher. However, the segmentation distance (d) was slightly lower for all Ti64 grades. The LAM chip morphology was also not following the trend, where d decreases as the cutting speed increases from 61 to 122 m/min. The cause of this reduction is unclear. Molinari [83] reported for the extremely high-speed cutting of Ti64 (600 to 1800 m/min), the chip segmentation distance is inversely related to the cutting speed by the formula of

At 122 m/min, it is expected that the chip segmented distance would increase as the cutting speed is faster and temperature is higher. However, the segmentation distance (d) was found to be slightly lower for all Ti64 grades. The LAM was not following the trend as well, where d decreases as the cutting speed increases from 61 to 122 m/min. The cause of this is currently unclear.

Molinari [83] reported for the extremely high speed cutting of Ti64 (600 to 1800 m/min), the chip segmentation distance is inversely related to the cutting speed by the formula of

$$Lc \approx AV^{-\frac{3}{4}} \text{ (Eq. 3)}$$

Lc is the segmented distance, A is the material coefficients, and V is the cutting speed. The decrease of segmented distance was theorized as the increased strain rate sensitivity and stress perturbation in the shear band formation[84].

ELO 122 chips shows thin α platelets (secondary α) forming near the equiaxed α phase. Pederson reported heating followed by quenching at a certain condition could produce a secondary α phase in Ti64[85]. Specifically, the phase is also known as *widmanstatten* (Figure 27). Therefore, the heat generated at 122 m/min is much higher, it could yield the secondary α phase after air cooling. A lumped system approximation [86] was made to calculate the machining cooling rate at 16.3°C/s, with details in Appendix B. Sridhar *et al.* [87] reported the cooling rate is equivalent to an oil quench for a 40 mm diameter bar near alpha titanium alloy Ti-6Al-3Zr-3Sn, which yields 0.07 μm of *Widmanstatten* α . No extreme microstructure changes was found during Ti64 MIL, STA, and LAM chips machining.

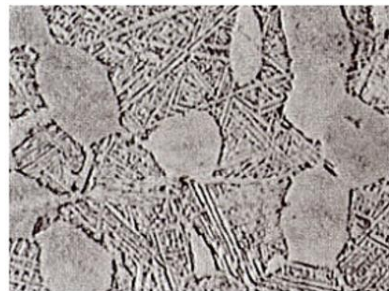


Figure 27. Widmanstatten microstructure of secondary α grains [85]

Figure 22 shows that the Ti64-LAM has the highest crater wear rate at a cutting speed of 122 m/min. However, LAM has a lower tensile strength than STA. Additionally, Attanasio [79] reported the hardness for STA (bimodal) microstructure is the highest at 411 HV, while LAM is

the lowest at 356 HV. Therefore, at 122 m/min cutting speed, this distinct microstructure highly influenced the crater wear. LAM grains are significantly larger at 743.1 μm , as shown in Table 8. Deforming the larger clusters at the interface (secondary shear zone) and the shear band (primary shear zone), will require increased energy and work for. Especially for orientation that are resistant to deformation, vice versa for the ‘softer’ orientations, leading to more variable loading on the tool.

Table 8. The average constituent grain size in different microstructure of Ti64 [11]

	ELO	MIL	STA	LAM
Average size of α -grains (μm)	8.1	15.2	10.2	—
Average size of lamellar grains (μm)	—	22	19.7	743.1

LAM was measured with a lower shear angle compared to other grades at 122 m/min. A lower shear angle indicates a ‘difficult’ to deform material during machining, as more shear force is required to cut [82]. In terms of microstructure, the LAM chips have the largest spread in the measured chip morphology (d , h_1 , h_2 , and ϕ), indicating a less regular chip structure. The large variation in chip morphology is related to the high deviations of cutting forces in turning the LAM workpiece (Figure 23) . The extreme swings in cutting force could cause a stronger “hammering” impact from the workpiece to the tool and cause a deeper crater.

Li *et.al* studied the heat treatment of Ti64-0.55Fe alloy with various initial microstructures (MIL, STA, LAM) [88]. The lamellar grains transformed faster to β phase at elevated temperature. Figure 28 shows the transformation of lamellar grain to β phase in the MIL microstructure from 880 to 940°C, while the remaining α remained untransformed. More transformed β phase in the LAM chip, it can accelerate wear due to increased diffusion of the tool material elements; tungsten, carbon, and cobalt. The crater wear mechanism will be discussed further in the next chapter. In our chips, there is no traces of the β phase following the rapid cooling from the air convection,

suggesting that the transformed β phase reverted to α phase. Further work is needed to pinpoint the potential presence of transformation to β in the machining chips.

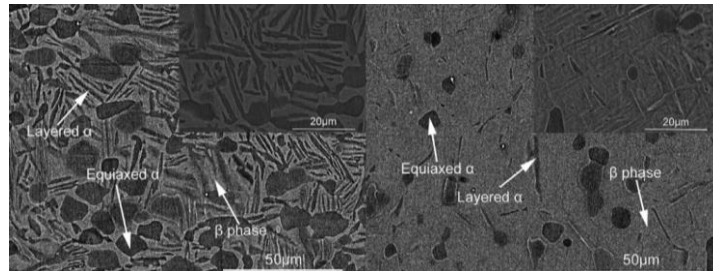


Figure 28. Lamellar grains (layered α) transformed into β grains at 940°C, from [88].

Ti64-STA fractured earlier than the other grades at all cutting speeds. A severe tool fracture is shown in Figure 29. It was observed in this experiment, fracture mainly occurred on the tool nose. The nose showed increased attrition of the titanium forming a built-up edge (BUE). The high cutting force of STA shown in Figure 23 could indicate the BUE is thicker compared to other grades and this may have caused the earlier failure.

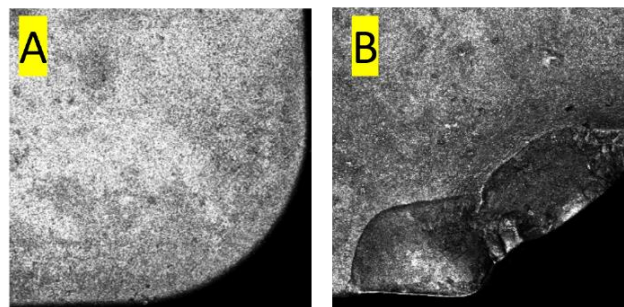


Figure 29. A) Uncoated tungsten carbide tool B) Severe fracture on the tool after machining Ti64-STA at 122 m/min

2.5 Conclusions

In this chapter, four different heat treatment microstructures of Ti64 (ELO, MIL, STA, and LAM) were machined at the cutting speeds of 61, 91, and 122 m/mins. Chip morphologies from

the turning process were characterized by the microscopy images. In addition, crater wear and cutting force were measured. Findings include:

1. All turning experiments showed a segmented chip formation when cutting at different speeds. The trend shows as the cutting speed increases from 61 m/min to 91 m/min, the segmentation distance increases due to the elevated thermal gradient inside the chip. The segmented chip distance decreases slightly from 91 m/min to 122 m/min.
2. The behavior of the ELO at 122 m/min provides some clue of a changed microstructure due to increased temperature and subsequent fast cooling. ELO shows the formation of secondary α grains in a thin needle shape which did not occur at other cutting speeds.
3. At 122 m/min, LAM shows the highest crater wear rate. While having a lower strength than other grades, the distinct microstructure yields a higher force variation, higher friction coefficient, and probably a faster phase transformation to the β phase.
4. In terms of tool life, the STA microstructure caused early fracture due to the built-up edge and increased cutting force.

CHAPTER 3: COMPARISON BETWEEN EXPERIMENTAL AND FINITE ELEMENT ANALYSIS ON TURNING OF Ti64-SOLUTION TREATED AND AGED (STA)

3.1 Motivation

In the previous chapter, the titanium turning process was characterized based on its chip morphology and the tool life. The chip formation in machining Ti64 was highly influenced by the initial microstructure (ELO, MIL, STA, LAM) and the cutting speed. However, to understand tool wear, the cutting temperature during the cutting process must be known.

While many works have studied the behavior of shear band formation on chip segmentation and temperature. Most are focused on a large spectrum of strain rate with the Ti64 MIL microstructure, described in [27], [36], [37]. The machinability study in different microstructures of Ti64, such as solution treated and aged (STA) is relatively limited. Therefore, turning experiments were carried out for Ti64 with STA and MIL microstructures under the same machining conditions for the comparative study on crater wear, tool life, and chip morphology. A finite element analysis model was developed using the chip morphology information to estimate the cutting temperature and electron backscatter image of chips were done to identify details about the chip microstructure and its impact on wear.

3.2 Experimental

3.2.1 Work Material

The differences in the MIL and STA microstructures of Ti64 are mainly characterized by the spatial arrangement of the two phases with hexagonal α and body centered cubic (BCC) β crystal structures [12]. MIL and STA from Rolled Alloys©(MI, USA) were used in this experiment. STA has higher strength and ductility than MIL [12]. The production of MIL and STA microstructures

This chapter is published as : Khawarizmi, R.M., Lu, J., Nguyen, D.S. *et al.* The Effect of Ti-6Al-4V Microstructure, Cutting Speed, and Adiabatic Heating on Segmented Chip Formation and Tool Life. *JOM* **74**, 526–534 (2022). <https://doi.org/10.1007/s11837-021-05091-1>

is shown in Chapter 2. The composition and material properties of both microstructures and the chemistry are shown in Table 9.

Table 9. Material and Chemical Properties of Ti64-MIL and Ti64-STA [12]

Ti	Al	V	Fe	O	C	N	Y
89.06%	6.63%	3.94%	0.14%	0.18%	0.03%	0.02%	0.001%
Grade	Ultimate Tensile Strength (MPa)	Tensile Yield Strength (MPa)	Elongation, %	Reduction of area, %			
Ti64 MIL	930	860	10	20			
Ti64 STA	1270	1181	16	41.5			

3.2.2 Turning Experiments

MIL and STA were machined in straight dry turning until tool fracture at cutting speeds of 61, 91, and 122 m/min (1, 1.5, and 2 m/s). The cutting speed of 122 m/min is higher than the cutting speed typically used in industry practice[13]. Uncoated tungsten carbide Sandvik H13A tools, 1 μm carbide grain size and 6% cobalt binder was used, shown in Figure 30. A constant feed rate of 0.127 mm/rev and depth of cut of 1.2 mm are used for turning. After the machining experiment and chip collection, another set of experiments were conducted to measure the cutting forces with a Kistler force dynamometer as shown in Chapter 2

The chip produced within 30 s of cutting time was collected for each cutting speed. Each chip was mounted using a conductive mounting powder, then ground using silicon carbide paper and polished with colloidal silica to reveal the cross-section. Each segmented chip surface was etched using Kroll's reagent for 1 minute using a swab. The cross section of the etched chip was then imaged using a Nikon light microscope at 50x magnification. Since the normal bright field image does not always clearly reveal the contrast between primary α and transformed (prior) β phases in the microstructure, dark field imaging was employed to better delineate the boundaries between the primary α and transformed β . Figure 31A shows the chip morphology for STA after etching where the darker grains are the primary α phase and the lamellar transformed β is gray. It is apparent that the shape of each segment is distinct from each other, and cracks are sometimes observed. MIL chips have similar chip morphology and are not shown in this chapter. The characteristics of chip morphology was shown Figure 31B and 31C, which will be used to fine-tune the constitutive models in the next section

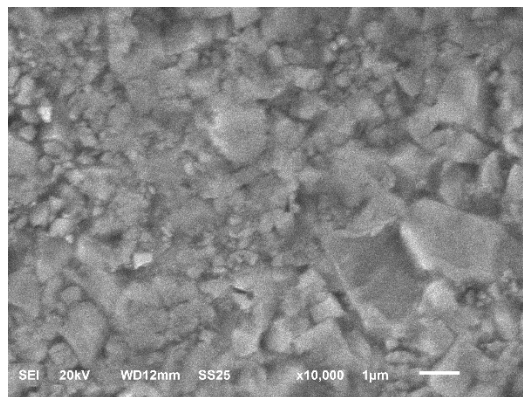


Figure 30. WC grains in the cutting tools.

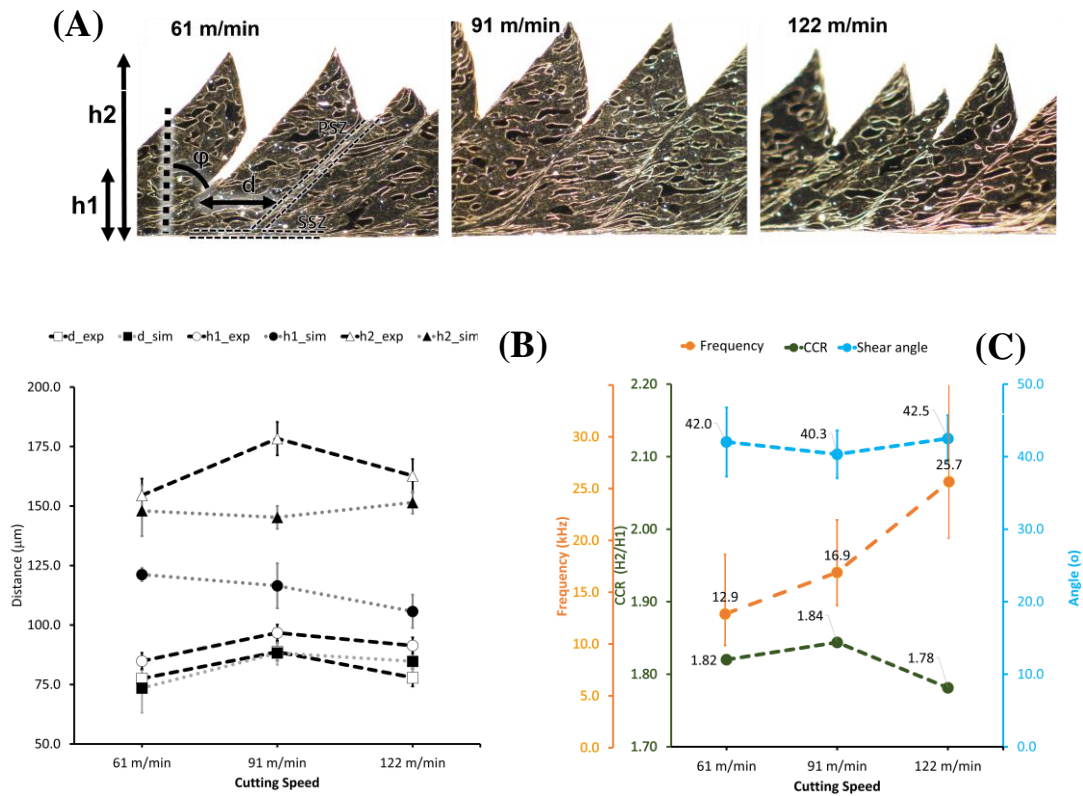


Figure 31. A) Dark field optical micrographs of etched Ti64-STA chips from 61, 91, and 122 m/min and metrics that characterize morphology. (B) Measured experimental and simulation chip morphology parameters: d , h_1 , and h_2 . Number of sample serrations measured: experimental, $n=100$; simulation, $n=4$. (C) Measured shear angle, frequency, and compressed chip ratio.

3.2.3 Electron Microscopy

The microstructure of the STA chips obtained at 61, 91, and 122 m/min were observed using a Tescan Mira scanning electron microscope (SEM) with an accelerating voltage of 25 keV, working distance of 15 mm, with a pole piece backscattered electron (BSE) detector. The crater face was also imaged with SEM with a magnification of 5000x. Orientation mapping of the chip microstructure was investigated using an Ametek (TSL) orientation imaging microscopy (OIM) system on a Tescan Mira, with a step size of 0.1 μm . OIM Analysis software v.8.5.0 was used to

clean the data using one generation of neighbor confidence index (CI) correlation and grain CI standardization.

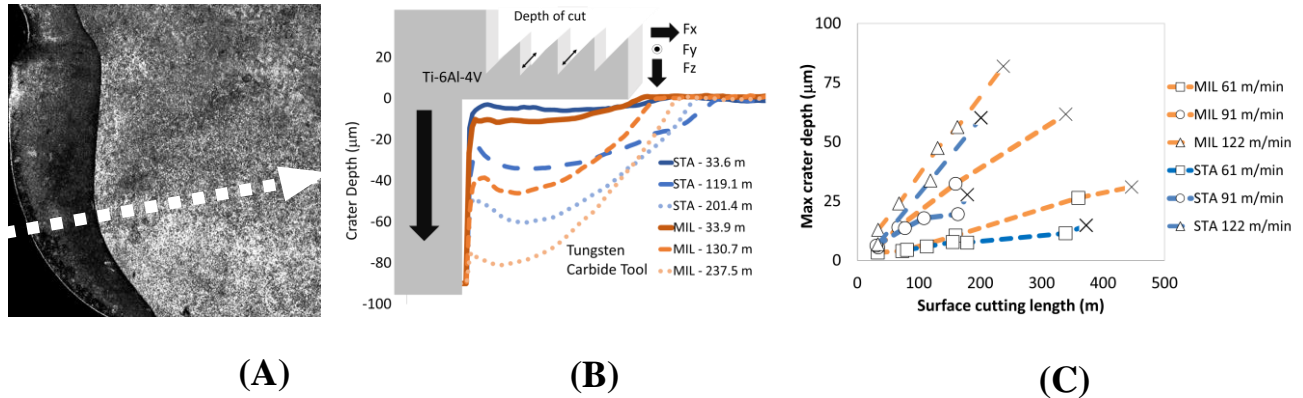


Figure 32. (A) Crater wear image after fracture when cutting STA at 122 m/s, white dotted line indicates the chip flow during machining; (B) 2-D profile of crater wear progression for MIL and STA at 122 m/s at different cutting lengths, with a schematic of chip formation and identification of cutting force directions in the cutting zone; (C) Crater wear at different cutting speeds for MIL and STA

3.2.4 Finite Element Analysis

To estimate the interaction between the tool and the work material, a 2-D FEA numerical simulation of machining the STA microstructure was performed using DEFORM 2D. v.11.2 commercial software. The numerical model was based on a plane strain orthogonal cutting geometry using a Lagrangian approach, which approximates turning with continuous re-meshing in the highly deformed chip [89]. The tool was modeled as a mechanically rigid body but thermally active low the temperature to rise during cutting. A heat transfer coefficient of $h=20 \text{ kW/m}^2 \text{ }^\circ\text{C}$, was used to allow fast heat conduction from workpiece into the tool, all initially at $20 \text{ }^\circ\text{C}$. The initial mesh had 6043 elements for the workpiece and 2477 elements for the tool. A $5 \text{ } \mu\text{m}$ mesh size was used in the workpiece close to the cutting zone with a constant friction coefficient (m) of

0.9 between the tool and workpiece to resemble sticking condition between the tool and the chip [37]

The STA workpiece was approximated with a modified Johnson Cook (JC) model (Eq.4) [36] and the constitutive flow stress model has the following form.

$$\sigma = \left[A + B \varepsilon^n \left(\frac{1}{\exp(\varepsilon^a)} \right) \right] \left[1 + C \ln \frac{\dot{\varepsilon}}{\dot{\varepsilon}_0} \right] \left[1 - \left(\frac{T - T_r}{T_m - T_r} \right)^m \right] \left[D + (1 - D) \left[\tanh \left(\frac{1}{(\varepsilon + p)^r} \right) \right]^s \right] \text{ Eq. 4}$$

Table 10. Material Constants and Parameters for Johnson Cook material model of Ti64-STA

<i>A</i>	<i>B</i>	<i>C</i>	<i>n</i>	<i>m</i>	$\dot{\varepsilon}_0$	<i>a</i>	<i>s</i>	<i>r</i>	<i>d</i>	<i>b</i>
838.5	712.4	0.033	0.3	0.89	10 ⁻⁴	2	0.05	1	1	5

The material constants for the STA flow stress are not reported as extensively as MIL [37], [90], [91] which were derived from a series of split Hopkinson bar tests. Thus, material constants were taken from Wang [92], where the STA microstructure was tested using a ball indent method. The strain rate dependency constant (*C*) was adjusted to 0.033 to yield a cutting force close to experimental measurements. Next, the material softening parameters were adjusted based upon the work of Ozel[37] to achieve the chip morphology (*d*, *h1*, *h2*) observed in the experiment. The resulting JC constitutive model parameters estimated are provided in Table 10. These parameters are considered as approximate, as the 2-D simulation represents orthogonal cutting rather than turning. The flow curves resulting from these adjustments are plotted in Figure 33A in blue, showing that the flow curves are above those of the MIL microstructure (orange) with material constants (*A*, *B*, *C*, *n* and *m*) adapted from Lee and Lin [90].

The simulated chip geometry parameters for STA simulation are plotted in Figure 31B (black lines and symbols) indicating reasonable correspondence with experimental values. The average

measured cutting force in three directions (F_x , F_y , F_z) are shown in Figure 33B. The forces are normalized by dividing the average force and the depth of cut. There is no significant difference or trend on the cutting speed with the average cutting forces measured. The experimental force is compared with the measured force from numerical simulation in Figure 33B (the $F_{y_sim} = 0$ because it is a 2-D simulation). The experimental cutting force in the z direction for STA (green bars) is higher than MIL (green diamonds) .

A cutting length of 1 mm was used in the FEA simulation to have enough chip length to see multiple segments while minimizing the computation time. Finally, the Cockcroft-Latham model damage criterion value was adjusted to a value of 2000 to make the chip segmentation size closer to experimental values (comparisons are provided in Figure 31B). In summary, this finite element approach started with model parameter values identified in prior work [11] and parameter adjustments were made to match experimental observations more closely.

Additionally, with the temperature and strain from the finite element simulation, 3-D stress tensor data (σ_x , σ_y , σ_{xy} , σ_z) was collected. Then the principal stress values and directions were calculated to estimate the deformation inside the chip. A matlab® code was utilized based on [93] to calculate the principal stress and directions, Code is shown in Appendix C.

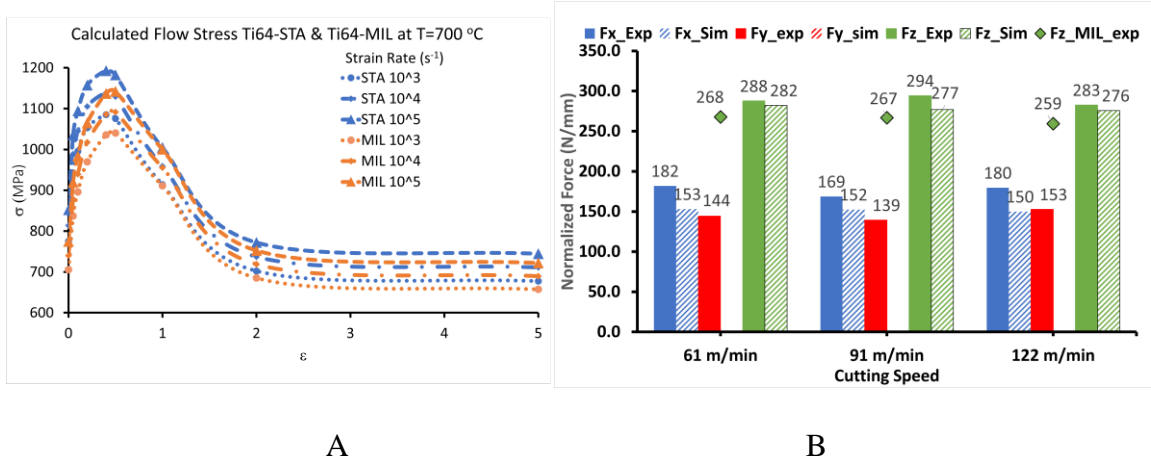


Figure 33. (A) Flow stress of Ti64-STA & Ti64-MIL calculated by modified JC model at 700 °C; (B) Measured experimental and simulated cutting force at different speeds

3.3 Results

3.3.1 Chip Morphology Analysis

. For all cutting speeds, the chip showed segmentation, but differences in the chip morphology between experimental and simulation d , h_1 , and h_2 , shown in Figure 31B and 31C are acceptable. The chip segmentation distance is close between experimental and simulation. Valley height h_1 of the simulated chip is higher than experimental, as cracks did not propagate in the simulation. The experimental peak chip height h_2 is higher than the simulated value at 91 m/min, this could be related to the grain variation in STA that could not be accurately simulated.

The measured segmentation frequency (f) values increased nearly linearly from 12.9 kHz at the low cutting speed to 25.7 kHz at the high cutting speed, which aligns with the frequency segmentation reported by Molinari [27]. From low to medium cutting speed (61 to 91 m/min) the average values of segmentation length, valley height, and peak height increase. However, at the highest cutting speed the morphology of d , h_1 , and h_2 decreases. Discussions in chapter 1 provided insight about the morphology change in STA chips during machining. There is no significant difference in the chip compression ratio (CCR) at different cutting speed values of 1.82, 1.84, and

1.78 with respect to increasing cutting speed. The measured shear angle was in the range of 40-42°, which is close to the idealized shear angle of 45° for flat tool cutting.

3.3.2 Wear Measurements

After machining, the worn tool corners from different cutting lengths and speeds were etched in hydrofluoric acid (HF) solution to dissolve the Ti adhesion layer and then the damaged tool was characterized using confocal laser microscopy (HF does not attack the Co binder in the tool). Flank and crater wear are two metrics used to assess tool performance. The flank wear results and analysis are extensively discussed in [11], which indicates that flank wear generated by the hard α grain orientations. Figure 32A shows the confocal image of crater wear on the fractured tool after cutting at 122 m/min. The dotted line shows the chip flow direction. The chip flow schematic and the force coordinate system during turning are shown in Figure 32B. The extracted two-dimensional profile of crater wear using confocal measurements after different cutting lengths in the MIL and STA microstructures in Figure 32B showed that MIL has deeper crater.

The maximum crater depth from the confocal images for both Ti microstructures is plotted in Figure 32C, indicating that the depth increased with cutting length, and the 'x' indicates tool fracture. While MIL craters are slightly deeper, the tool fractured earlier for the STA than the MIL grades. Compared to 61 m/min, the crater wear depth is about twice as deep for 91 m/min and about 5 times lower at 122 m/min

3.3.3 Finite Element Method Results

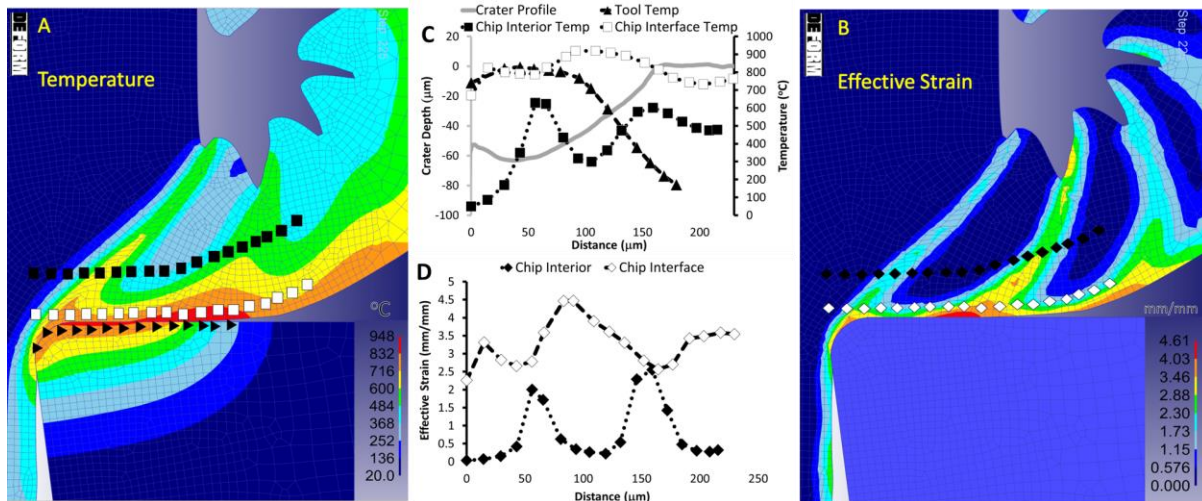


Figure 34. (A) Temperature field and (B) Effective strain in the Ti64-STA chip and tool with 1.2 mm depth of cut at 122 m/min, (C) values along marked elements and overlaid experimental crater wear profile at 122 m/min and 201 μm cut length, (D) Strain field of Ti64-STA chip along marked elements

As measuring the temperature and local strain during turning is difficult, finite element analysis was used to estimate the tool and chip temperature and the heterogeneous material deformation behavior inside the titanium chips at different speeds. Two distinct regions in the etched chip exhibit severe shear deformation as shown in Figure 31A. The primary shear zone (PSZ) originates from the tool tip and extends to the free surface of the chip. The secondary shear zone (SSZ) is along the interface between the tool and chip.

Figure 34 shows the FEM simulated strain and temperature fields inside the Ti64-STA chip during cutting at 122 m/min, which shows similar PSZ and SSZ features observed in the actual chip. Figure 34A shows the temperature field in the chip and the tool and similarly, Figure 34B shows the strain field. Figures 34C and 34D plotted the temperature and strain at the marked locations, one in the tool, near the SSZ interface, and the other at the depth of 55 μm from the interface inside the chip. In Figure 34C, the crater wear profile at fracture after cutting at 122

m/min is overlaid onto the temperature plot, which reveals that the highest temperatures during the chip formation are at the location of maximum crater depth. The values plotted are from the fourth chip ‘tooth’ that was in an approximately steady state condition at $t=2.6 \times 10^{-4}$ s. The temperature in the SSZ of the chip in the SSZ is higher than the tool and the interior of the chip and is located about 100 μm from the tip. From the strain plot in Figure 30D, the interface of the tool has higher strain values than the shear band within the chip with a maximum strain around 4.5. Within the chip, the higher strain values are concentrated in the PSZ with values that decrease significantly with distance away from the PSZ.

The strain fields for the other two cutting speeds are similar (not shown) but the higher speed produced higher strain values. For the three cutting speeds, the average temperature along the tool surface in the vicinity of the crater (width of 127 μm) was: $T_{61} = 504$, $T_{91} = 585$, and $T_{122} = 673$ °C. Inside the chip, there is a periodic temperature fluctuation corresponding with the PSZ, indicating that the temperature field is correlated with the plastic strain that causes adiabatic heat generation. In contrast, there is a constant velocity and sticking friction from the chip flow at the tool interface, therefore temperature less fluctuate on the tool. The average temperature, maximum temperature and effective strain estimated for each location and cutting speeds are presented in Table 11.

From the stress field inside of the chip in Figure 35, the shear stress (σ_{xy}) shows the highest stress values near the primary shear zone and at the tip of the ‘tooth’ around 800 MPa. The stresses mode are mostly in shear and tension. Additionally, the principal stress values and directions were calculated for 13x9 “points” inside of the chip formation for Ti64-STA at 122 m/min. For each points, the length of the principal stress vector indicates its values, with red means tension and blue is in compression.

Table 11. Summary of Maximum Temperature and Effective Strain from FEA Simulation

Cutting Speed (m/min)	Avg Temperature (°C)			Max Temperature (°C)			Max Effective Strain		
	61	91	122	61	91	122	61	91	122
Chip Interior	434	427	369	654	702	750	3.1	3.2	3.4
Chip Interface	741	791	814	854	907	946	4.2	4.2	4.5
Tool	504	585	673	794	848	909	-	-	-

Different points inside of the chip undergoes different mode of deformation. In the chip-tool interface or the secondary shear zone, the principal stress values and direction infers the material is highly in tension with the direction of the chip flow (horizontally). On the other hand, the tip of the tooth shows high tensile stress as the chip is forming. Figure 36 obtained from the experiments shows deformation in the α grains that closely resembles one simulated by FEM.

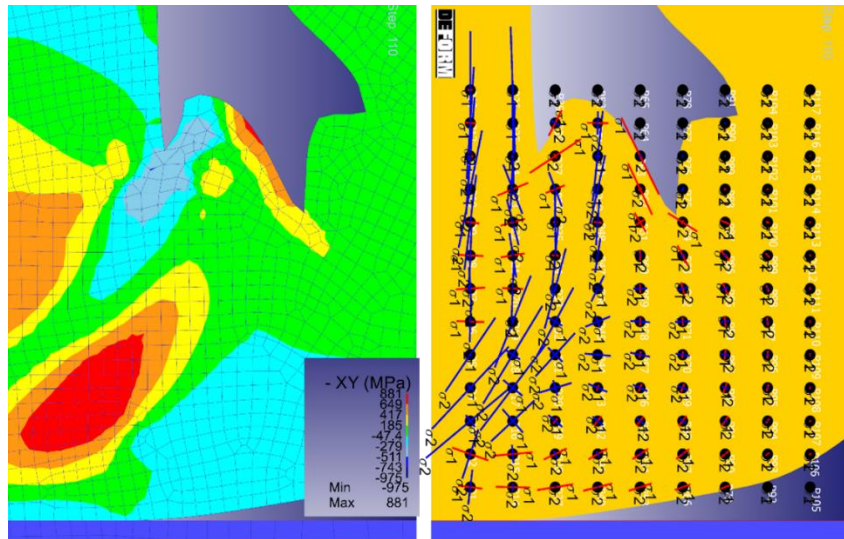


Figure 35. Shear Stress Field (σ_{xy}) in Turning Ti64-STA at 122 m/min (left) and The corresponding stress tensor inside the chip (right)

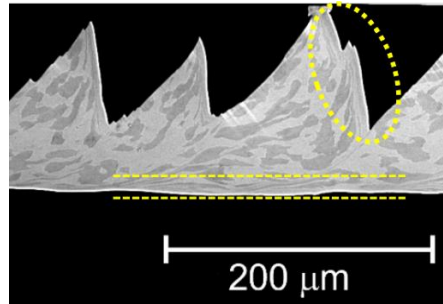


Figure 36. Experimental Chip for Ti64-STA at 122 m/min cutting obtained near tool fracture

3.3.4 Electron Backscattered Diffraction (EBSD) Analysis

A backscattered electron (BSE) image of a STA chip cut at 122 m/min is shown in Figure 35A. The darker phase in this image is the primary α while the brighter regions are the lamellar transformed β . In the undeformed material, the primary α is equiaxed, so the shapes of the primary α in the chip reflect the strain history. An EBSD scan conducted within the green dashed boxed region in Figure 37A is shown in Figure 37B. The primary α grains are clearly indexed and exhibit various orientations as indicated by their colors, while the transformed β region is not indexed as they are too deformed to generate indexable patterns (but it was successfully indexed in the undeformed material). The equiaxed green orientations in Figure 37B are more resistant to deformation than the red-orange orientations where prism slip is favored in the compression/shear stress state. Figure 35C shows the grain reference orientation deviation (GROD) map of the same region shown in Figure 35B.

An extremely large misorientation gradient exists in the red box region on the right side of the long orange primary α grain where it was locally sheared upward in the PSZ. The white color shows that the misorientation was larger than 15° from the average orientation in the α grain deformation. Along with the elongated shape of primary α grains parallel to the shear band, this implies that there must be a large amount of shear strain in the PSZ during the cutting process.

However, there is not much information acquired from the SSZ (yellow box). This could be caused by even larger shear strains in the SSZ, as seen in the highly elongated thin grains; even the α grain orientations could not be indexed. Orientation maps from 61 and 91 m/min STA chips show similar features, with variance in details such as the width of the PSZ, the presence of cracks, and the gradients in shear near the shear the PSZ.

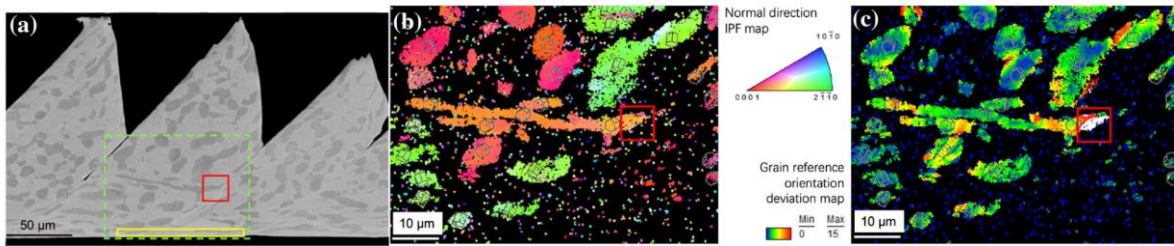


Figure 37. Backscattered electron image of Ti64-STA chip obtained at 122 m/min, showing the contrast of primary α (darker phase) and lamellar transformed β (brighter regions); (B) EBSD scan of the light green dashed boxed area shown in (A) revealing the α phase; (C) Grain reference orientation deviation (GROD) map showing orientation difference from the average α grain orientation

3.4 Discussion

From measurements of 100 serrations on a segmented STA chip, no apparent trend of morphology change was found with increasing cutting speed. Chapter 2 provides more detail on the different morphology of the cutting chip as cutting speeds are changed. While the microstructure in STA chips clearly shows evidence of adiabatic heating and localized deformation consistent with the finite element model and EBSD maps, the chip geometric details are highly varied from one segment to another. As the local stress and strain are known to be a strong function of crystal orientation in hexagonal alloys, this can account for the heterogeneous deformation and differing shear band morphology at each tooth. In Figure 29A at 61 m/min the two shear bands are not at the same angle, there is a crack in one but not the other, and the right side of the ‘tooth’ is straight in one but curved in the other. The microstructural variation could influence the chip morphology as much as the temperature and cutting speed

The crater wear rate was calculated as shown in Chapter 1 and plotted in Figure 38 for MIL and STA, showing a slightly higher measured wear rate for MIL. The crater wear rate increased by a factor of 15 above the rate at 61 m/min with doubling the cutting speed. The measured crater wear rate data were compared to the crater wear model by Hua and Shivpuri [16] in Eq.5.

$$W = \frac{2C_o}{\rho} \left(\frac{VD_o}{\pi x} \right)^{1/2} e^{-Q/2R(273+T)} \quad \text{Eq. 5}$$

The material coefficients are for cobalt: $C_o = 0.02 \text{ mole/mm}^3$, $D_o = 1.9 \text{ mm}^2/\text{s}$, $Q = 114.1 \text{ kJ/mole}$, $R = 8.32 \times 10^{-3} \text{ kJ/mole/}^\circ\text{K}$. V is the cutting speed and x is the distance between the edge to the center of the crater, $63.5 \text{ }\mu\text{m}$. This wear model was described as a diffusion of tool material by the chip in the following sequence: The cobalt binder phase was rapidly depleted through diffusion into the chip material, which loosened the WC grains. The loosen carbide grains were subsequently removed from the tool in a brittle manner. In the equation, the exponential term accounts for the temperature effect of cobalt diffusivity in the α phase.

The predicted wear rate from [16] is plotted in Figure 38 for MIL. For STA, the average tool temperatures from the finite element model in Table 10 was used in Eq. 5 to calculate the predicted wear rate for STA. Figure 36 shows that the model predicted MIL crater rate is higher than of predicted STA with tool temperature of $600\text{-}700^\circ\text{C}$ [94]. Experimentally, the wear rate of MIL and STA was measured to be close with each other. At 61m/min , the measured wear rate closely matched the predictive model from FEM of Ti64 STA. This infers that the tool temperature that produced crater wear at this cutting speed was close to $500 \text{ }^\circ\text{C}$, and the cobalt diffusion dominated the cratering process with Eq.5 above. With increasing cutting speed, the measured wear rate deviates more from the predicted wear rate. For 91 m/min , the measured wear rate was close to $12 \text{ }\mu\text{m/min}$, which is underestimated by the STA model and over-estimated by the MIL

model. At 122 m/min cutting speed the measured wear rate is significantly faster from both the MIL and STA model. Therefore, at 91 m/min and 122 m/min the tool temperature must be higher than predicted by the FEM or that the crater wear model is different.

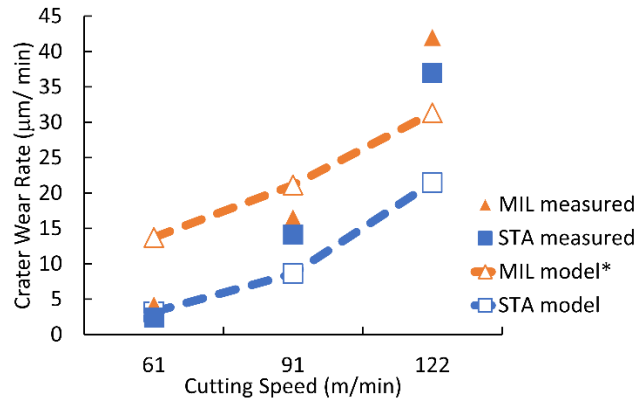


Figure 38. Experimental and Predicted Crater Wear Rate for Ti64-MIL and Ti64-STA.

* Data are from [68]; the tool was 600-700° C, but the chip temperature was not clearly identified.

At higher speed, especially at 122 m/min, the simulation may not account for a phase change (where at least some of the α within the lamellar re-transformed back to β). This would further accentuate the shear instability due to softer β and hence cause a more localized higher temperature due to a greater plastic instability. Hence, a more complex diffusivity model would be needed for a two-phase microstructure, as diffusivity of the tool constituents in β is at least few order of magnitude higher [95]. Figure 39 shows that cobalt is at least 2 orders of magnitude faster than carbon at temperature less than 882 °C (β transus temperature). Tungsten diffusivity at α phase is unknown, but as a ‘heavy’ element it is expected to be a slow diffuser. With increased temperature and phase change, cobalt diffusivity is slightly reduced. This is due to the change of the diffusion mechanism from vacancy to interstitial from α to β [96]. Carbon diffusivity, increased by three orders of magnitude at β phase of titanium. Hence, the increased temperature might alter the crater wear model to be exponentially faster at 91 and 122 m/min.

The temperatures required to account for the tool degradation rates (more than 1000°C) point to localized re-transformation to the β phase. Because the transformed β (lamellar) component in STA has high V content, which stabilizes the β phase, it is expected that the primary α phase with high Al would not transform easily to β and remain harder than the transformed β regions. This was shown as well at Chapter 2. At room temperature, the STA which contain more lamellar is stronger than the primary α phase (apparent in the higher flow curves of STA and MIL in Figure 33A), but it may soften faster with increasing temperature than the α phase, and due to an adiabatic temperature increase and presence of V, more β would form with increasing cutting rate, leading to a greater flow instability.

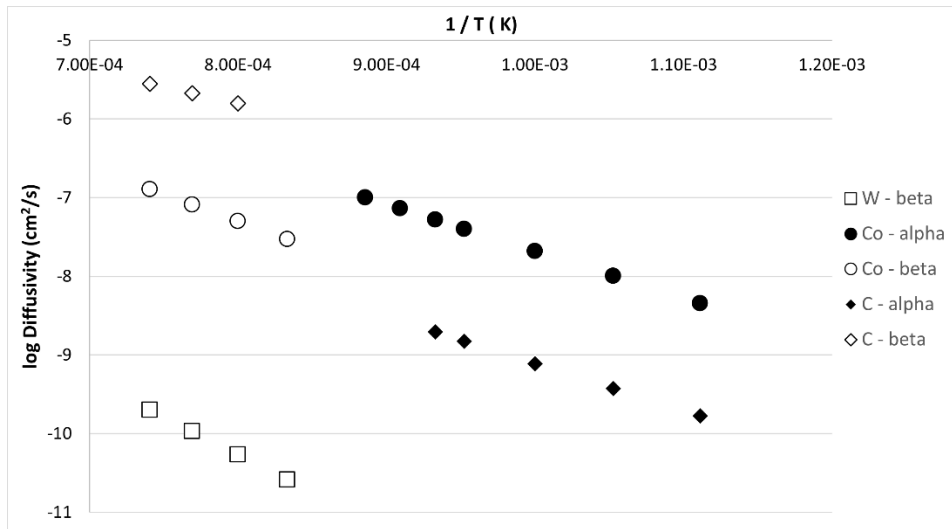


Figure 39. Diffusivity of Tool Constituents (W,C, and Co) in Titanium

Recently Graves *et al.* [97] reported on the mechanism of crater formation in machining Ti-5553, a metastable β Ti alloy. At a cutting speed of 72 m/min, they verified the initial crater formation mechanism reported by Hua & Shivpuri by the depletion of cobalt binder matrix. Then, it was found that decarburization of WC grains in the crater further erode the tool. It did not show rough carbide grain pull-out, but a smooth crater surface, as observed in our experiments. The

evidence from [97] showed region that has depleted cobalt yields a more stabilized β titanium and resulted in faster decarburization of carbide grains and reaction with the TiC adhesion layer forming above. According to Hartung [14] TiC layer formation is desirable due to it reduced crater wear, however at higher cutting speeds it is quickly removed so crater wear is high.

SEM images such as Fig 38 and Fig 39 were taken on the worn tool and the chip interface to observe cobalt diffusion and TiC layer formation. In Figure 38, the worn tool prior to etching showed built-up edge (BUE) and built-up layer (BUL) on the crater at machining of Ti64 STA at 122 m/min. At 2000x magnification, the crater surface showed adhesion layer and holes on the carbide surface. The porosity of the tool can be compared with the carbide image shown earlier in Figure 28. SEM EDX (Energy Dispersive X-Ray Spectroscopy) was conducted to find the compound of the adhesion layer, but it can only be detected as titanium. Therefore, it is inconclusive if TiC layer is formed due to the crater wear mechanism. EDX on the particles that latched on chip did could not detect TiC as well.

Figure 40 shows SEM images at of the crater wear surface after etching away the Ti adhesion at different cutting speeds. Similar to prior etch, porosity was found in the crater surface. Additionally, carbide grains with a rougher surface were observed. The cavity and rough surface indicated the cobalt diffusion and carbon depletion via decarburization of carbide grains.

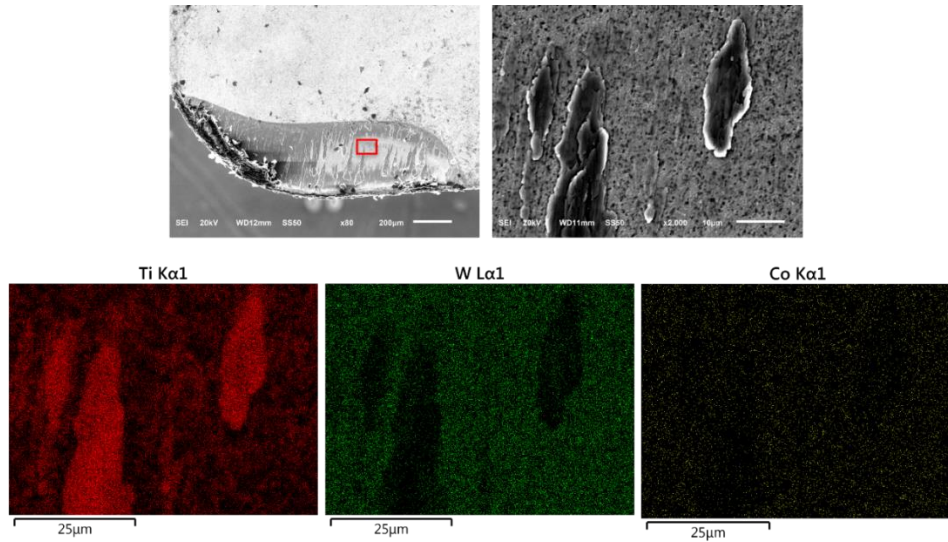


Figure 40. SEM images at 80x, 2000x for Ti64-STA at 122 m/min. With Elemental detection for Ti, W, and Co

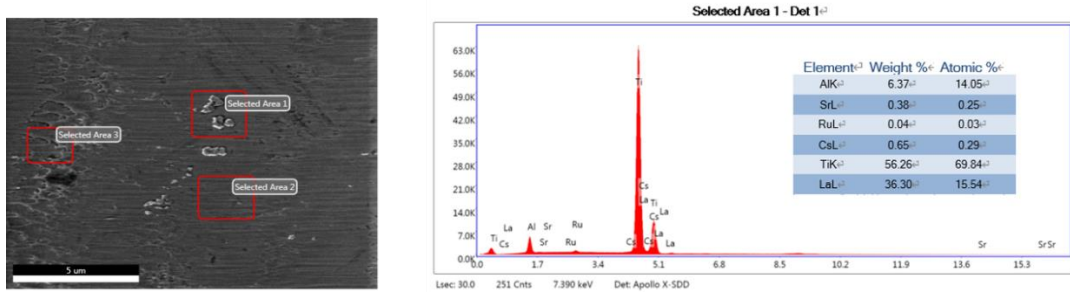


Figure 41. SEM images and quantitative element results for particles attached to the chip

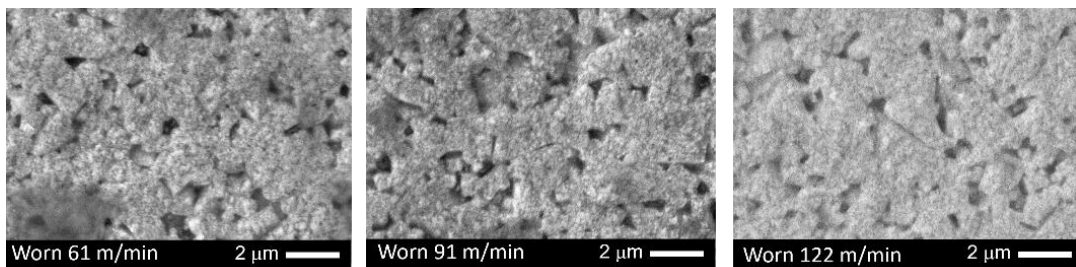


Figure 42. SEM Images at 10000x showing crater face of the carbide tool at different cutting speed

3.5 Conclusions

Turning experiments on MIL and STA microstructure Ti64 bars were carried out at of 61 m/min, 91 m/min, and 122 m/min and crater wear was measured for both microstructures. Chip

morphology at the onset of the cutting process was analyzed only for Ti64 STA. The STA chip morphology and force measurements were used to adjust the Johnson-Cook model parameters in the FEM simulation. Specific findings from this chapter are:

- 1) The segmented chip morphology of STA such as peak height, valley height, segment spacing and chip compression ratio (CCR) were similar among three cutting speeds, with variability that exceeded the differences in the average values. The EBSD grain map (to shows very high orientation gradients closer to the shear band) also indicates that much greater shear strain occurred in soft-oriented grains in the vicinity of the shear bands. Such features clearly show how microstructure affects and reflects local formation of adiabatic shear bands.
- 2)The simulation using the modified J-C constitutive model optimized to match the observed chip geometry for STA also showed good agreement with the experimental cutting forces. The effective shear strain results showed that a localized shear of about 3 occurred periodically inside the chip. From this model, the temperature in the primary and secondary shear zones could be estimated, and the simulated temperature of Ti64-STA could reach 950°C in the chip interface and 900°C in the cutting tool for STA at 122 m/min cutting speed.
- 3) Maximum crater depth of the carbide tool for both grades at 91m/min is twice that of 61 m/min and 5 times as deep at 122 m/min, indicating the strong dependence of tool wear on the cutting temperature. The discrepancy between the predicted crater wear rate and measured wear rate, provides evidence for a significant fraction of the material transformed to β at the cutting speed of 122 m/min. Which could account for more rapid diffusion of Co and Carbon into the titanium and faster crater wear

CHAPTER 4: A MACHINABILITY STUDY OF COATED INSERTS DURING THE MACHINING OF TI-6AL-4V SOLUTION TREATED AND AGED

4.1 Motivation

No coating material has been found to significantly improve the tool life in machining Ti alloys, in contrast to ferrous alloys, where for many decades, coated inserts has achieved astonishing improvement in tool life [98], [99]. Additionally, no ceramic tool material, such as : alumina (Al_2O_3), cubic boron nitride (cBN) and sialon (SiAlON) has been found to improve machinability in cutting titanium alloys [31]. Despite the tremendously high cost of ceramic tools, they are easily fractured during machining titanium when compared to uncoated carbide tools. These difficulties of different tool materials when machining titanium alloys stems from the low thermal conductivity, high reactivity, and high modulus. Therefore, an ideal tool material for cutting Ti alloys should have high thermal conductivity, chemical inertness, and high strength [13], [42]

To the best of author's knowledge, no comparative study on various types of coating materials and thickness in machining Ti alloys in relation to cutting speeds are available, which is the primary motivation for this chapter. This chapter focuses on the comparative machinability of a variety of coated tools including commercially available uncoated, coated inserts and novel coated materials such as BAM and $(\text{AlCrSi/Ti})\text{N}$ under various cutting speeds (61 m/min, 91 m/min, 122 m/min). The performance of these cutting tools will be assessed using cutting force data, flank wear, and crater wear measurements.

4.2 Experimental Setup

A straight turning experiment was conducted in dry condition on a CNC Lathe (TL01, Haas Automation Inc®, California, USA). The Ti-6Al-4V workpiece in the STA microstructure was provided by Rolled Alloys, Inc (Temperance, Michigan, USA) with an outer diameter of 125 mm and length of 673 mm. The details of the chemical properties of the workpiece are presented in Table 1. Three cutting speeds, low (61 m/min), medium (91 m/min), and high (122 m/min), were used while the depth of cut and feed rate were fixed at 1.2 mm and 0.127 mm/rev, respectively. The cutting forces in three cutting directions were measured during the turning experiments with a Kistler stationary dynamometer (Kistler Instrument Corp., Amherst, NY) including a Piezo-Multicomponent Stationary type 9257B Dynamometer, type 5070A Multichannel Charge Amplifier, type 5697A acquisition system and type 2825A Dynoware. The detailed experimental setup for our turning experiments is shown in Chapter 2.

Uncoated flat carbide square inserts with a rake angle of 0° and relief angle of 7° (SCMW 432-H13A / 120408, Sandvik-Coromant®, NJ, USA) were used in the experiment. Cutting inserts without a chip breaker was used to eliminated cutting temperature variations on the rake face. Two commercially available tools recommended for heat resistant super alloy (HRSA), SCMT432-MM1115 (finishing machining) and SCMT432-MM1125 (rough machining), were used . These tools have a TiAlN coated carbide inserts. Five additional coatings of AlMgB₁₄(BAM), Al_{0.66}Ti_{0.34}N, Ti_{0.5}Al_{0.5}N, ZrN, and (AlCrSi/Ti)N on the uncoated carbide tools noted above were deposited by Fraunhofer CCL (East Lansing, MI, USA) using a physical vapor deposition (PVD) technique. These inserts were used to turn the workpiece until the inserts fractured.

Two different coating thicknesses of (AlCrSi/Ti)N, 3 and 7 μm thick, have alternating layers of AlCrSiN and TiN. AlCrSiN is a chemically stable material with high hot hardness [100]. It has

a nanocomposite structure which AlCrN (alcrona) is embedded in an amorphous Si₃N₄ (silicon nitride) matrix. Figure 43 shows the layered structure of the AlCrSiN/TiN and nanocomposite structure of AlCrSiN. In the nanocomposite structure, around 80% is the AlCrN grain (darker) and 20% is the Si₃N₄ matrix. Typically, (AlCrSi/Ti)N processed to attain the thickness of 3 to 4 μm and the coating used in our experiment attained the thickness of 3.3 μm and thus denoted (AlCrSi/Ti)N3. The coating processing was repeated to attain additional thickness with the final thickness of 6.7 μm, which denoted as (AlCrSi/Ti)N7. BAM is a relatively new coating material in the market benefitted by a large reduction in friction, which may potentially benefit machining Ti alloy[101]. Similar to the (AlCrSi/Ti)N coating, the process was repeated to attain BAM6 but could only be grown to the final thickness of 5.9 μm, slightly less than twice the thickness of BAM3. A summary of the cutting inserts used in this experiment is presented in Table 12.

There were two methods of measuring the coating thickness, one is by cutting the coated tool in the cross section and using SEM – EDX to do a 1-D line scan to detect the coating elements. The second method is calotte test. The calotte test was conducted at Fraunhofer CCL by grinding the coated tool with a ball indenter, then the resulting cavity corresponds to a certain thickness. Both coating measurements results were comparable. Figure 44 and 45 shows the schematics of the coating measurements

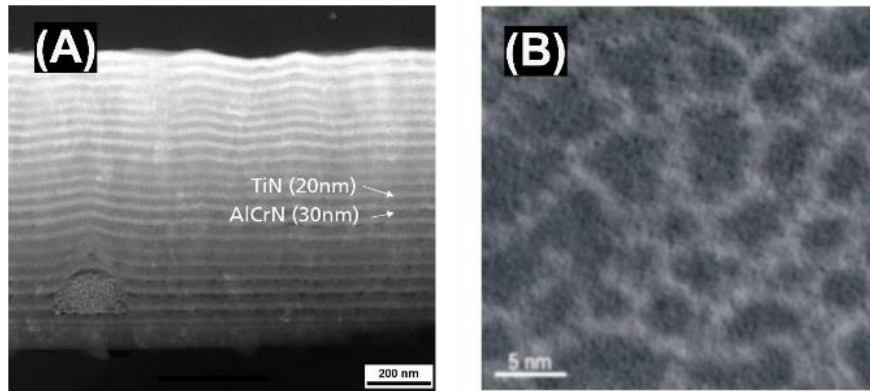


Figure 43. (A) Multilayer (AlCrSi/Ti)N Coating (B) Nanocomposite Structure of AlCrSiN layer

Table 12. Uncoated And Coated Inserts Layer Thickness

Coating types	Layer thickness (μm)	Layer structure
Uncoated carbide	-	-
MM1115	1.8	Single layer
MM1125	3.6	Double layers
BAM3	3.5	Single layer
BAM6	5.9	Double layers
AlTiN	1.3	Single layer
TiAlN	2.3	Single layer
ZrN	2	Single layer
(AlCrSi/Ti)N3	3.3	Multi layers
(AlCrSi/Ti)N7	6.7	Double of Multi layers

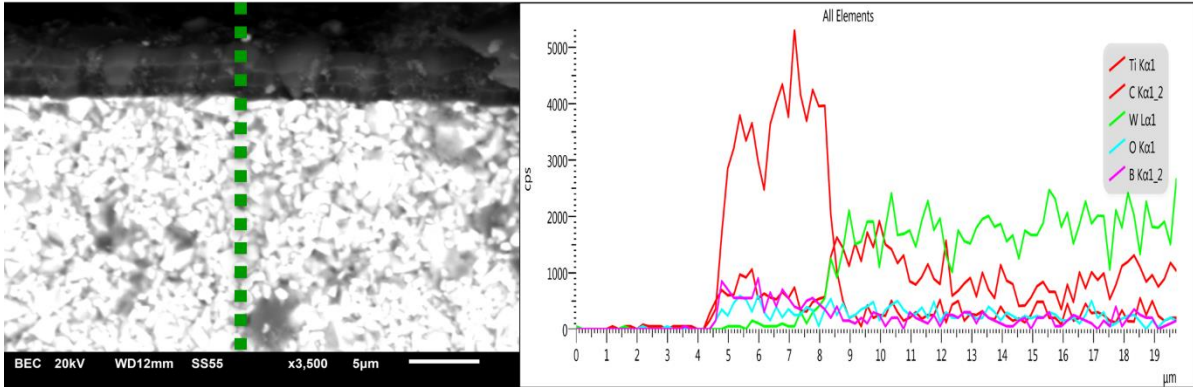


Figure 44. SEM image of the cross section of the coated tool and energy dispersive x-ray spectroscopy signal, showing the coating thickness.

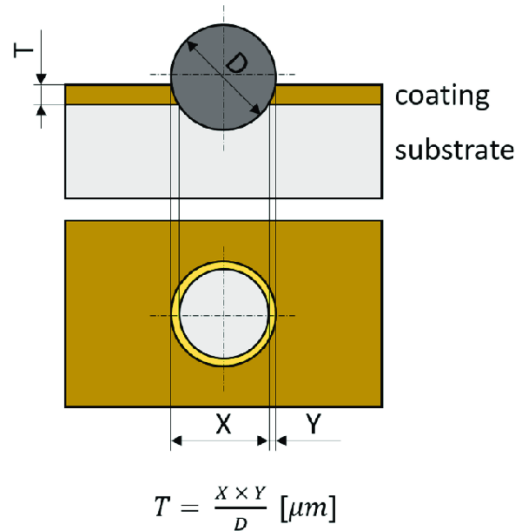


Figure 45. Calote Test method [102]

4.3 Wear Measurement

After turning experiments, adhesion layers were apparent on the cutting inserts. The adhesion layers covered the worn areas, which must be removed before making the wear measurement. Two different methods were used to remove the adhesion layer. Uncoated and AlTiN tools were submerged in a concentrated HF (hydrofluoric acid) solution. (AlCrSi/Ti)N, BAM and ZrN coated inserts required a mechanical steel brush to remove the adhesion layers because a Ti interlayer was

deposited on the carbide substrate prior to depositing each coating. This Ti interlayer was necessary for these coatings to stick to the carbide substrate.

Flank and crater wear images were captured using an Olympus Fluoview FV1000 Confocal Laser Scanning Microscopy (CLSM) system with the magnification of 20x, and a step size of 1 μm . The CLSM data including the conjugal focal plane images were overlapped to generate the height encoded images (HEI). The wavelet-based algorithm constructed in MATLAB [81] was used to eliminate the noise from the HEI images. Finally, the 2D profiles of the flank and crater wear were extracted from three-dimensional images to quantify the extent of wear. The steps of the wear measurement used in this study were presented in Figure 46.

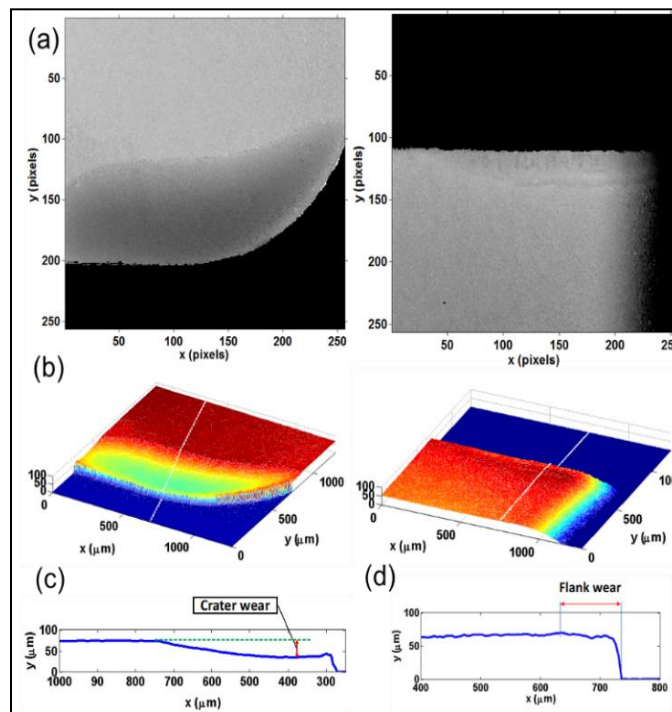


Figure 46. Tool Wear Measurement Using 3D Confocal Images (A) HEI Images, (B) 3D Processed Surface (C) 2D Profile of Flank Wear and (D) 2D Profile of Crater Wear.

4.4 Results

TiAlN coated inserts with 2.3 μm thickness experienced premature failure at the beginning of the turning experiments. Initial observation of the tool surface shows that the coating did not adhere well to the tool surface because it flaked off at the cutting edge and flank face of the inserts as shown in Figure 45. Thus, no additional experiments were carried out for this coating. However, TiAlN coated inserts could be improved but requiring a significant effort to design a stronger interlayer bond between the TiAlN coating and the carbide substrate.

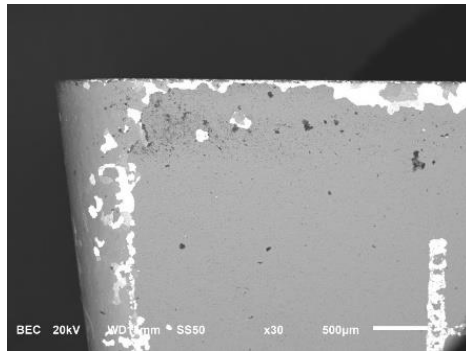


Figure 47. Flank Surface Image of TiAlN Coated Insert.

Two grades of commercially available coated inserts, MM1115 and MM1125, also prematurely failed during turning. Inserts were severely worn and fractured as shown in Figure 48. At the cutting speed of 61 m/min, the failure of MM1115 grade and MM1125 happened after cutting for 81 and 55 seconds, respectively. At the cutting speed of 122 m/min, the failure occurred much sooner at 13 and 10 seconds, respectively. Figure 46 presents the SEM images of the rapid failure and chipping observed on both inserts. Tool MM1125 (rough machining) failed more catastrophically than the MM1115 tool. Due to both premature failures, no further work was conducted on these coated tools. For the rest of the inserts, the turning experiments in the conditions described in section 4.2 were carried out.

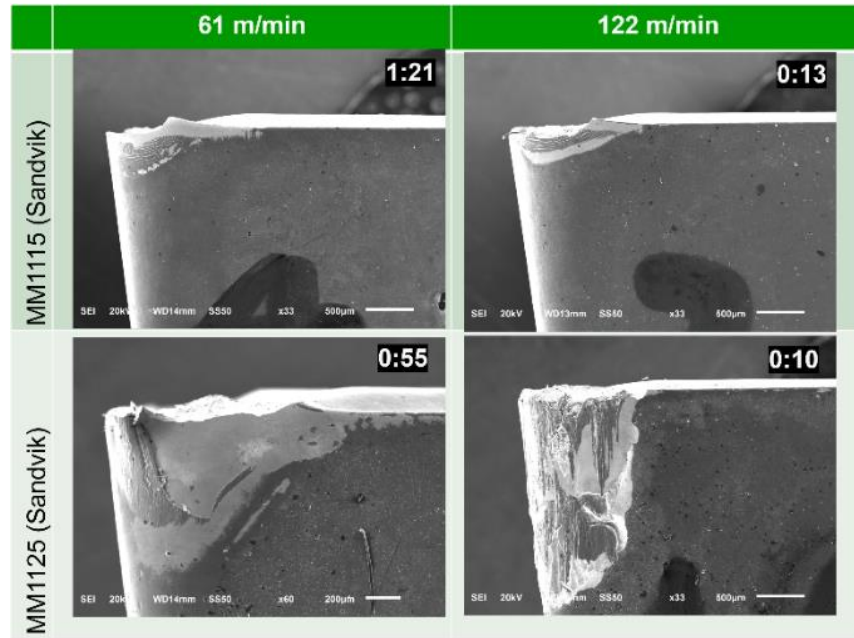


Figure 48. Scanning Electron Microscope Images of the MM1115 And MM1125 Coated Tool.

4.4.1 Cutting Force

Figure 49(A) shows a schematic of the force components measured with the dynamometer during the turning experiments. F_x , F_y , and F_z components of the force data were recorded with the sampling rate of 100 Hz. Figure 47(B) presents the force signals measured throughout one complete cycle of the turning experiments. When the insert fails or fractured, the forces in all three components immediately increase as shown in Figure 49(B) at the cutting time of 150 seconds. The average and variation of all three force components were assessed at the beginning of a turning experiment prior to any significant accumulation of tool wear on the inserts.

Figure 50(A) presents the average F_x , F_y , and F_z forces for all cutting tools used. It has been reported that the BAM coating has a low friction coefficient [103]. However, our measurements show that neither the BAM3 or BAM6 coatings reduced the force components in comparison to the uncoated carbide. For other coatings as well, there is no significant difference in the forces when compared to the uncoated tools.

Figure 49(B) presents force variation (max – min) from F_x , F_y , and F_z . The force variations are smaller at a higher speed for all inserts. Less variation of measured forces at higher cutting speed indicates a more stable deformation process. At all cutting speeds, BAM3 has the lowest variation in the cutting force (F_z), indicating a relatively stable cutting process suggesting that the coating survived the turning process and did not flake off easily.

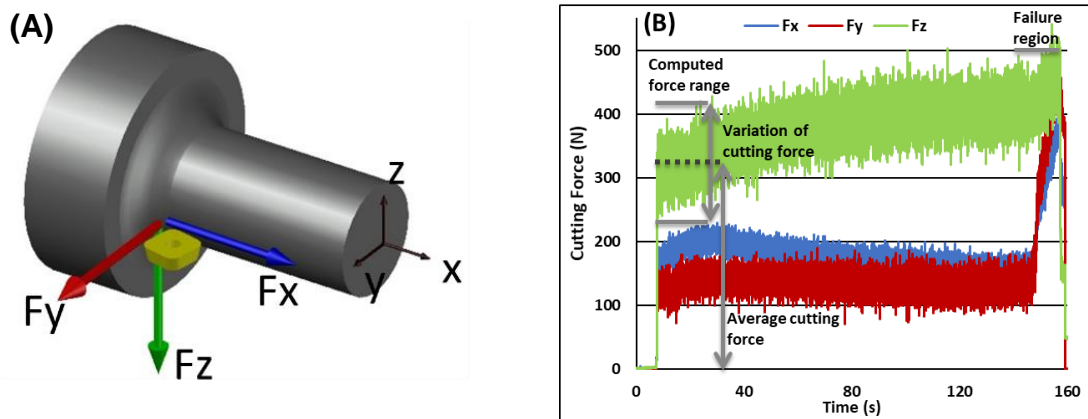


Figure 49. (A) Cutting Forces Components in Turning (B) Measured Cutting Forces of Uncoated Carbide Tool at 122 m/min

4.4.2 Tool Wear

Figure 51 presents the confocal images of all inserts at the final or fractured stage for both flank and crater faces with the recorded cutting time. The collection of these images shows the differences among the fractured inserts. Flank wear shows large areas of abrasion and sometimes a large portion of tool material fractured off. Crater surfaces generally showed a smooth surface indicating chemical dissolution and/or diffusion has occurred. Some inserts like BAM3, BAM6 and ZrN show severe fractures on the crater surface as well, while uncoated carbide, AlCrSiN, and AlTiN has a smoother surface.

Figures 52 and 53 show the progression in flank wear and crater wear for each insert. Figure 52(A), (B) and (C) presented the flank wear chart for low, medium, and high cutting speeds, respectively. The typical tool life is reached when the flank wear land is reached 300 μm . The flank wear plot typically shows a primary wear process with a decreasing wear rate followed by a secondary wear rate that is nearly constant, and then a tertiary sudden increase of wear rate leading to fracture.

At the low cutting speed, all coated tools have longer tool lives than the uncoated carbide tool, which can only cut until 500m at the cutting speed of 61 m/min. In comparison, the (AlCrSi/Ti)N7 coated inserts had the longest life and the insert did not fracture even after cutting for almost 1400m. Cutting had to be halted due to the limited workpiece length. The thinner (AlCrSi/Ti)N3 failed earlier after reaching the cutting distance of about 900 m. The next best coating was BAM3 which cuts up to 1100m. Interestingly, the thickness affected the coating performance in the opposite way; the 6 μm thick BAM6 coating failed sooner than BAM3. This may result from a greater amount of internal stress damage resulting from thermal stress generation while cooling after depositing both coatings, BAM and (AlCrSi/Ti)N. As will be discussed, (AlCrSi/Ti)N7 reduced flank wear compared to (AlCrSi/Ti)N3. Measurement of the residual stress in coatings as a function of thickness will be the subject of a future research.

In terms of crater wear, as shown in Figure 52(A), the uncoated carbide insert shows the crater depth of 30 μm during fracture. At the same cutting distance, the crater depths of (AlCrSi/Ti)N7, BAM3, and BAM6 are less than the uncoated carbide insert. With increasing cutting speed, the crater depth increased for all three of these coatings, in particular, (AlCrSi/Ti)N7 reached the crater depth of 80 μm at the longest cutting length without fracture. The crater wear progression is relatively constant as cutting length increases. Thus, the crater wear rates are determined by

dividing the crater wear depth to the cutting time. All results of crater wear rate are summarized in Table 4. At the low speed, the inserts wore in the crater at the rate of 2.4-5.3 $\mu\text{m}/\text{min}$.

At the medium speed of 91 m/min, all cutting inserts fractured except BAM3 before reaching the cutting time of 5 minutes. Uncoated carbide tools fractured after cutting around 4 minutes while BAM3 inserts lasted the longest at the cutting distance of 500 m or the cutting time of 6 minutes. As with the low cutting speed, the BAM6 fractured sooner than BAM3. The (AlCrSi/Ti)N7 coated insert, which performed well at the low speed, did not work at this speed. The thickness of the (AlCrSi/Ti)N coating did not impact the tool life as the tool lives for both thickness of (AlCrSi/Ti)N coating were around the cutting distance of 350m. From the flank wear and crater wear chart, the best tools at the medium speed were BAM3 and uncoated carbide. The crater wear rate is significantly increased to 10.4-18.1 $\mu\text{m}/\text{min}$.

When cutting at the high speed, all inserts wore down much faster and fractured sooner with the tool life less than 2 minutes. From the confocal images of the flank wear, severe attrition wear occurred on the BAM and ZrN coated inserts. Upon the inspection of the crater wear images, even the (AlCrSi/Ti)N7 coated tool has some rough surface areas in the crater, indicating attrition. It is widely known that crater wear is dominated by the dissolution/diffusion wear at high cutting temperature. The flank and crater wear plots show that BAM3 survived the longest at high cutting speed at cutting distance around 320m. This is reflected by smaller crater depths in comparison to other inserts. When comparing the crater wear rate, the wear rate for each insert is increased significantly at the rates between 28.9 and 49 $\mu\text{m}/\text{min}$.

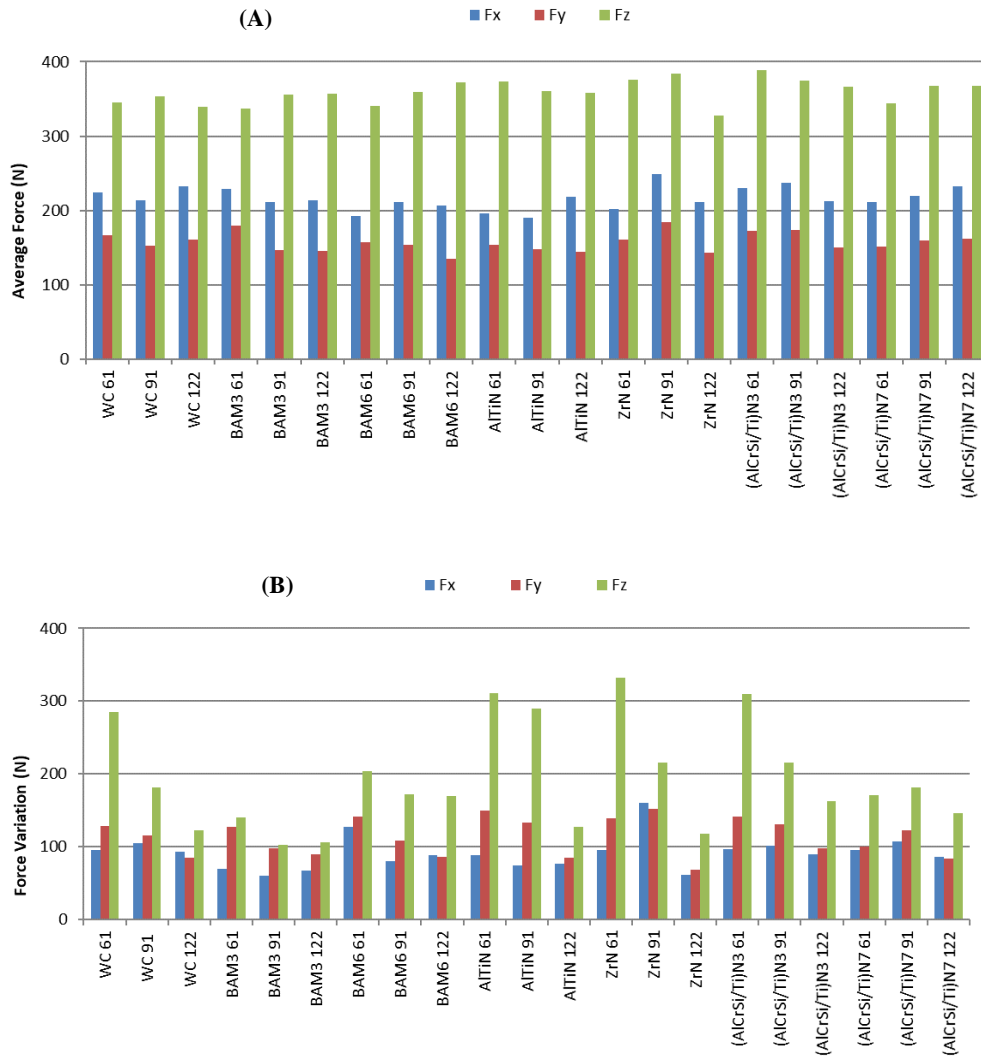


Figure 50. (A) Average Normal, Tangential, and Cutting Forces change to F_x , F_y , F_z and (B) Force Variations in F_x , F_y , and F_z for Each Coating and Cutting Speed

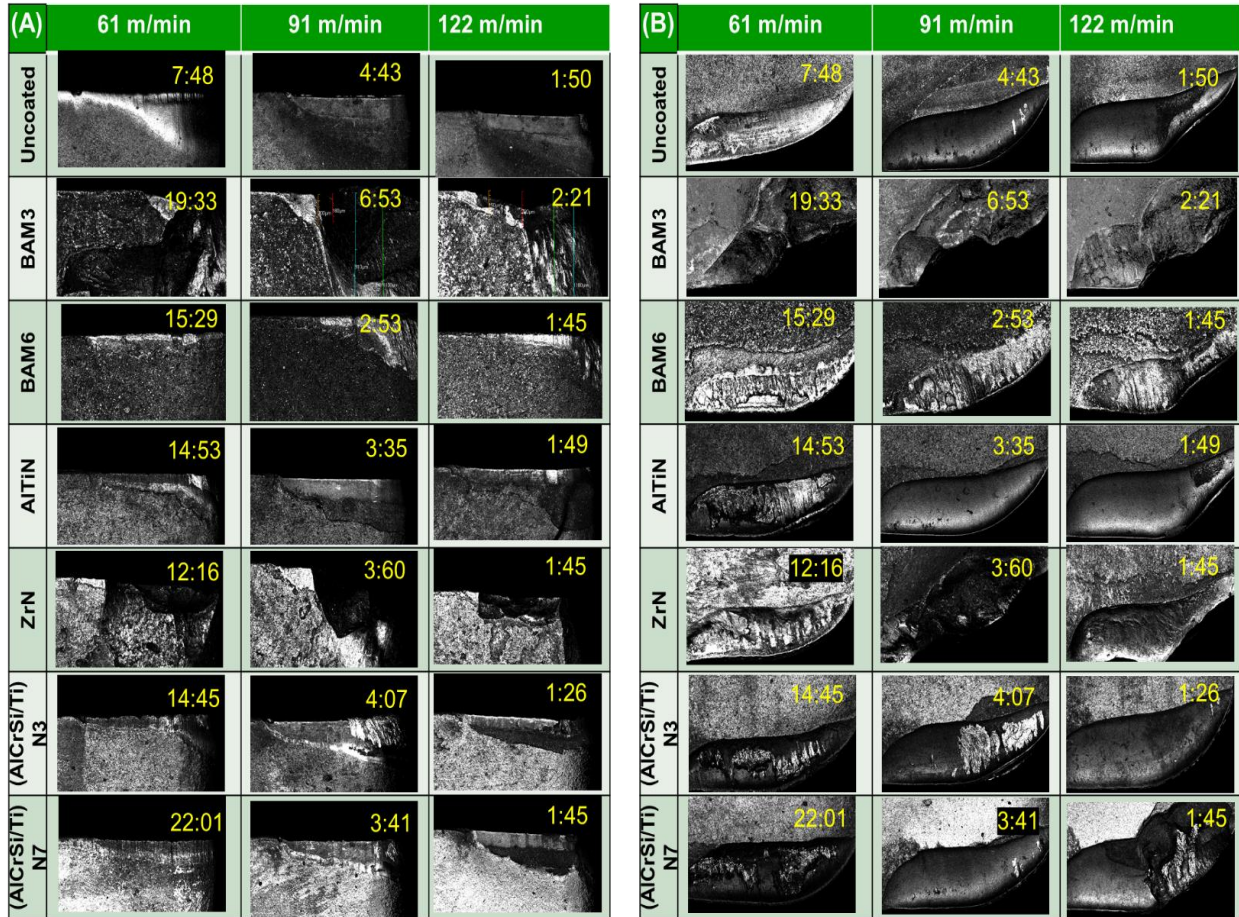


Figure 51. (A) Flank Wear And (B) Crater Wear Confocal Images of The Worn Tool After Turning Titanium Alloys for All Cutting Speeds

4.5 Discussion

Table 14 presents the room temperature hardness data for uncoated carbide and other coating materials used in this study obtained from literature. Because of the thin coatings with multiple nano-layers, attempts to measure hardness of used tools was unsuccessful. From the literature, the room temperature hardness of all coatings are higher than the uncoated carbide, and the (AlCrSi/Ti)N material was the hardest (at least at room temperature). Generally, all coating materials tested in this experiment improved the tool life for low cutting speed as seen from the

flank and crater wear chart. This suggests that hardness is significant factor in improving machinability. In particular, the (AlCrSi/Ti)N7 coated inserts exhibited the best performance, which could be related to the highest hardness. However, if hardness is the only important factor, the (AlCrSi/Ti)N3 tools should achieved similar performance, but it did not.

In previous work [11], the microstructural features responsible for abrasive wear when cutting the Ti alloys are the clusters of the α phase grains with ‘hard’ orientations and the lamellar phase colonies, which are significantly larger than the hard inclusions and cementite phases ferrous alloys. The 3-4 μ m coating thickness improved the tool life significantly in cutting ferrous alloys. It has also been reported that the thicker the coating is, the more wear resistant it becomes with turning experiments with 4340 steel [104]. In comparison, machining Ti alloys required much thicker coatings to protect against abrasion by larger sized ‘hard’ orientations in Ti alloys. Hence, a combination of hardness and thickness of the double-multilayer (AlCrSi/Ti)N7 coating inserts could explain why this material performs superbly at low cutting speed when compared specifically to (AlCrSi/Ti)N3, as the greater thickness appears to be able to resist impact of hard orientations whereas the smaller thickness does not. The good performance of the alcrona-based material is in line with our previous results in which (AlCrSi/Ti)N coated tools for drilling Ti-6Al-4V plates [46] improved machinability when compared to uncoated tools.

At a higher cutting speed, the cutting temperature increases significantly more than other metallic alloys due to the low conductivity of Ti alloys. Our previous finite element method to estimate tool temperature during cutting of Ti-6Al-4V STA shows that the cutting temperature can reach at least 900°C at the speed of 122 m/min [105]. Therefore, at higher cutting speed, more heat is ‘trapped’ in the cutting area. Generally, the hardness of the tool material also degrades, and the wear resistance of the coating is compromised. In the experiment reported in [106], by heating up

a tungsten carbide substrate with AlCrN coating in a high temperature (800-900C) environment for 7 days, it was found that the coating become oxidized with multiple pits and voids on the surface that weakens the surface integrity. Furthermore, the substrate material has oxidized as well [106]

. The present data suggests that the (AlCrSi/Ti)N₇ coated inserts have less protection against tool wear at elevated temperature, causing it to fracture at both medium and high cutting speed. In addition, higher temperature also accelerates the dissolution and diffusion wear. This wear is considered chemical wear which affects the formation of crater wear by the means of rapid decomposition of tool compound and transporting to work material. This is also known to be the dissolution/diffusion mechanism.

The evidence of rapid wear at elevated temperature can be observed from the crater wear rate on Table 13. At medium and high cutting speeds, the wear rates are many orders of magnitude higher than those at low cutting speed. It is theorized that at low speed, the main form of wear is dominated by abrasion with the minor contribution from chemical wear. At higher cutting speed the dissolution/diffusion wear becomes the main mode of material removal in the tool. Hua and Shivpuri [94] developed a model based upon cobalt diffusion that governs the crater wear rate for uncoated carbide inserts. They reported that the cobalt binder in the carbide insert is a fast diffuser in Ti, and with higher temperature, more cobalt diffused into the work material. However, their model still overestimates the crater wear rate in comparison to the experimental wear data. Additionally, the dissolution and diffusivity of different materials might affect the crater wear rate.

Hartung [14] reported that dissolution of the tool material has a large influence on the crater formation of the tool. The solubility indicates the maximum amount of material that can dissolve in a solvent. The solubility of compound (A_xB_y) can be calculated by estimating the Gibbs free

energy of formation and enthalpy [14] into Ti matrix. However, due to the scarcity thermodynamic properties on some of the coating material in this study, the solubility was approximated by the least soluble component within the tool [14] as it is reported that the solubility of compound must be limited by the least soluble element of the compound.

Table 15 presents the solubility data of the different tool elements in the coatings used in this experiment. Solubility of elements were taken by tracing the element maximum weight (atomic %) that can be soluble in Ti at certain temperature based on the binary phase diagrams [3], [107][108], [109]. Please note that the solubility needs to be divided by their stoichiometric ratio. At 800°C, Ti is mainly in the α phase and at 1000°C in the β phase.

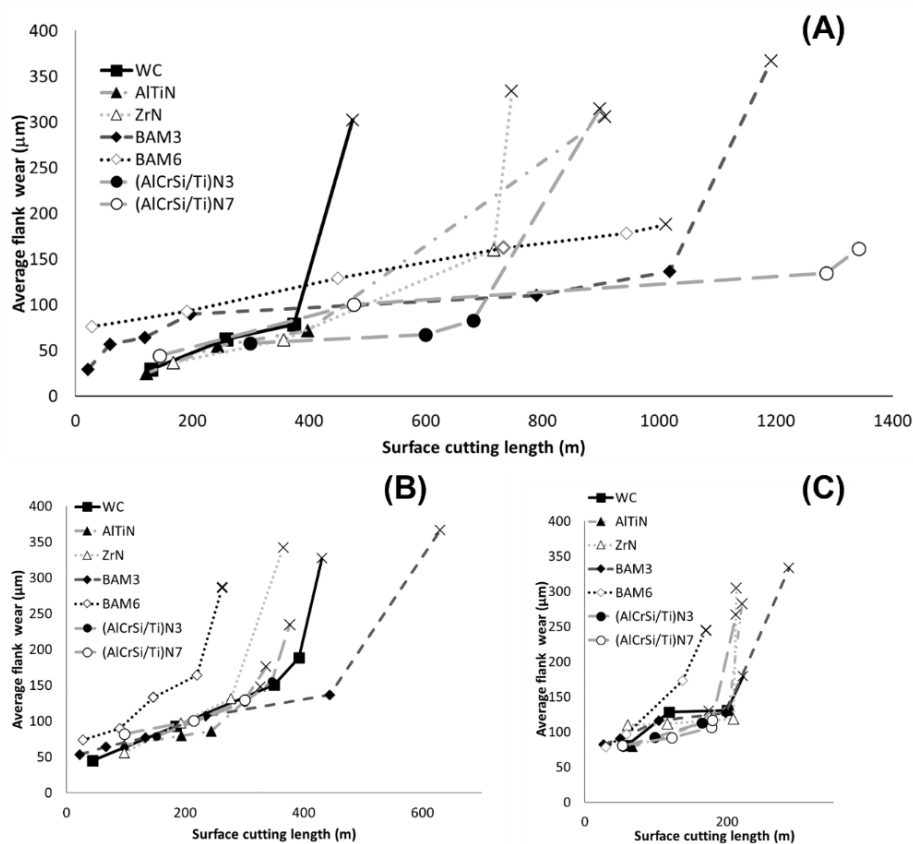


Figure 52. Flank Wear Curves of (A) 61 m/min, (B) 91 m/min, and (C) 122 m/min

As an example of solubility estimation, the BAM coating ($B_{14}AlMg$) consists of 3 elements: B, Al, and Mg. Each element has its own solubility limit with Ti as shown in Table 15 with different temperatures. Then, the lowest solubility among these elements was selected as the compound or tool solubility limit at each temperature. At $800^{\circ}C$ and $1000^{\circ}C$, the solubility of BAM was limited by the solubility of B. The data shows that B on $B_{14}AlMg$ is the least soluble in Ti as shown in Table 15. The solubility is further reduced by dividing the solubility value to the number of boron atoms in the compound (14). In contrast, Al is more soluble in Ti. For the $(AlCrSi/Ti)N$ coating, the solubility is estimated as the combination of the solubilities of the alcrona ($AlCrN$) and silicon nitride (Si_3N_4).

The other factor in chemical wear of tools is diffusivity. Diffusion indicates how fast each atom moves into a matrix of another element. In the context of tool wear, this determines how rapidly the dissociated elements in the tool material move within the chip. At higher temperature, the atom can diffuse faster. Interestingly, low soluble elements tend to be fast diffusers and vice versa. Diffusion wear was estimated by the element tracer diffusivity, which is calculated based on temperature in Ti. Figure 54 shows the Arrhenius plot of element diffusivity in pure titanium adapted from various sources [14], [95], [110], [111] The diffusion follows the formula as below:

$$D = D_0 \exp(-Q/k_B T) \quad \text{Eq. 6}$$

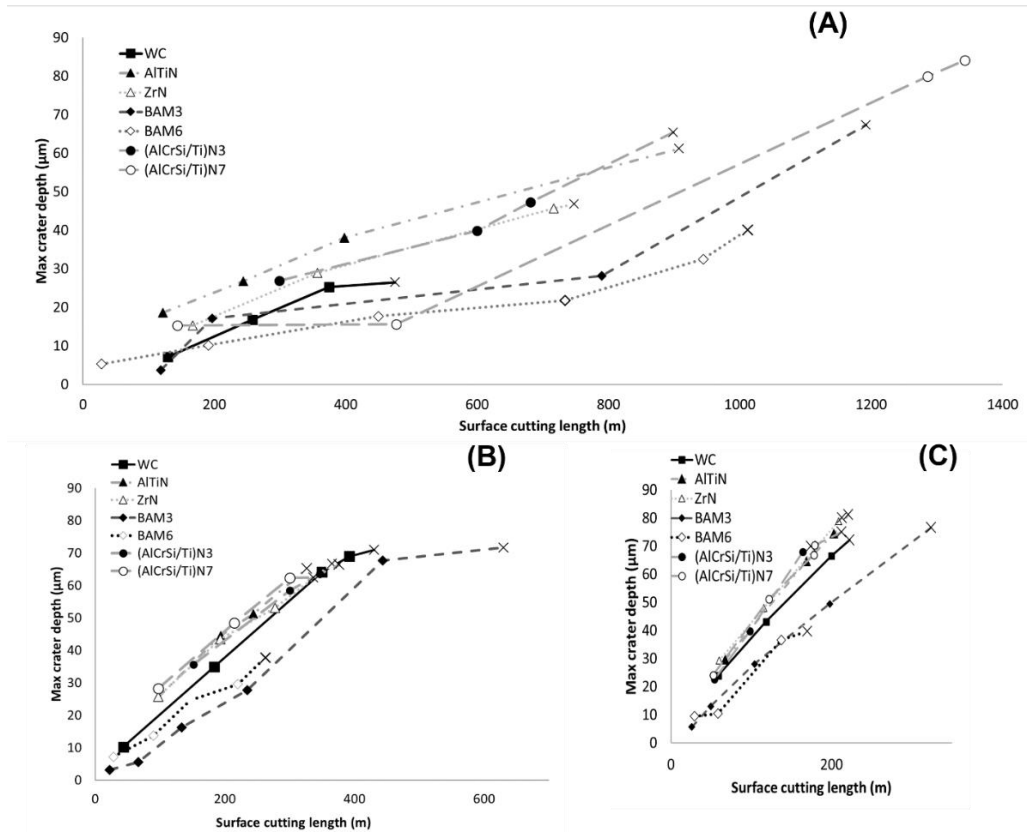


Figure 53. Crater Wear at the Cutting Speeds of (A) 61, (B) 91, and (C) 122 m/min

Table 13. Crater Wear Rate at Different Cutting Speeds

Speed (m/min)	Crater Wear Rate (mm/min)		
	61	91	122
WC	3.4	15.0	39.6
AlTiN	4.1	18.1	44.8
ZrN	3.8	16.6	45.9
BAM3	3.4	10.4	28.9
BAM6	2.4	13.1	28.5
(AlCrSi/Ti)N3	4.4	16.0	48.9
(AlCrSi/Ti)N7	5.3	16.9	43.1

Table 14. Room Temperature Hardness of Various Coating Materials and Substrate

Coating material	Hardness (GPa)	Ref
WC	23.5	[112]
AlTiN	30.7	[113]
ZrN	28	[114]
BAM	30-32	[101]
(AlCrSi/Ti)N	35-40	[44]

Table 15. Solubility Limit at Different Cutting Speeds. (*) means the element is fully soluble in Ti.

Tool (A _x B _y C _z)	S _A (at.%) in α-Ti (800° C)	S _A (at.%) in β-Ti (1000° C)	S _B (at.%) in α - Ti (800° C)	S _B (at.%) in β - Ti (1000° C)	S _C (at.%) in α - Ti (800° C)	S _C (at.%) in β - Ti (1000° C)	S _{Tool} (at.%) in α - Ti (800° C)	S _{Tool} (at.%) in β - Ti (1000° C)
WC	0.2	16.5	0.9	0.6	-	-	0.2	0.6
B ₁₄ AlMg	0.1	0.3	15.3	8.4	0.6	1.2	7×10 ⁻³	0.02
AlCrN	15.3	8.4	0.47	28	11.2	1.1	0.47	1.1
Si ₃ N ₄	1	2.5	11.2	1.1	-	-	0.33	0.28
AlTiN	15.3	8.4	*	*	11.2	1.1	11.2	1.1
ZrN	8	*	11.2	1.1	-	-	8	1.1

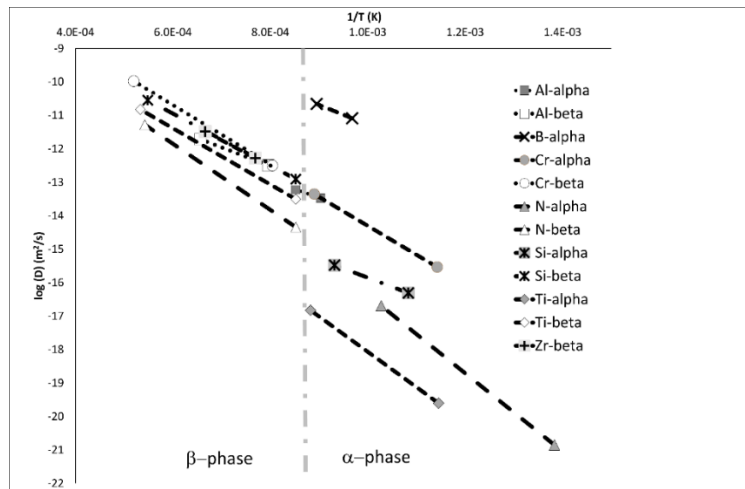


Figure 54. Diffusivity data of different elements in Ti.

At 800°C, Ti is mostly in the α phase, and the uncoated carbide, BAM ($B_{14}AlMg$), and alcrona material shows low solubilities into Ti. However, at lower speed, it is more likely that abrasion wear is more dominant than chemical wear; therefore, the low solubility/diffusivity level did not affect the wear observed in the inserts. When the temperature rises to 1000°C with Ti in β -phase, BAM shows the lowest tool solubility compared to other inserts, up to 10 times lower. At higher machining speeds, temperature could reach 1000°C [6] and the solubility of tool materials could now influence the machinability of Ti alloy. Between 800 and 1000°C, the fraction of β -phase in Ti increases from a few % to 100% in a non-linear way.

The low solubility of BAM may account for the lowest crater wear in general on BAM3 at medium and high cutting speed but the tool life is short-lived with inevitable fracture. In addition, BAM6 fractured much earlier at medium and high cutting speeds but still retarded crater wear. This performance of BAM coating may indicate that the coating is more resistant at elevated temperature, where abrasion becomes secondary to chemical wear. This phenomenon is observed similarly our previous work in drilling Ti/CFRP stack plate [45] where the BAM coated drill reduced wear significantly at the high speed (800rpm) compared to the low speed (400rpm).

Regarding the diffusivity in the α and β phases, Al shows low diffusivity values in both phases. On the other hand, B shows a much high diffusivity in the α phase. Due to the lack of B diffusivity data into the β phase, it is assumed that the diffusivity in the β phase is two orders of magnitude higher than that in the α phase. Mg diffusivity data are also unknown so far. Based on the composition of BAM, significantly more boron atoms are present. Thus, it is highly possible that for BAM coating, diffusion wear was governed by the rapid diffusivity and low solubility of B. Hence, despite the low solubility of BAM implying a less amount of B atoms available to be dissolved, the dissociated B atom may be quickly diffused away from the insert.

Hartung [14] suggested that the diffusion wear of material in the machining process can be approximated by:

$$V_{diffusion\ wear} \left(\frac{m}{min} \right) = -K.S. \sqrt{\frac{D}{\pi t}} \quad \text{Eq. 7}$$

Which K is the ratio of molar volumes between the chip and tool material, S is the solubility of the least soluble component, D is the diffusivity of the slowest diffusing component and t is the chip travelling time from edge to the center. For the cutting speed of 122 m/min and the feed rate of 0.127 mm/rev, the estimated time is 4×10^{-5} s. The diffusivity of element is calculated based on the temperature of 1000 C. Eq 7 is based on the work of cook & Nayak [115], and estimated the upper bound of the diffusion wear rate. The molar volume and diffusivity data were taken from a reference handbook [95]. The summarized wear rate is then shown in Table 16. It was calculated that among the coating material, combining the effects of dissolution and diffusion, that BAM coating wear rate is the lowest. Recalling information from Chapter 3, the tungsten carbide wear rate is dominated by the cobalt diffusion and is around 40 $\mu\text{m}/\text{min}$ at 122 m/min, therefore, since the wear rate of BAM is low, it could provide some protection and reduced the crater wear, in comparison to the other coating.

Table 16. Wear Rates of Different Coating Materials at 122 m/min and 1000°C

Coating Material	Ratio Of Molar Volumes	Slowest Diffusing Component	Diffusion Coefficient (cm ² /s)	Solubility (at %)	Predicted Wear Rate (cm/s)	($\mu\text{m}/\text{min}$)
AlTiN	1.93	N	2.09E-10	1.1	2.65E-05	15.9
ZrN	1.40	N	2.09E-10	1.1	1.93E-05	11.6
BAM	7.18	Al	2.42E-09	0.02	6.12E-06	3.7
AlCrN	1.49	N	2.09E-10	1.1	2.05E-05	12.3

4.6 Conclusions

This chapter presents a series of turning tests of various coated inserts compared with uncoated inserts on Ti-6Al-4V alloy with the STA microstructure. Two commercially available coated

carbide tools and five material types of novel coated carbide tools were tested at low, medium, and high cutting speed. Among various advanced coatings, (AlCrSi/Ti)N and BAM seems to provide some promise in protecting against tool wear under certain conditions despite the premature fracture which is more mechanical failure not gradual wear. With regards to tool wear, the main points that may be drawn from this study are:

1. Some tools, namely the MM1115, MM1125, and TiAlN coated carbide inserts, failed prematurely when turning the STA microstructured Ti-6Al-4V alloy. Fracture is due to coating flaking and possibly oxidation.
2. The nanocomposite coating (AlCrSi/Ti)N with the thickness of 6.7 μm ((AlCrSi/Ti)₇) increased tool life by a factor of three compared to other tools with the cutting speed of 61 m/min. As the cutting speed increases, the coating is no longer effective as the main wear mechanism changes from abrasion to the dissolution/ diffusion wear. However, (AlCrSi/Ti)₃ did not offer any benefit in resisting tool wear.
3. The BAM coatings (BAM3 & BAM6) resisted both flank and crater wear and slightly extends tool life at medium and high cutting speeds due to the low solubility of the elements. The estimated diffusion wear rate was calculated to be as low as 3.7 $\mu\text{m}/\text{min}$. The tool eventually fails due to attrition from the titanium layer

CHAPTER 5: MINIMUM QUANTITY LUBRICATION (MQL) USING DIFFERENT SOLID ADDITIVES OR MACHINING Ti64-STA

5.1 Motivation

The industry usually applies flood cooling lubricant to reduce cutting temperature and achieve better surface roughness to solve issues with machining titanium and difficult-to-cut alloys. Minimum quantity lubrication (MQL) adds cutting fluid with a meager flow rate of less than 0.2 mL/hour [102], providing sufficient lubrication to the cutting zone. The addition of the typical cutting fluid constitutes about 16-20% of the manufacturing cost [116]. However, most cutting fluids are disposed of after use with low recyclability and pose a health problem to workers [117]. [55]The benefit of using MQL method over traditional flood cooling is the reduced cost, more manageable cleaning, and reduced health pollutants [118]. As stated earlier in the literature review, it is still unclear which solid lubricants would work best in machining Ti64 with MQL. Therefore, in this chapter, the machinability of Ti64 STA was studied using uncoated and (AlCrSi/Ti)N-coated carbide tools with the aid of minimum quantity lubrication and additives. The machining performance was analyzed using cutting force, flank, and crater wear.

5.2 Experimental

The workpiece in this experiment is Ti64-STA (solution treated and aged), and the experimental section in Chapter 2 presents the machining setup. MQL system from Uni-MAX (Unist Co., Grand Rapid, MI) was utilized to produce the oil mist. The base lubrication oil used was Rapeseed oil of Unist© *Coolube* 2210 mixed with different additives. Based on the previous study [56], we utilized an optimized nozzle position at 15° yaw and 15° pitch angle on the tool rake side.

Table 17. Experimental Details

Workpiece	Ti-6Al-4V (Solution Treated and Aged)
Cutting Speed & Feed	122 m/min; 0.127 mm/rev
Lubricant	Oil (Coolube 2210) mixed with Micro-and Nano-platelets
Nozzle Position	15° yaw and 15° pitch angle
Air pressure	8 psi
Flow rate	1.5 mL min
Nozzle distance	50 mm

Initially, the machining experiments used flat tools of uncoated and coated carbide. However, the chip produced during machining frequently became entangled with the MQL nozzle and blocked the desired lubrication. The phenomenon is commonly known as a 'bird-nest' effect. A chip breaker tool (Figure 55) with the same carbide grade was selected (SCMT 12 04 08-KR H13A) to reduce the chip entanglement. An (AlCrSi/Ti)N PVD coating with a thickness of 7.5 μm mm was applied to the chip breaker tool by Fraunhofer CCD. For brevity, the coated tool is labeled as AlCrSiN. Figure 57 shows the coating measurements obtained by using the scanning electron microscope. Due to limitations in the process, the coating in the rake side only reached 4.5 μm thickness.

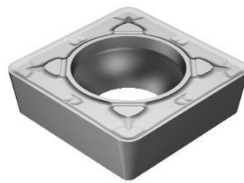


Figure 55. Cutting Tool SCMT 12 04 08-KR H13A

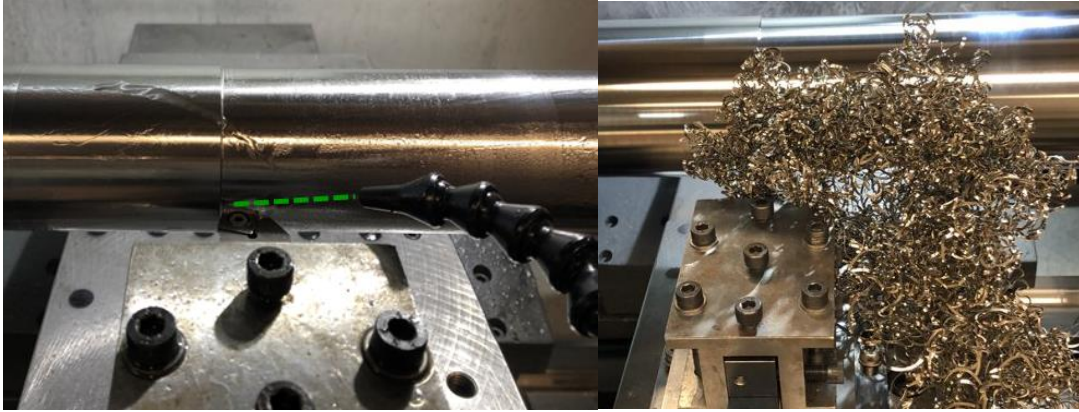


Figure 56. Experimental Setup of the MQL turning(left), “bird-nest” effect from turning (right)

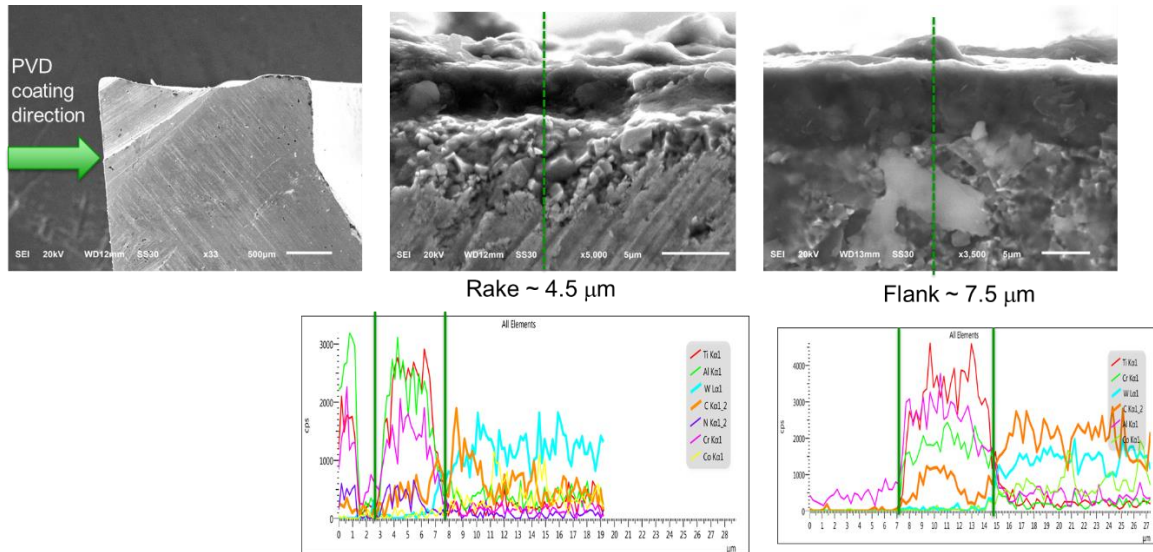


Figure 57. (AlCrSi/Ti)N Coating on the carbide tools

Different types of solid lubricants (additives) and sizes were mixed in the oil to enhance the lubrication during machining titanium : hBN, WS₂, MoS₂, and xGnP. Hexagonal boron nitride (hBN) has been widely used as solid lubricant [3] [119], [120] due to its thermal stability and good friction properties. Tungsten disulfide (WS₂) and Molybdenum disulfide (MoS₂) are sulfur-based additive which are widely used due to extremely low friction properties [121]–[123] and low level of toxicity [124]. Exfoliated graphite nano-particles (xGnP) are an improved graphite based solid

lubricant that have high aspect ratio and high surface area, allowing it to have better performance [3], [56]. Each platelet is varied in size and properties, as shown from the scanning electron images in Figure 58 and summarized in Table 18.

The [56] solid lubricants are mixed with the oil by a high-speed mixer DAC 150FVZ-K from *FlackTek* (Landrum, SC). at 23000 rpm for 10 minutes. The resulting mixture is relatively stable after mixing, but after 72 hours, the hBN and WS₂ were dissociated, while MoS₂ was still mixed (Figure 59). The xGnP mixture was also stable after 72 hours [56]. The concentration level of 0.5% of mixture weight (0.5 wt%) was used based upon the previous experiments wherexGnP showed extended tool life for machining Ti64 STA [56] .

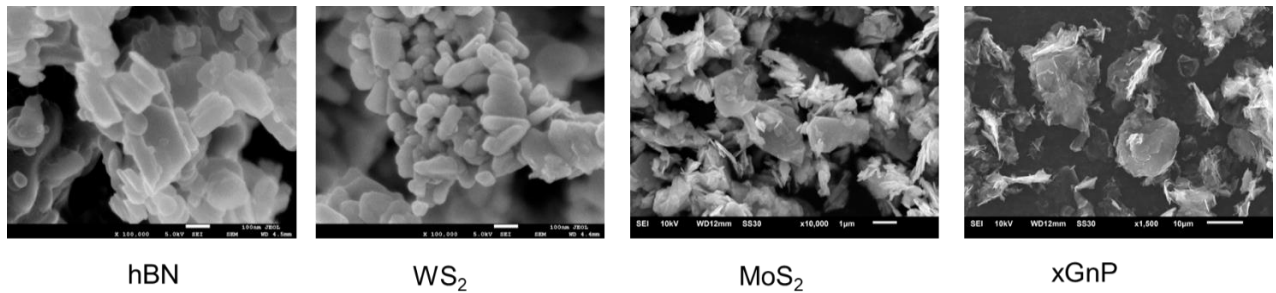


Figure 58. Scanning Electron Microscope of various additives at different magnification

Table 18. Solid additives (platelets) mixed with oil

Platelets	APS (diameter)	Thickness	Aspect Ratio (APS/thickness)	Surface area (m ² /g)	Friction Coefficient	Temperature Stability (°C)	Company
hBN	70 nm	~27 nm	2.5	19.4	0.15-0.7	1000	Lowerfriction
WS ₂	90 nm	~30 nm	3	30	0.03-0.07	650	Lowerfriction
MoS ₂	1.5 μm	~10 nm	150	30	0.03-0.1	594	Lowerfriction
xGnP M5	5 μm	6-8 nm	~700	120-150	0.2-0.6	500	XG Sciences

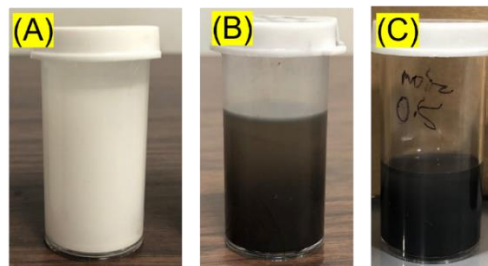


Figure 59. Mixture stability after 72 hours (A) hBN 0.5wt% (B) WS₂ 0.5wt% (C) MoS₂ 0.5wt%

5.3 Results & Discussions

Figure 60 shows the average cutting force in three different directions: feed force (Fx), radial force (Fy), and cutting force (Fz). AlCrSiN coated tools have a larger cutting force when compared to uncoated tools. The increased force is due to a thicker coating and tool radius. When lubrication was applied, the response was not consistent; in some cases, the force was reduced, and in some, it was increased. The least cutting force was recorded for the uncoated tool with the MoS₂ lubrication. The cutting force (Fz) was reduced from 329N in the dry condition to 308N when lubricated with MoS₂, which is a 6% force reduction. The feed and radial forces, it were reduced by 16% and 19%, respectively.

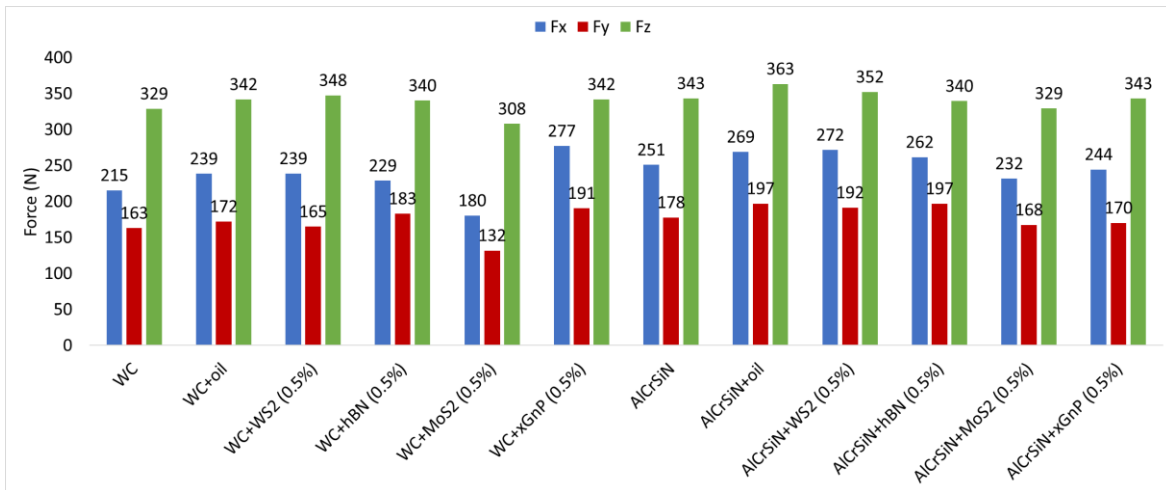


Figure 60. Average force of turning uncoated and coated tools for different lubrication

Effects of MQL on flank wear are shown in the light microscope image of the flank face of the uncoated carbide tool before cut and after fracture, with MoS₂ lubrications in Figure 61. On the top of the flank wear land, it showed some carbide grains were exposed due to attrition. Besides attrition, plastic deformation also occurs during fracture, where the tip of the cutting tool is pushed inwards. Confocal images of the flank wear at fractured are shown in Figure 62 with flank wear chart presented in Figure 63. For the uncoated carbide, MoS₂ additive works best by extending

tool life to 462 m, up to 58% improvement from 292 m of cutting length with dry cutting. Flank wear land is also the least with the MoS₂ additive. For the AlCrSiN tools, the MoS₂ extend the tool life to 393 m from 335m of dry cut, a 17% improvement. Additionally, AlCrSiN tools have a significantly reduced flank wear land when MQL was applied with various additives. However, the tool eventually fractures.

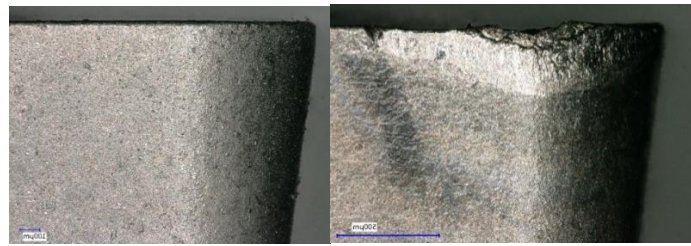


Figure 61. Flank face of the fresh and worn tool after machining with MoS₂ lubrication

Coating +Lubrication	Flank Wear at Fracture	Coating +Lubrication	Flank Wear at Fracture
WC Dry		AlCrSiN Dry	
WC+Oil		AlCrSiN+Oil	
WC+WS ₂ (0.5%)		AlCrSiN+WS ₂ (0.5%)	
WC+hBN (0.5%)		AlCrSiN+hBN (0.5%)	
WC+MoS ₂ (0.5%)		AlCrSiN+MoS ₂ (0.5%)	
WC+xGnP (0.5%)		AlCrSiN+xGnP (0.5%)	

Figure 62. Confocal Images of flank wear during fracture

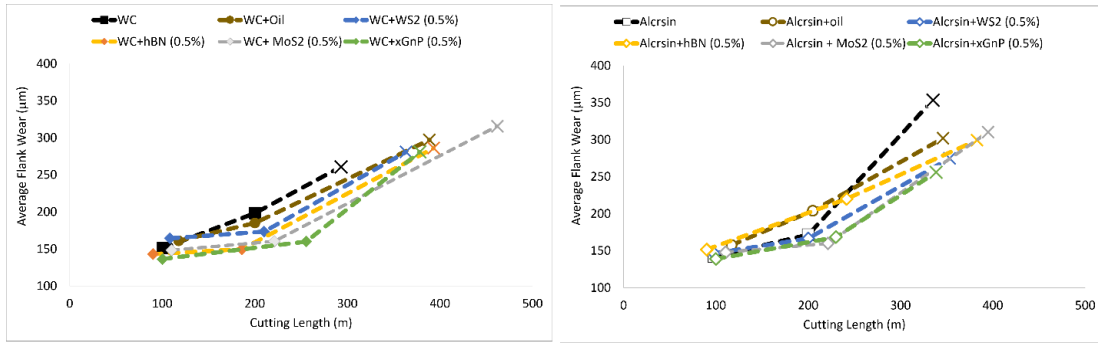


Figure 63. Flank wear chart for WC and AlCrSiN tools

The crater wear profile of the AlCrSiN tool is shown in Figure 64. The 2-D shape was extracted from the confocal image from the same region at different lengths, then adjusted at the same height reference. The light microscope image of the rake face (Figure 65) more clearly showed the attrition and the plastic deformation of the tool during fracture. The chip-breaker geometry has an inclined ‘hump’, allowing higher stress concentration where plastic deformation is more likely to occur. With the flat tools that were used in previous chapters, attrition in the rake face was more common.

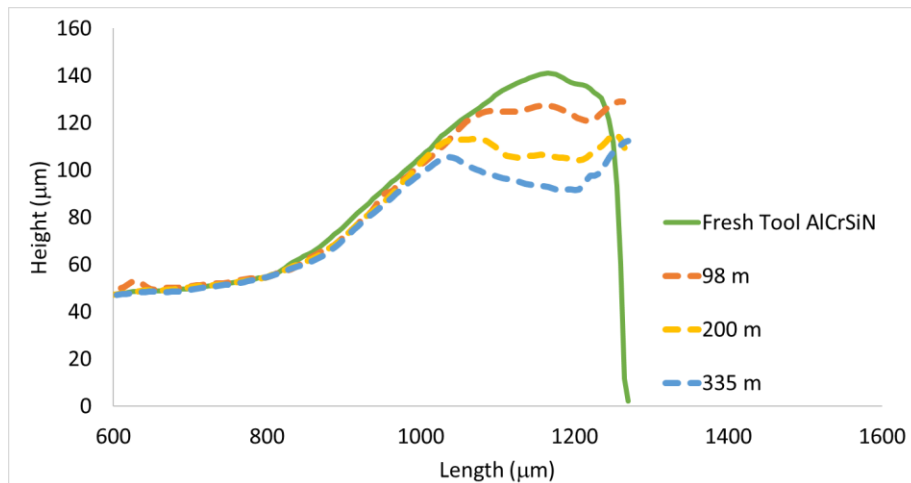


Figure 64. Crater wear progression in AlCrSiN tools during dry cutting.



Figure 65. Rake face of the fresh and worn tool after machining with MoS₂ lubrication

The crater wear chart for the experiments is presented in Figure 67 and based on the confocal images in Figure 66. For the uncoated tools, adding MQL to the machining process generally reduced the crater wear, but the most reduction occurred with the MoS₂ addition. The crater depth was reduced by 30% from 61 μm in dry conditions to 43 μm. For the coated tools, MoS₂ also improved the crater with the best performance, with a 14% reduction of crater depth from 49 μm to 42 μm.

Coating +Lubrication	Crater Wear at Fracture	Coating +Lubrication	Crater Wear at Fracture
WC Dry		AlCrSiN Dry	
WC+Oil		AlCrSiN+Oil	
WC+WS ₂ (0.5%)		AlCrSiN+WS ₂ (0.5%)	
WC+hBN (0.5%)		AlCrSiN+hBN (0.5%)	
WC+MoS ₂ (0.5%)		AlCrSiN+MoS ₂ (0.5%)	
WC+xGnP (0.5%)		AlCrSiN+xGnP (0.5%)	

Figure 66. Confocal Images of crater wear during fracture

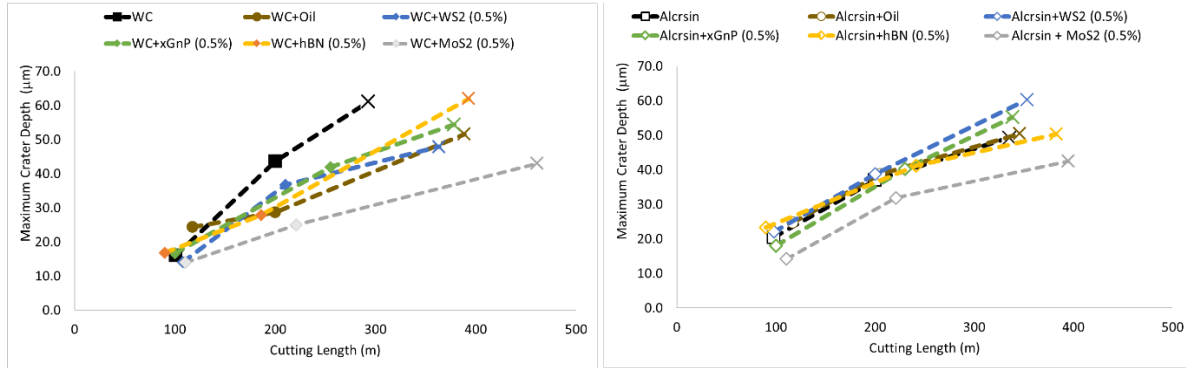


Figure 67. Crater wear chart for WC and AlCrSiN tools

MoS₂ has the lowest friction coefficient, is quite stable at high temperature, and have a high aspect ratio. The excellent performance of the MoS₂ additive was found in both uncoated and coated tools, with reduced flank and crater wear. Mo is a β stabilizer in Ti and a potent oxide former [125][126], which prevents carbide formation, such as TiC. The addition of MoS₂ in the MQL could theoretically prevent the adhesion layer from being formed (BUE and BUL), yielding a lower cutting force and a better machinability. However, adhesion layer was not measured and compared in this study.

In our previous results for flat carbide tools, graphite xGnP powders could reduce craters and increase tool life [56]. However, the chip breaker tools used did not show the same improvement. With the ‘hump’ tool profile, the tool-chip contact length become shorter than a flat tool, and temperature could be increased significantly. Since xGnP dissociates at a lower temperature than the other powders, it could cause poorer performance than the other powder that have high-temperature stability. Less improvement was observed when nano-sized hBN and WS₂ platelets were used. It is expected with the smaller additive size; there would be increased particle density and increased performance. Several studies [127], [128] found difficulties in maintaining constant particle flow during delivery for super fine particle size and it was recommended to use

larger particle sizes. From our mixing process, the hBN and WS₂ platelets easily dissociate after 72 hours; therefore, a couple of improvement strategies for the nano-sized additives would be to increase the particle size or increase the particle concentration in future studies.

5.4 Conclusions

This chapter present a preliminary study of using minimum quantity lubrication (MQL) with various additives for machining Ti64-STA at 122 m/min using uncoated and AlCrSiN coated carbide tools. Findings from this chapters includes:

- MoS₂ at 0.5 wt% mixed with rapeseed oil can aid the turning process of Ti64-STA, as evidenced by the reduction in cutting force, flank wear land and crater wear depth. In terms of tool life, the uncoated carbide improves by 58% and the coated tool improved by 17%
- AlCrSiN tools produced reduced flank wear land when MQL was applied for various additives compared to the dry condition. However, it eventually fractured.
- The chip breaker tools failed by attrition of the built-up edge and plastic deformation of the tool due to the increased rake angle.

CHAPTER 6: THE EFFECT OF CARBON FIBER TYPES ON TOOL WEAR DURING EDGE TRIMMING OF 0°, 45°, 90°, AND 135° CARBON FIBER REINFORCED PLASTIC LAMINATES

6.1. Experimental

6.1.1 Workpiece Materials

Three types of unidirectional carbon fibers with different material properties are used in this experiment. The first type is the T300 (Toray Composite Materials America, USA) standard modulus (SM) fiber, which is commonly used in aerospace applications with over 30-year production history. The second type chosen is IM-7 (Fiber Glast, TX, USA), an intermediate modulus (IM) fiber, which is also popular in aerospace applications. The last one is K13312 (Mitsubishi, USA) as a high modulus (HM) fiber. Both the SM and IM fibers are PAN-based carbon fibers, while the HM fiber is pitch-based. The CFRP laminates used in the experiments are fabricated at Protech Composites Inc. (Vancouver, WA, USA) using the vacuum infusion process, which is a typical CFRP fabrication process for large structures such as wind turbine blades and recreational yachts [129][130]. The vacuum infusion process uses a vacuum bag to compact laminate carbon plies laid onto the mold. The resin is then infused by the vacuum to completely wet out the reinforcements and eliminate all air voids in the laminate structure [129], [130]. The matrix is an epoxy resin system of DGEBA epoxy and DDS diamine curing agent (Aldrich Chemical Company, St. Louis, MO). All the coupon plate size is 250 mm by 200 mm. A total of six plates were fabricated for the edge-trimming experiments.

For each type of fibers, two cross-ply laminates were made with only two-ply angles, 0°/90° plies, and 45°/135° plies to reduce the processing-induced residual stress. The 0.3 mm thick

This chapter is published as : Khawarizmi, R., Bin Abdullah, M. S., Han, Y., Kim, D., and Kwon, P. "*The Effect of Carbon Fiber Types on Tool Wear During Edge Trimming of 0 deg, 45 deg, 90 deg, and 135 deg Carbon Fiber-Reinforced Plastic Laminates.*" ASME. *J. Manuf. Sci. Eng.* June 2022; 144(6): 061005.

cross-ply glass fibers were placed to the bottom and the top to cover the carbon fibers. The cross-ply glass fibers were added to separate two distinct carbon fiber orientations between 0° and 90° plies and between 45° and 135° plies in both CFRP workpieces during the fabrication. These cross-ply glass fibers also created distinguishable tool wear marks between two distinct carbon fiber orientations during the edge trimming experiments. The carbon fiber ply stack-ups for SM, IM, and HM fibers were resulted 14 plies, 13 plies, and 7 plies, respectively, for each orientation. For the tight weave IM and HM unidirectional carbon fibers, thin micromesh (thickness < 0.1 mm) was used within carbon fiber plies for an effective resin flow during the vacuum infusion process [131]. The resin flowrate was 1.5 inches/min.

A fabric type breather [132] was used within each plies in fabrication of IM and HM carbon fiber laminates as recommended by fabrication plant, which resulted in lower volume fraction than SM fiber laminates. The approximated fiber volume fraction of SM, IM, and HM carbon fiber laminates are 54%, 33%, and 40%, respectively. The volume fraction was calculated from optical image and SEM image of CFRP cross-sections using ImageJ software, as shown in Figure 68. The optical and SEM images show two type of zone, resin rich and breather zone, and matrix resin mixed zone. The resin rich areas and breather were identified using lower magnification optical and SEM images (50x and 100x). The corresponding areas of resin rich zone and breathers were calculated using ImageJ software. The volume fractions of carbon-resin mixed zone are obtained by subtracting volume fraction of resin rich zone from 100, which is 93%, 66% and 72% respectively for SM, IM and HM coupons. Then, carbon fiber volume fraction in the fiber-resin mixed zone were calculated using optical images at higher magnification (1,000x). The CF volume fractions are 58% for SM, 50% for IM and 56% for HM in resin-fiber mixed zone. Multiplication the above two sets of percentages provide the final carbon fiber volume fractions

for each laminate. Table 19 provides the specific properties of the respective carbon fibers and their CFRP workpieces [133]–[135]

Table 19. Properties of each carbon fiber type and its CFRP laminate used for the experiments

Fiber type	Standard modulus (SM)	Intermediate modulus(IM)	High modulus (HM)
Fiber manufacturer code	T300	IM7	K13312
Fiber tensile strength (MPa)	3530 [133]	5600 [134]	3200 [135]
Fiber tensile modulus (GPa)	230 [133]	276 [134]	420 [135]
Strain at fracture (mm/mm)	0.015 [133]	0.02 [134]	0.006 [135]
Fiber diameter(μm)	7 [133]	5 [134]	9 [135]
Total laminate thickness(mm)	11.6	6.6	8.38
Ply Thickness (mm)	0.254	0.1524	0.5048
Fiber volume fraction	54%	33%	40%
Layups for 0°/90° plies (GF = cross-ply glass fibers)	[GF ₂ /0° ₁₄ /GF/90° ₁₄ /GF ₂]	[0° ₁₃ /GF ₂ /90° ₁₃]	[0° ₇ /GF ₂ /90° ₇]
Layups for 45°/135° plies (GF = cross-ply glass fibers)	[GF ₂ /45° ₁₄ /GF/135° ₁₄ /GF ₂]	[45° ₁₃ /GF ₂ /135° ₁₃]	[45° ₇ /GF ₂ /135° ₇]

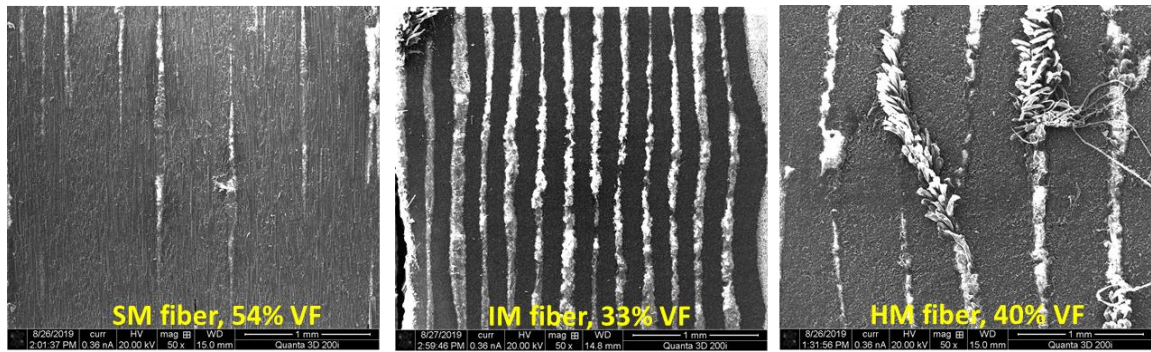


Figure 68. Cross section of CFRP workpieces at 0° ply angle at 50x magnification

6.1.2 Experimental Set-up

Uncoated 2-flute end mills made of micro-grain tungsten carbide (Atrax, MSC Industrial Co., IN, USA) was mounted in a 7.5 hp, 3-axis CNC mill (Minimill, HAAS®, CA, USA) to perform

the edge trimming experiments. The spiral flute direction is the right-hand direction. Table 20 summarizes the geometry dimensions of the end mill used in the experiment.

Table 20. End mill dimensions

Diameter(mm)	Length of cut (mm)	Shank diameter (mm)	Overall length (mm)	Helix angle
6.35	19.05	6.35	63.5	30°

The performed edge trimming was up-milling/conventional milling, in which the feed direction is opposite to the cutting direction. A spindle speed of 6000 RPM (cutting speed 120 m/min) was used for edge trimming. Other parameters such as feed per revolution and depth of cut were kept constant at 0.0508mm/rev (0.002 in/rev) and 0.508 mm (0.02 in), respectively. Additionally, a water-soluble coolant (Kool Mist®, CA, USA) typically used in aircraft parts manufacturing environment was used to reduce the cutting temperature and heat build-up. Figure 69 presents the experimental set-up and the fiber ply angle schematic. To investigate the wear progression, tool traveling lengths are set at four increments: 1m, 4m, 8m, and 16 m. These data points will capture the initial and steady-state regimes of tool wear [66]. Tool wear measurement will be explained in the next section.

Additionally, the arithmetic mean roughness (Ra) values of the machined CFRP surface were measured using a surface profilometer (SJ-210, Mitutoyo®, Japan). A cut-off length of 0.8 mm and a traverse length of 4.0 mm were chosen at 5 different positions on the machined CFRP workpiece in longitudinal cutting direction.

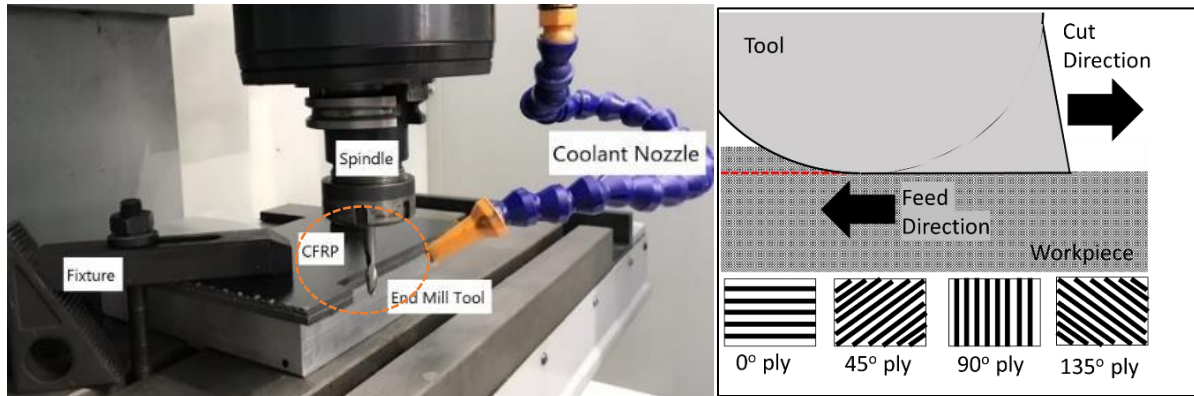


Figure 69. Edge trimming setup and fiber ply orientation

6.1.3 Tool wear evaluation methods

After machining, worn-out tools were cleaned by applying compressed air and acetone bath in an ultrasonic cleaner (Model 5300, Ultrasonic Power Corp[®], IL, USA) for 30 minutes. For quantitative wear measurements, end mill tools were imaged using the VHX-6000 digital light microscope (Keyence[®], IL, USA). The 3-dimensional (3-D) image of the cutting edge was constructed by a series of images captured at 200X magnification with a stepsize of 1.14 μm in the height direction. Then, a single 2-D cross-sectional profile from the middle was extracted to measure the tool wear. Figure 70 (A) shows the captured 3-D image of the tool cutting edge and the selected 2-D cross-section.

Edge rounding has been reported as the dominant wear mode in CFRP machining[60]–[62][136]–[138]. It occurs due to the abrasion of machined carbon fibers on both the flank and the rakeface. The edge rounding was measured by comparing the radius of the cutting edge before and after each trimming pass. The edge shape is approximated as a circle using the best fit circle equation and optimized by GRG (Generalized Reduced Gradient) non-linear algorithm [139]. On the other hand, one of the most common criteria in wear analysis is to measure the length of the flank wear land before and after machining, or simply known as flank wear (V_B). Flank wear land measurements

are widely used in metal machining but are also applied to measure tool wear in machining CFRP. Additionally, the worn area is calculated by subtracting the area between the fresh and worn tool profiles, by the method of trapezoidal area under the curve. Figure 68(B) shows the three wear criteria measured in this experiment.

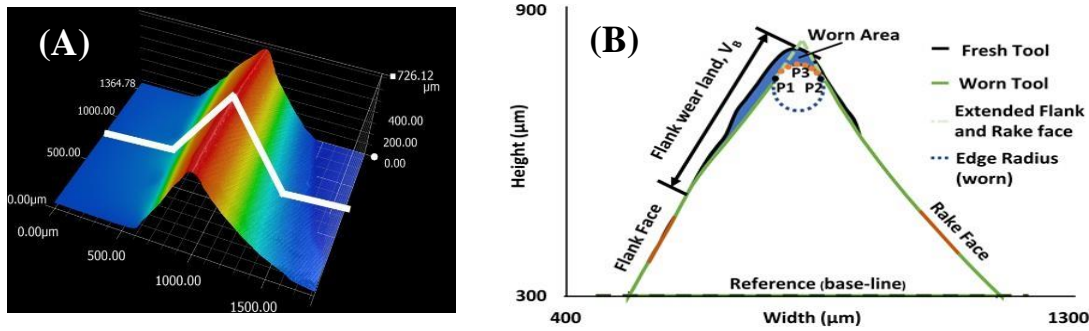


Figure 70. (A) 3-D profile of tool cutting edge and extracted 2-D profile. (B) Three tool wear measurement methods on a 2-D tool edge profile: the flank wear land, the edge radius (the dotted circle), and the worn area (the shaded area).

To evaluate tool wear qualitatively, the worn tools were observed using a scanning electron microscope (SEM) from Quanta 3D 200i-ThermoFisher® at 30keV. To analyze the tool wear mechanism in detail, two distinct locations of each worn tool were observed when using SEM at higher magnifications. Figure 71 shows an SEM image of a worn tool at 1000x and two locations: edge rounding zone and flank wear zone that were further analyzed at 20,000x magnification.

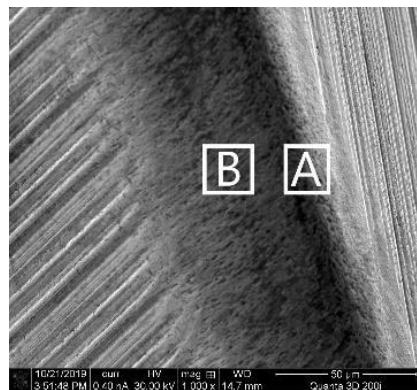


Figure 71. Two locations of SEM investigations in a worn tool surface (A: edge rounding zone; B: the flank wear zone)

6.2 Results and Discussions

6.2.1 Tool wear measurements by digital light microscope

The tool wear for CFRP machining mainly stems from the abrasiveness of carbon fibers [60]. Due to the various fiber volume fractions among CFRP workpiece laminates, all wear measurements were normalized to each respective fiber volume fraction reported in Table 19. These normalized wear measurements are common as the resulting wear is proportional to the amount (volume fraction) of abrasive (fibers) present [140], [141] at least within the small range of volume fractions in our CFRP samples. The normalized edge radii, normalized flank wear, and normalized worn area results for each ply angle and each fiber type are presented in Figures 72, 73, and 74.

For the edge rounding data shown in Figure 72, the wear progression yields the largest edge radii for the ply angle of 90° with the CFRP laminate made of IM fibers. Among the CFRP laminates with various ply angles, the largest edge rounding was observed with the 90° plies, which agrees well with our previous results [66]. When comparing the edge rounding among three fiber types with various ply angles, the trend is consistent where the IM fibers yield the largest radii, followed by the HM fibers, and the SM fibers yield the least edge rounding. Note that IM fibers have the highest strength while the HM fibers have the largest elastic modulus. For the flank wear measurements (see Figure 73), the 45° plies have the most extensive normalized flank wear compared to the other ply angles. Our previous research [66] reported that the interaction between broken protruded fibers and the flank surface was dominant in causing extensive flank wear with the 45° plies. In addition, the number of exposed broken carbon fibers is the largest in the 45° plies compared to the other ply angles.

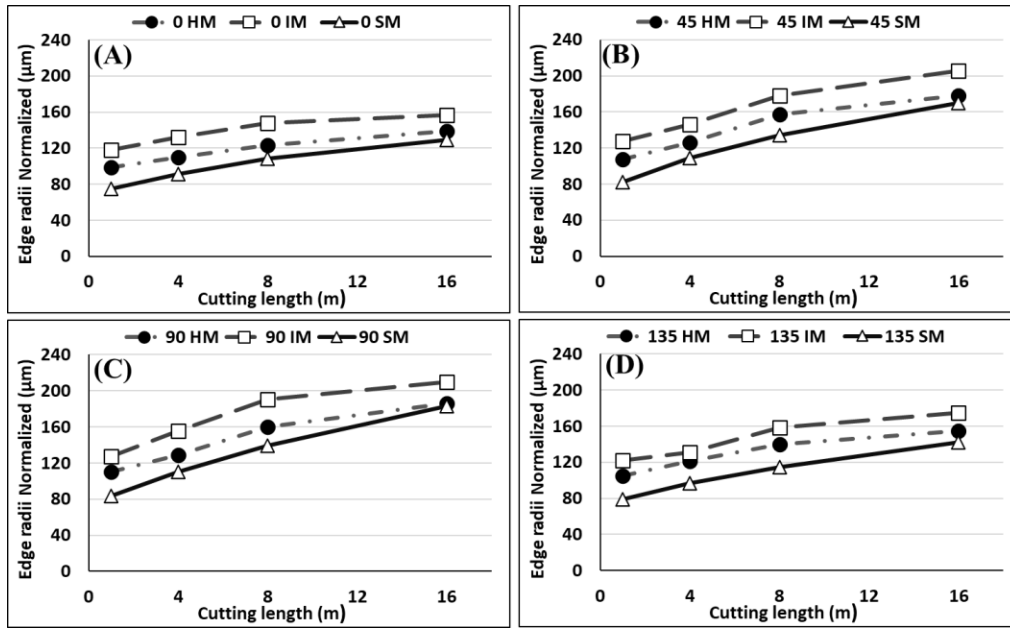


Figure 72. Normalized edge radii for different plies (A) 0° (B) 45°(C) 90°(D) 135°

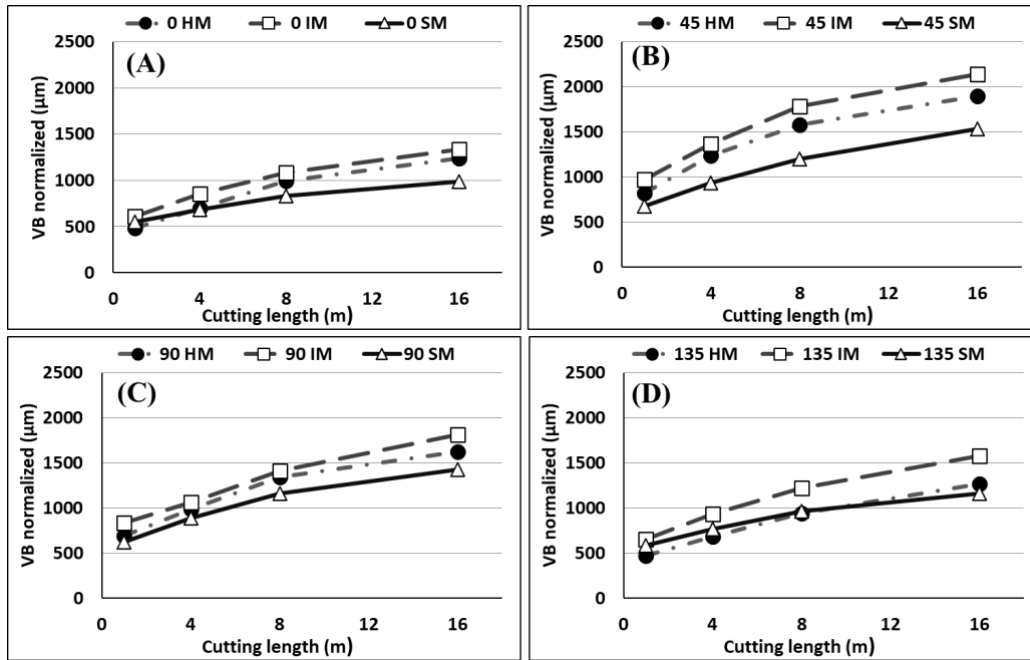


Figure 73. Normalized flank wear for different plies (A) 0° (B) 45° (C) 90° (D) 135°

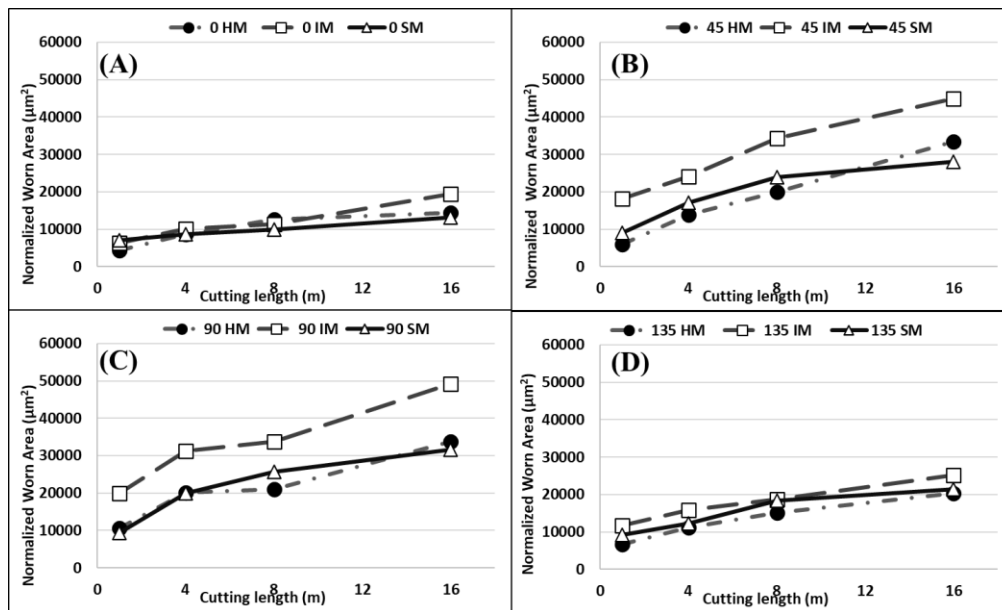


Figure 74. Normalized worn area for different plies (A) 0° (B) 45° (C) 90° (D) 135°

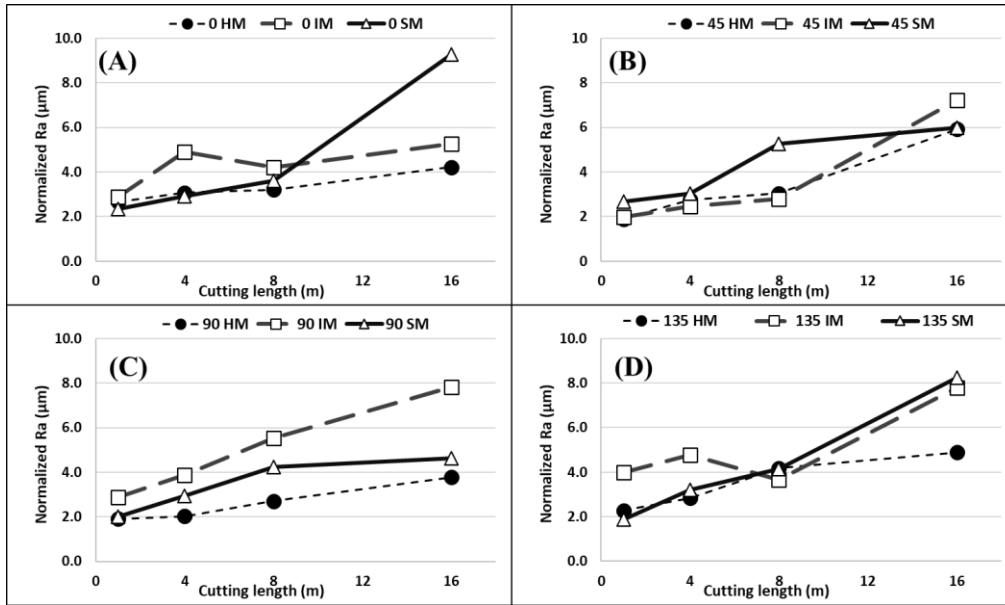


Figure 75. Normalized surface roughness (Ra) for different plies (A) 0° (B) 45° (C) 90° (D) 135°

With different fiber properties, the IM fibers have more flank wear compared to the HM and SM fibers. The normalized worn area measurements in Figure 74 represent the combination of the flank wear and the edge rounding wear. Between different fiber plies, it is shown that 0 and 135 ply angle yield the least worn area in the tool. When comparing the fiber properties, the IM fibers result in a slightly larger worn area. For the 45° and 90° plies, the impact of IM fibers is significantly higher, with 90° plies produced the largest worn area in comparison to the other ply angle, which indicates edge rounding was more dominant than the flank wear in the worn area measurements. The most profound edge rounding with the 90° plies is related to the largest cutting force during machining of CFRP [142]. Figure 75 presents the surface roughness (Ra) of the CFRP workpieces measured by contact profilometer, due to the resin and the breather (micromesh) [143] in the IM and HM fibers, the roughness measured was also normalized with respect to the fiber volume fraction.

6.2.2 Tool wear and machined CFRP surface investigations by SEM & Roughness

The abrasion of the tungsten carbide (WC) tool in machining CFRP is known to occur in two distinct modes: soft abrasion and hard abrasion [24]. The soft abrasion occurs by the removal of the soft cobalt binder in the tool by the broken fibers, which then fractures along the WC grain boundaries. As the cracks reach deeper following the inter-granular path, the carbide grains are loosened. The carbide grains are eventually dislodged by the subsequent interactions with fibers [144]. Pits and depressions on the tool surface are formed due to the dislodgements of carbide grains. The worn surface is characterized by a 'rough' surface because of the presence of pits and cavities when soft abrasion is dominant (Figure 76).

In contrast, hard abrasion is the direct abrasion on the tool surface by the broken fibers or indirect abrasion by the fiber and/or carbide debris. These debris were formed due to the brittle fracture of carbon fibers and the micro-spalling on the carbides. The hard abrasion on the tool eventually creates scoring marks on the worn surface with or without tiny pits [144]. Figure 77 represents the SEM images of the worn tools and Figure 78 represents the machined CFRP surfaces at 16 m cutting length for each plies. Figure 77 shows the presence of hard abrasion on the tool surfaces. Regardless of fiber types and orientation, the worn tool surface is relatively smooth and flat, with occasional scoring marks. This is a typical surface topography caused by hard abrasion that carbon fibers abrade carbide grains. More pronounced scoring marks are present on the flank wear lands for the IM and HM fibers when compared with the edge rounding zones. They indicate the hard abrasion by the IM and HM fibers in the tool flank surface. There are little to no scoring marks in the flank lands as the abrasive actions are less intense with the SM fibers with lower modulus and strength.

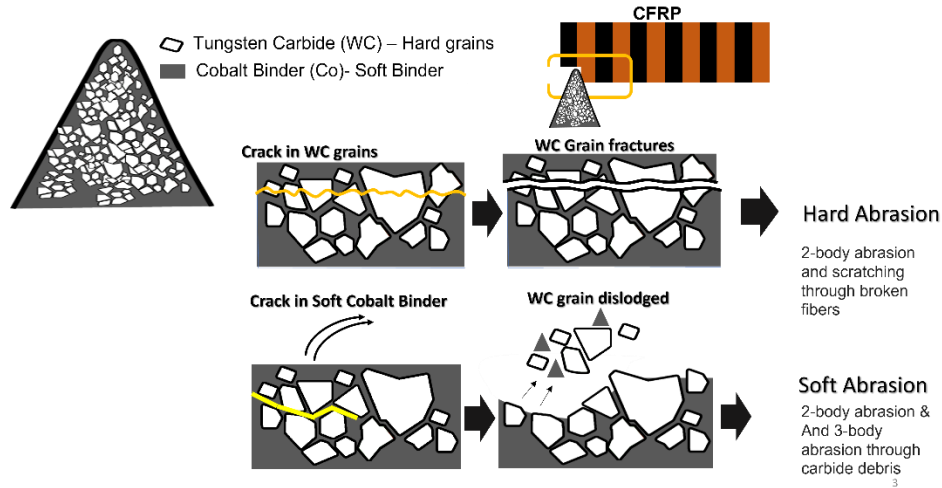


Figure 76. Hard and Soft Abrasion in WC tool from CFRP, adapted from [144]

Unlike the flank lands, the worn tool surface on the edge rounding zones, as shown in the first and third columns of figures in Figure 77, contains rough regions due to the removals of sub-micron carbide grains. They indicate soft abrasion that carbide grains were pulled off after the removal of the soft cobalt phase. As shown in the SEM images from the 90° plies, the IM and HM fibers, specifically, yielded a much higher number of dislodged WC grains than the SM fibers. It is noted that both the SM fibers have slightly higher tensile strength and significantly lower tensile modulus than the HM fibers (See Table 19). Figure 72 shows that the HM fibers result in higher normalized edge radii than the SM fibers. More extensive edge rounding wear by the HM fibers, when compared with the SM fibers, can be caused by the combination of soft abrasion and hard abrasion by the HM fibers.

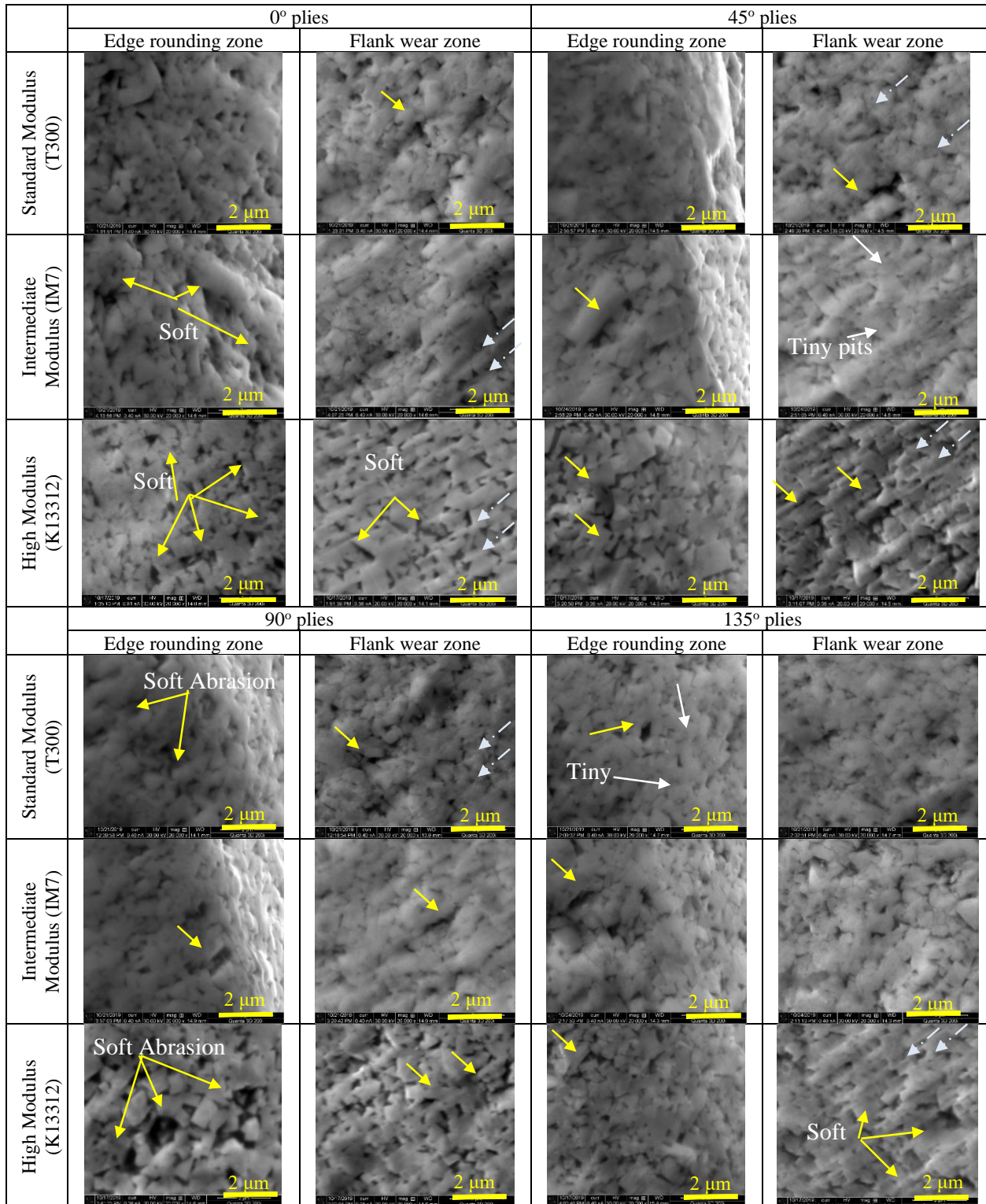


Figure 77. SEM images of the cutting edges for three fiber types at four different fiber orientations (20,000 \times ; yellow arrow refers to soft abrasion (dislodged carbide grains))

Figure 78 also shows the morphology of all broken fibers in CFRP surface. Compared to the other fiber types, the SM fibers produced cleanly broken ends similar to the IM fibers in the 0° and 45° plies. The clean fracture surface also indicates a flexural fracture, with the fibers snapped in half in the cross-section, which reported by Xie *et.al* [143]. This flexural fracture is directly related to the edge-trimming operation performed and yields an uneven CFRP surface. With the SM and IM fibers being PAN-based, the SM fibers with relatively lower tensile strength yield less wear than the IM fibers.

On the contrary, the HM fibers fracture much easier at the failure strain of 0.06 mm/mm. Thus, HM fibers interact with the tool for a lesser time or require lower cutting energy to fracture than the IM and SM fibers. However, the broken HM fibers still effectively abrade the tool surface, as seen in Figure 77. The HM fibers are pitch-based; therefore, they have sheet-like microstructures from the graphitization during the production process [77], [78]. The unique fiber structures of the HM fibers resulted in an increased stiffness but more brittle to fracture. The cross-section of pitch-based carbon fiber consists of crystalline graphite sheets that are often comparable to disorganized rolls [76]. Figure 78 shows the broken HM fibers into micro-fibrils and tiny sheets. The broken HM micro-fibrils, which are clearly shown in 5,000X images, can remove cobalt binders more effectively, causing soft abrasion. Furthermore, the high stiffness of HM fibers can make the broken fibers bounce back, which becomes more effective abrasion on the tool surface.

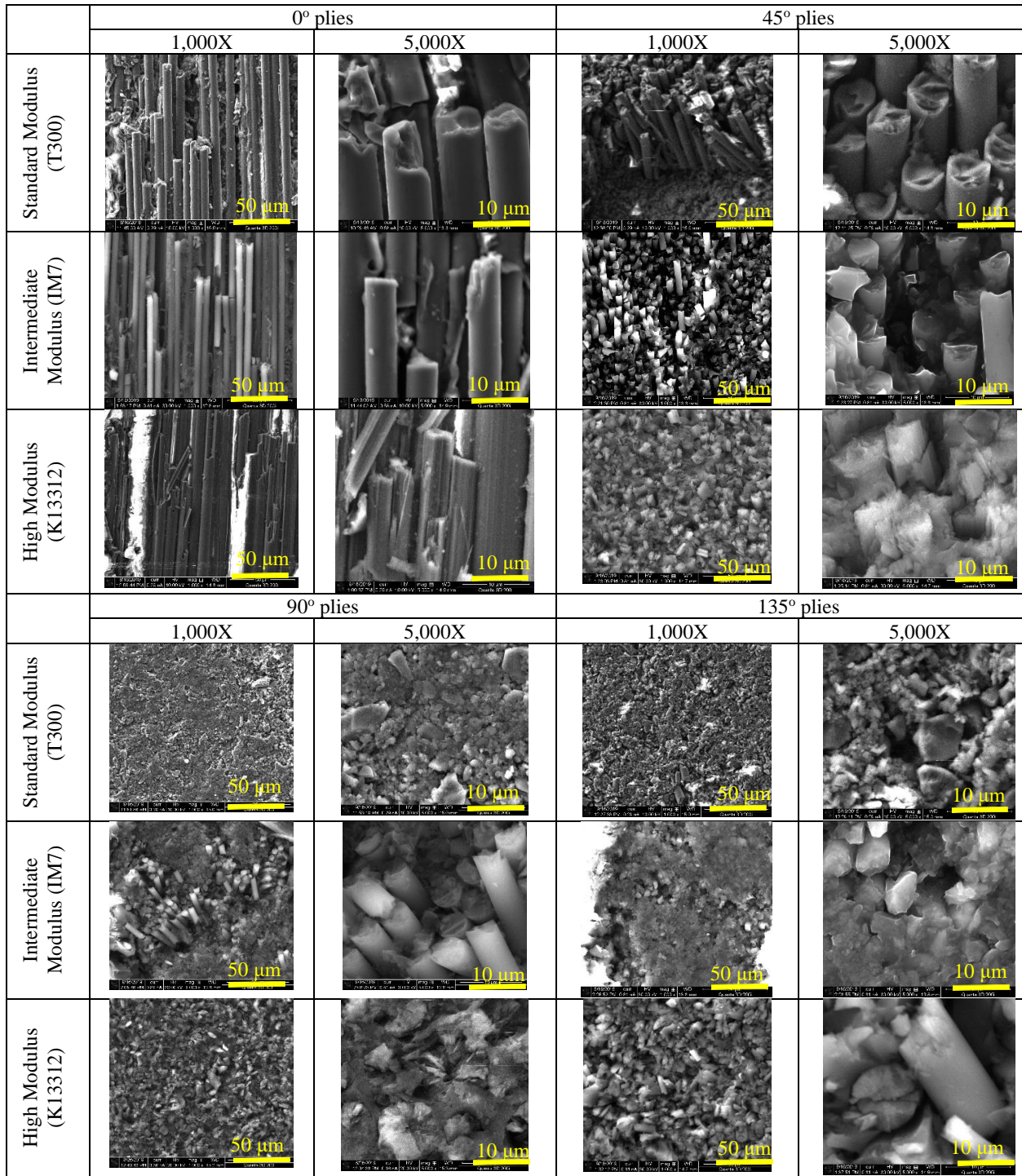


Figure 78. SEM images of the machined CFRP surface after cutting 16 m for three fiber types at four different orientations (1000×and 5000×)

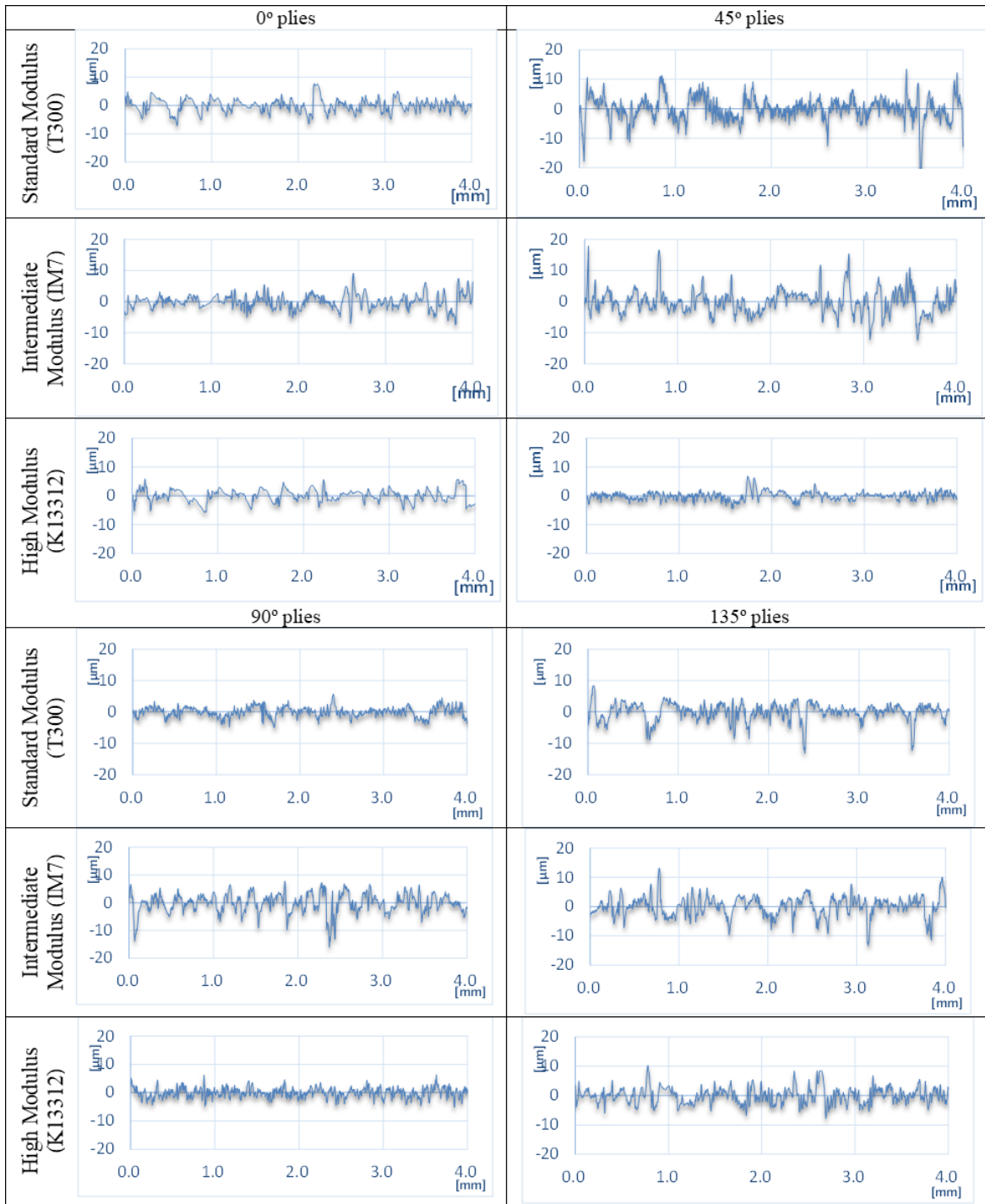


Figure 79. Raw surface roughness measurements at 16 m cutting distance

The effect of fiber types and the edge trimming operation can also be seen in the surface roughness measurement, as raw data is provided in Figure 79. The peaks and valleys in the roughness signals indicate sharp surfaces and cavities in the CFRP surface. This raw signal measurement is then averaged and normalized with respect to the fiber volume fraction and the result was presented in Figure 75 earlier. There was strong roughness of 0° plies for SM fibers at 16m compared to other fibers. However, when the SEM image was observed in Figure 76. The fibers showed bending and incomplete fracture. At 45° plies there is a sharp feature from the broken fibers observed by the profilometer in Figure 79. On the other hand, at 90° plies SM and HM fibers shows a relatively flat surface at 16 m while IM fibers shows a sharp surface. The flat surface were related to the increase in polymer/matrix smearing at the 90° and 135° plies. The matrix smearing surface is shown in Figure 78. Additionally at 135° plies, there is a significant cavity in the surface, that is indicative of a fiber pullout.

Among the three fiber types, IM fiber produced the most extensive normalized tool wear in all three measurements from Figures 72 to 74. The IM fibers have the highest tensile strength, strain at fracture, and toughness than the other fiber types, which caused the IM fibers to require the most considerable energy during chip formation. Also, the diameter of the IM fibers is the smallest among all three fiber types, resulting in more fibers interacting with tool surfaces. The largest tool wear from the strongest carbon fibers, IM fibers in this study, agree well with the study done by Hodzic *et al.* [70]. They reported that the high abrasiveness of carbon fiber possibly comes from higher fiber strength. Moreover matrix smearing was the prominent feature specifically in both 90° and 135° plies machining resulting from its the chip formation mechanisms [66,128] (broken fibers interacting with the tool for 90° and burst type of chip for 135° plies). The matrix smearing would diminish abrasion by covering the broken fibers, as the broken fibers generated in these plies for the SM fibers are less pronounced in comparison with other fiber types, which are less

dense and larger in diameter. Therefore, the SM fibers yield less wear than the other two different fiber types due to the low strength/modulus to limit hard abrasion and the matrix smearing on the machined workpiece to diminish the fiber-tool interaction.

6.3. Conclusions

This chapter presented a study on the effects of fiber properties on tool wear edge trimming of CFRP laminates with three different carbon fibers and four distinct fiber ply orientations. CFRPs fabricated with the standard modulus (SM), intermediate modulus (IM), and high modulus (HM) carbon fibers were edge-trimmed at the constant cutting speed and feed. The worn surfaces of the tool and the machined CFRP surfaces were also analyzed. Additionally surface roughness were also analyzed. Three wear criteria, namely: flank wear, edge rounding radii, and worn area are measured proportional to the workpiece fiber volume fraction and compared. The major conclusions that can be derived are:

1. Tool wear, flank wear, edge radii, and worn area on the uncoated carbide tools during the edge trimming process are influenced by the distinct CFRP fiber properties, namely the fiber tensile strength, tensile modulus, and fiber microstructure (PAN-based or pitch-based).
2. The IM carbon fibers resulted in the highest wear compared to the HM and SM carbon fibers. The high tensile strength of the IM carbon fibers caused the largest tool wear from the combination of hard abrasion while breaking carbon fibers and additional abrasion from the broken fiber ends.
3. Pitch-based HM fibers yield the second-largest tool wear, despite their lower tensile strength. The graphitized microstructure produces broken sheet-like fibers that were effectively removed carbide grains by means of soft abrasion in addition to hard abrasion. Furthermore, the higher stiffness of the HM fibers makes the wear rate increase compared to the SM fibers.

4. The SM fibers resulted in the lowest tool wear compared to the other fiber types due to their lower tensile strength and less sharply broken fibers. The matrix smearing on the machined SM fiber workpiece also indicates reduced fiber-tool interactions to cause less tool wear.

5. When it comes to the effect of fiber orientation on tool wear, the 45° plies yield the most extensive flank wear, regardless of the fiber types. This is due to the largest number of carbon fibers interacting with the tool in the 45° plies compared to the other ply angles. The largest edge rounding radii are found in the 90° plies due to the most significant cutting force and surface roughness from 90° fiber orientation.

\

APPENDICES

APPENDIX A – Histogram of the Segmentation Distance in Ti64

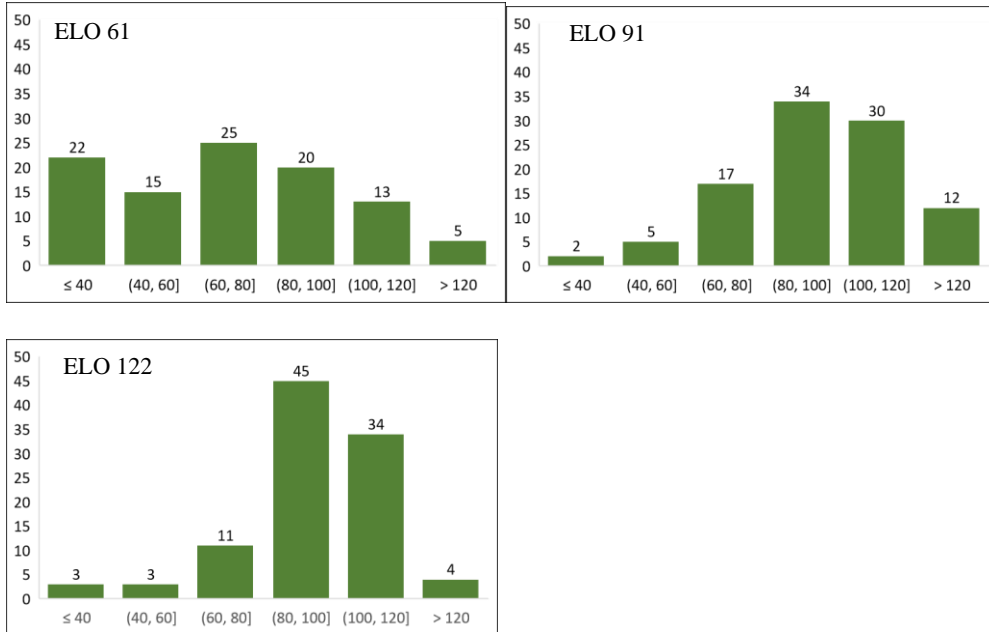


Figure 80. Histogram for measured segmentation distance in ELO chips

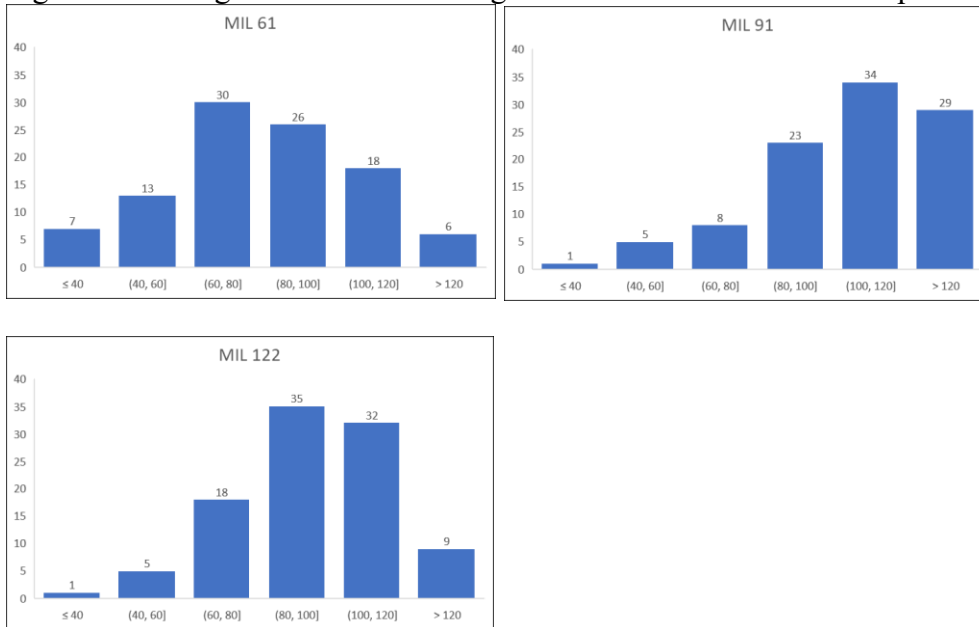


Figure 81. Histogram for measured segmentation distance in MIL chips

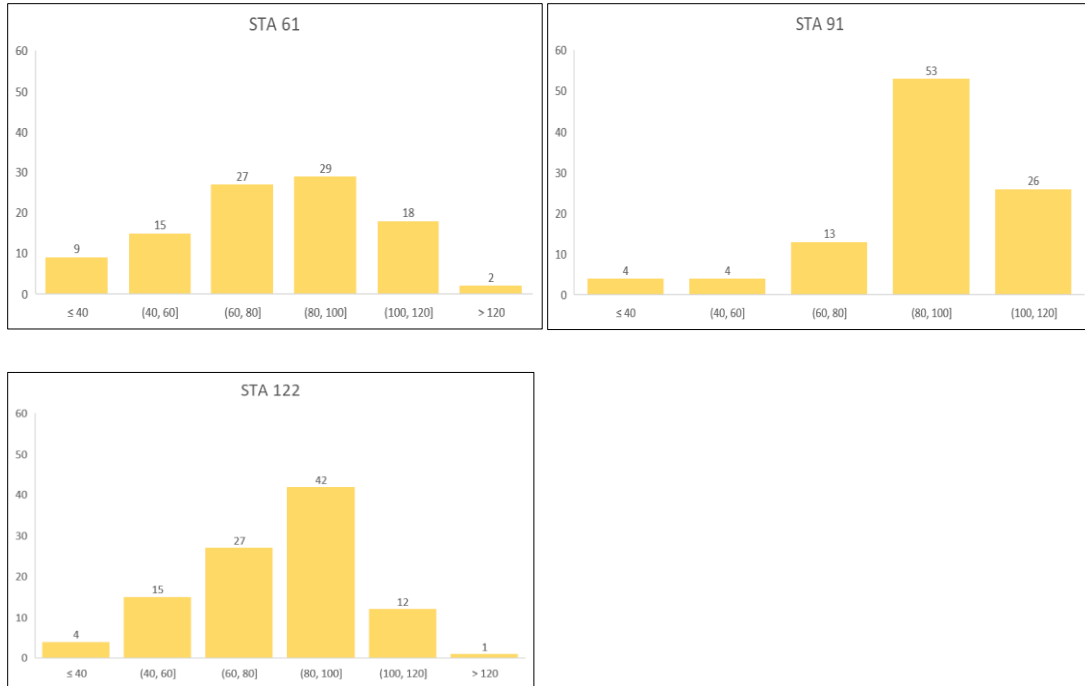


Figure 82. Histogram for measured segmentation distance in STA chips

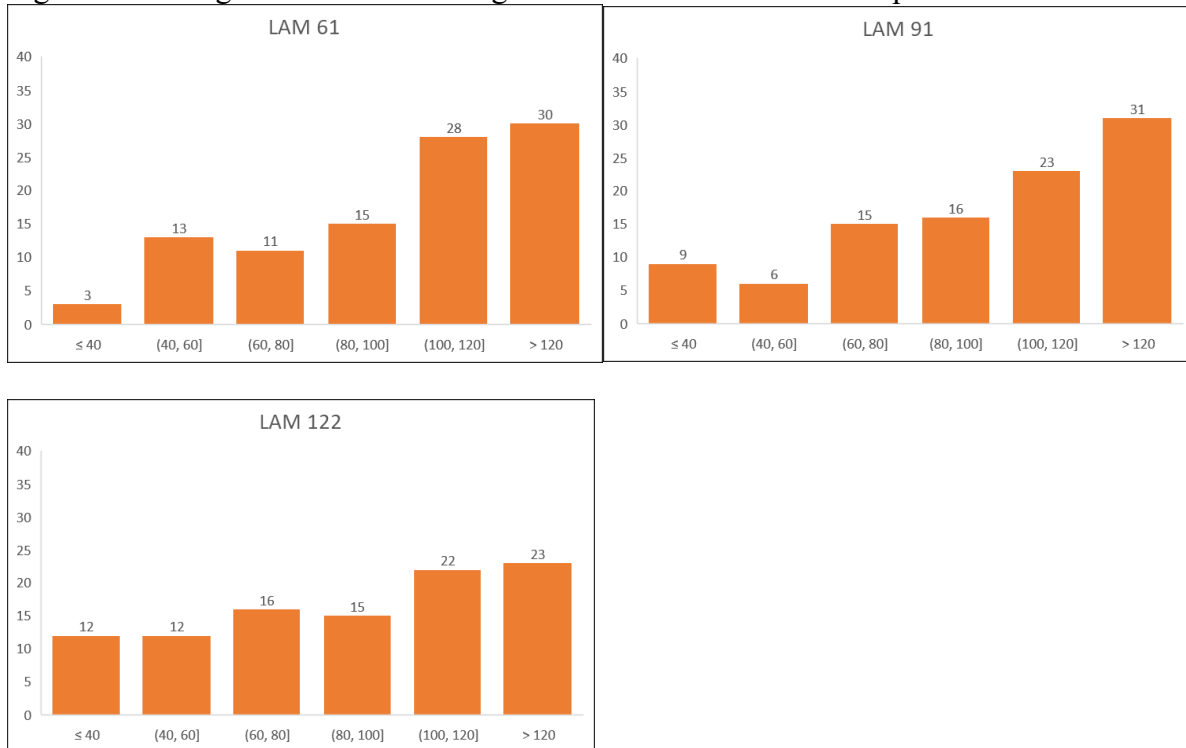


Figure 83. Histogram for measured segmentation distance in LAM chips

APPENDIX B – Cooling Rate in Turning Ti64-ELO

The convective heat transfer coefficient for air flow can be approximated to :

- $h_c = 10.45 \cdot v + 10 \cdot v^{1/2}$
- $v = 122 \text{ m/min} = 2.033 \text{ m/s}$

Then,

- $h_c = 22.67 \text{ kCal/m}^2 \cdot ^\circ\text{C} = 26.3 \text{ W/m}^2 \cdot ^\circ\text{C}$

Calculating the *Biot* number for the system, approximating the chip as an infinite strip:

- Characteristic length of the system (L_c) = $w/2$ (w - height of the chip)
 - $L_c = \sim 78 \mu\text{m}$
- $Bi = \frac{hL_c}{k} = \frac{26.3 \cdot 78 \times 10^{-6}}{6.7} = 3 \times 10^{-4}$
- Since $Bi \ll 0.1$, The system can be approximated as a lumped system analysis

Calculating the cooling exponent (b) for Ti alloy:

$$b = \frac{h}{\rho C_p L_c} = \frac{26.3}{4430 \times 526.3 \times 78 \times 10^{-6}} = 0.144$$

Substituting b to the equation:

$$\frac{T(t) - T_\infty}{T_i - T_\infty} = e^{-bt}$$

For $T_i = 1000^\circ\text{C}$ and $T_\infty = 20^\circ\text{C}$:

$$T(t) = 20 + 980 e^{-0.144t}$$

$$T(60\text{s}) = 20.17$$

$$\text{Cooling Rate} = \frac{1000 - 20.17}{60} = 16.3^\circ\text{C/s}$$

APPENDIX C – Matlab Code For Tensor Calculation [93]

```
clear,clc,close all
format short g
S = dlmread ('Step174_5x10_all_2.txt',' ',1,0); %Row i, Column 0

global rows columns;
[rows,columns]= size (S)
for col = 1:columns;
    for row = 1:rows;
        end;
end;
k=1;
omega=1;
for i=1:k:rows;
    sigmaT= [S(i,6) S(i,9) S(i,10);
            S(i,9) S(i,7) S(i,11);
            S(i,10) S(i,11) S(i,8)];
    [V,D] = eig(sigmaT);
    [V,D,W] = eig(sigmaT);

    W1 = [W(1,3);W(2,3);W(3,3)];
    W2 = [W(1,2);W(2,2);W(3,2)];
    W3 = [W(1,1);W(2,1);W(3,1)];

    Rad=[W(1,3) W(1,2) W(1,1);
        W(2,3) W(2,2) W(2,1);
        W(3,3) W(3,2) W(3,1)];

    PS = [D(3,3);D(2,2);D(1,1)];

    l1 = W(1,3);
    m1 = W(2,3);
    n1 = W(3,3);

    l2 = W(1,2);
    m2 = W(2,2);
    n2 = W(3,2);

    l3 = W(1,1);
    m3 = W(2,1);
    n3 = W(3,1);

    Cosine = [W(1,3) W(1,2) W(1,1);
             W(2,3) W(2,2) W(2,1);
             W(3,3) W(3,2) W(3,1)];

    Degree_Angle=[acos(l1)*180/pi acos(l2)*180/pi acos(l3)*180/pi ;
                 acos(m1)*180/pi acos(m2)*180/pi acos(m3)*180/pi ;
                 acos(n1)*180/pi acos(n2)*180/pi acos(n3)*180/pi] ;

    Probe1=l1^2+m1^2+n1^2;
    Probe2=l2^2+m2^2+n2^2;
    Probe3=l3^2+m3^2+n3^2;

    Vector_1 = [l1 m1 n1];
```

```

Vector_2 = [l2 m2 n2];
Vector_3 = [l3 m3 n3];

Vector_Matrix(i,:) = [l1 m1 n1 l2 m2 n2 l3 m3 n3];

E(i,:)=round ([i S(i,3) S(i,4) S(i,5) D(3,3) W1(1,1) W1(2,1) W1(3,1)
D(2,2) W2(1,1) W2(2,1) W2(3,1) D(1,1) W3(1,1) W3(2,1) W3(3,1)],4);
MV (i,:) = [W1(1,1) W1(2,1) W1(3,1) W2(1,1) W2(2,1) W2(3,1) W3(1,1)
W3(2,1) W3(3,1) ];
M(i,:) = [i S(i,3) S(i,4) S(i,5) D(3,3) Degree_Angle(1,1)
Degree_Angle(2,1) Degree_Angle(3,1) D(2,2) Degree_Angle(1,2)
Degree_Angle(2,2) Degree_Angle(3,2) D(1,1) Degree_Angle(1,3)
Degree_Angle(2,3) Degree_Angle(3,3)]
Probe_M(i,:) = [i Probe1 Probe2 Probe3];

% s^3-In1*s^2+In2*s-In3=0
I1= D(3,3)+D(2,2)+D(1,1);
I2= D(3,3)*D(2,2)+D(2,2)*D(1,1)+D(3,3)*D(1,1);
I3= D(3,3)*D(2,2)*D(1,1);
InvMatrix = [I1 I2 I3]
I(i,:) = [i InvMatrix(1,1) InvMatrix(1,2) InvMatrix(1,3)];
roots([1 -InvMatrix(1,1) InvMatrix(1,2) -InvMatrix(1,3)]);
MaxShearStressTs1 = (D(2,2)-D(1,1))/2;
MaxShearStressTs2 = (D(3,3)-D(1,1))/2;
MaxShearStressTs3 = (D(3,3)-D(2,2))/2;

MaxShearMatrix=[MaxShearStressTs1 MaxShearStressTs2 MaxShearStressTs3];
MSM(i,:)= [i S(i,3) S(i,4) S(i,5) MaxShearMatrix(1,1)
MaxShearMatrix(1,2) MaxShearMatrix(1,3)];
end

rowNames = arrayfun(@num2str,1:rows,'uni',0);
colNames = {'i',
'x','y','z','Sigma1','alpha1','beta1','gamma1','Sigma2','alpha2','beta2','gam
ma2','Sigma3','alpha3','beta3','gamma3'};
DataTable_COS = array2table(E, 'VariableNames',colNames)

writetable(DataTable_COS,'DataTablePrincipalStress_COS.txt','Delimiter',' ')
writetable(DataTable_COS,'DataTablePrincipalStress_COS.dat','WriteRowNames',t
rue)

filename = 'DataTablePrincipalStress_COS.xlsx';
writetable (DataTable_COS,filename,'Sheet',1,'Range','D1');

rowNames = arrayfun(@num2str,1:rows,'uni',0);
colNames = {'i',
'x','y','z','Sigma1','alpha1','beta1','gamma1','Sigma2','alpha2','beta2','gam
ma2','Sigma3','alpha3','beta3','gamma3'};
DataTable_DEGR = array2table(M, 'VariableNames',colNames)

writetable(DataTable_DEGR,'DataTablePrincipalStress_DEGR.txt','Delimiter','
')
writetable(DataTable_DEGR,'DataTablePrincipalStress_DEGR.dat','WriteRowNames'
,true)

rowNames = arrayfun(@num2str,1:rows,'uni',0);
colNames = {'l1', 'm1', 'n1', 'l2', 'm2', 'n2', 'l3', 'm3', 'n3'};

```

```

DataTable_COS = array2table(Vector_Matrix, 'VariableNames', colNames)
writetable(DataTable_COS, 'DataTablePrincipalStressDirections.txt', 'Delimiter'
, ' ');

```

```

figure ('Units', 'centimeters', ...
'Position', [0 0 30 18], ...
'PaperPositionMode', 'auto');
gcf
hold on
run('Vektorfield_1')

```

Vektorfield_1

```

format short g
M = dlmread('DataTablePrincipalStress_COS.txt', '', 1, 0) % Row 1, Column 0

global rows columns;
[rows, columns] = size (S);
for col = 1:columns;
    for row = 1 : rows;
        end;
end;
omega=0.003;
for i=1:k:rows;
    M;
    X=[M(i,2)];
    Y=[M(i,3)];
    Z=[M(i,4)];
    V(i,:)= [X;Y;Z];

    sigma1 = M(i,5);
    alpha1 = M(i,6);
    beta1 = M(i,7);
    gamma1 = M(i,8);
    P1X0 = M(i,2);
    P1Y0 = M(i,3);
    P1Z0 = M(i,4);
    P1X = X+sigma1*alpha1*omega;
    P1Y = Y+sigma1*beta1*omega;
    P1Z = Z+sigma1*gamma1*omega;

    InvP1X= X-sigma1*alpha1*omega;
    InvP1Y= Y-sigma1*beta1*omega;
    InvP1Z= Z-sigma1*gamma1*omega;

    sigma2 = M(i,9);
    alpha2 = M(i,10);
    beta2 = M(i,11);
    gamma2 = M(i,12);

    P2X = X+sigma2*alpha2*omega;
    P2Y = Y+sigma2*beta2*omega;
    P2Z = Z+sigma2*gamma2*omega;

    InvP2X= X-sigma2*alpha2*omega;
    InvP2Y= Y-sigma2*beta2*omega;
    InvP2Z= Z-sigma2*gamma2*omega;

```

```

sigma3 = M(i,13);
alpha3 = M(i,14);
beta3 = M(i,15);
gamma3 = M(i,16);

P3X = X+sigma3*alpha3*omega;
P3Y = Y+sigma3*beta3*omega;
P3Z = Z+sigma3*gamma3*omega;

InvP3X= X-sigma3*alpha3*omega;
InvP3Y= Y-sigma3*beta3*omega;
InvP3Z= Z-sigma3*gamma3*omega;

PStart_P1 = [M(i,2) M(i,3) M(i,4)];
PEnd_P1=[P1X P1Y P1Z];
Inv_PEnd_P1 = [InvP1X InvP1Y InvP1Z];

PStart_P2 = [M(i,2) M(i,3) M(i,4)];
PEnd_P2=[P2X P2Y P2Z];
Inv_PEnd_P2 = [InvP2X InvP2Y InvP2Z];

PStart_P3 = [M(i,2) M(i,3) M(i,4)];
PEnd_P3=[P3X P3Y P3Z];
Inv_PEnd_P3 = [InvP3X InvP3Y InvP3Z];

plot3(X,Y,Z, '.k', 'MarkerSize', 40);
hold on
plot3(P1X,P1Y,P1Z, '.r', 'MarkerSize', 1);
str={'\sigma{1}'};
text(P1X,P1Y,P1Z, str, 'FontSize', 16);
hold on
% plot3(P2X,P2Y,P2Z, '.r', 'MarkerSize', 1);
% str={'\sigma{2}'};
% text(P2X,P2Y,P2Z, str, 'FontSize', 16);
% hold on
plot3(P3X,P3Y,P3Z, '.r', 'MarkerSize', 1);
str={'\sigma{2}'};
text(P3X,P3Y,P3Z, str, 'FontSize', 16);
hold on

if M(i,5)<0; %Sigma 1
    mycolor = 'b';
else;
    mycolor = 'r';
end;
plot3([PStart_P1(1) PEnd_P1(1)], [PStart_P1(2) PEnd_P1(2)], [PStart_P1(3)
PEnd_P1(3)], mycolor, 'Linewidth', 2);
hold on

% if M(i,9)<0; %Sigma 2
%     mycolor = 'b';
% else;
%     mycolor = 'r';
% end;
% plot3([PStart_P2(1) PEnd_P2(1)], [PStart_P2(2) PEnd_P2(2)], [PStart_P2(3)
PEnd_P2(3)], mycolor, 'Linewidth', 2);
% hold on

if M(i,13)<0; %Sigma 3
    mycolor = 'b';
else;
    mycolor = 'r';
end;

```

```

end;
plot3([PStart_P3(1) PEnd_P3(1)], [PStart_P3(2) PEnd_P3(2)], [PStart_P3(3)
PEnd_P3(3)], mycolor, 'Linewidth',2);
hold on

if M(i,5)<0; %Sigma 1
    mycolor = 'b';
else;
    mycolor = 'r';
end;
plot3([PStart_P1(1) Inv_PEnd_P1(1)], [PStart_P1(2) Inv_PEnd_P1(2)], [PStart_P1(3)
Inv_PEnd_P1(3)], mycolor, 'Linewidth',2);
hold on

% if M(i,9)<0; %Sigma 2
%     mycolor = 'b';
%else;
%     mycolor = 'r';
%end;
% plot3([PStart_P2(1) Inv_PEnd_P2(1)], [PStart_P2(2) Inv_PEnd_P2(2)], [PStart_P2(3)
Inv_PEnd_P2(3)], mycolor, 'Linewidth',2);

if M(i,13)<0; %Sigma 3
    mycolor = 'b';
else;
    mycolor = 'r';
end;
plot3([PStart_P3(1) Inv_PEnd_P3(1)], [PStart_P2(2) Inv_PEnd_P3(2)], [PStart_P2(3)
Inv_PEnd_P3(3)], mycolor, 'Linewidth',2);

hold on

%view([140 25]);
view(2);
grid off
%title ('nodes')
xlabel ('X')
ylabel ('Y')
%zlabel ('Z')
axis equal
end;
set(gca, 'visible', 'off');
set(gcf, 'color', 'none');
%set(gca, 'color', 'none');
export_fig('Step174_10x5_Steel_2', '-dpng', '-transparent', '-r300');

```

BIBLIOGRAPHY

BIBLIOGRAPHY

- [1] R. Komanduri and W. R. Reed, "Evaluation of carbide grades and a new cutting geometry for machining titanium alloys," *Wear*, vol. 92, no. 1, pp. 113–123, 1983.
- [2] J. A. G. de Sousa, W. F. Sales, and A. R. Machado, "A review on the machining of cast irons," *Int. J. Adv. Manuf. Technol.*, vol. 94, no. 9, pp. 4073–4092, 2018.
- [3] T. K. Nguyen, *Fundamental tool wear study in turning of Ti-6Al-4V alloy (Ti64) and nano-enhanced minimum quantity lubrication (MQL) milling*. Michigan State University, 2015.
- [4] M. J. Donachie, *Titanium - A Technical Guide*, vol. 99, no. 5. 2000.
- [5] MatWeb, "Titanium Ti-6Al-4V (Grade 5), Annealed Properties." [Online]. Available: <https://asm.matweb.com/search/SpecificMaterial.asp?bassnum=MTP641>. [Accessed: 15-Sep-2019].
- [6] MatWeb, "Aluminum 7075-T6; 7075-T651 Properties." [Online]. Available: <https://asm.matweb.com/search/SpecificMaterial.asp?bassnum=ma7075t6>. [Accessed: 15-Sep-2019].
- [7] MatWeb, "AISI 4340 Steel, annealed, 25 mm round Properties." [Online]. Available: <https://www.matweb.com/search/datasheet.aspx?MatGUID=fd1b43a97a8a44129b32b9de0d7d6c1a>. [Accessed: 15-Sep-2019].
- [8] N. Tsangarakis, "Mode II fracture toughness of 4340 steel," *Eng. Fract. Mech.*, vol. 22, no. 4, pp. 617–624, 1985.
- [9] R. Boyer, G. Welsch, and E. W. Collings, *Materials properties handbook : titanium alloys*. 1994.
- [10] J. C. Williams and G. Lutjering, *Titanium*, vol. 53, no. 9. 2003.
- [11] D. Nguyen, D. Kang, T. Bieler, K. Park, and P. Kwon, "Microstructural impact on flank wear during turning of various Ti-6Al-4V alloys," *Wear*, vol. 384–385, pp. 72–83, 2017.
- [12] M. J. Donachie, *Titanium Alloy Datasheets , Appendix B*. 2000.
- [13] E. O. Ezugwu and Z. M. Wang, "Titanium alloys and their machinability - A review," *J. Mater. Process. Technol.*, 1997.
- [14] P. D. Hartung, B. M. Kramer, and B. F. von Turkovich, "Tool Wear in Titanium Machining," *CIRP Ann. - Manuf. Technol.*, vol. 31, no. 1, pp. 75–80, 1982.
- [15] P. A. Dearnley and A. N. Grearson, "Evaluation of principal wear mechanisms of

- cemented carbides and ceramics used for machining titanium alloy IMI 318,” *Mater. Sci. Technol. (United Kingdom)*, vol. 2, no. 1, pp. 47–58, 1986.
- [16] J. Hua and R. Shivpuri, “A cobalt diffusion based model for predicting crater wear of carbide tools in machining titanium alloys,” *J. Eng. Mater. Technol.*, vol. 127, no. 1, pp. 136–144, 2005.
- [17] L. Jiawei, T. R. Bieler, P. Y. Kwon, R. M. Khawarizmi, J. Molina-Aldareguia, and M. Monclus, “Effect of Crystal Orientation and Cutting Speed on the Local Hardness and Shear Band formation of Ti-6Al-4V Chips using Nanoindentation and EBSD Mapping,” *Submitt. to JOM*, 2022.
- [18] T. B. Britton, H. Liang, F. P. E. Dunne, and A. J. Wilkinson, “The effect of crystal orientation on the indentation response of commercially pure titanium: experiments and simulations,” *Proc. R. Soc. A Math. Phys. Eng. Sci.*, vol. 466, no. 2115, pp. 695–719, 2010.
- [19] T. Nguyen, P. Kwon, D. Kang, and T. R. Bieler, “The Origin of Flank Wear in Turning Ti-6Al-4V,” *J. Manuf. Sci. Eng. Trans. ASME*, vol. 138, no. 12, 2016.
- [20] M. Armendia, A. Garay, L.-M. Iriarte, and P.-J. Arrazola, “Comparison of the machinabilities of Ti6Al4V and TIMETAL® 54M using uncoated WC–Co tools,” *J. Mater. Process. Technol.*, vol. 210, no. 2, pp. 197–203, 2010.
- [21] P. J. Arrazola, A. Garay, L. M. Iriarte, M. Armendia, S. Marya, and F. Le Maître, “Machinability of titanium alloys (Ti6Al4V and Ti555.3),” *J. Mater. Process. Technol.*, vol. 209, no. 5, pp. 2223–2230, 2009.
- [22] R. Komanduri and B. F. Von Turkovich, “New observations on the mechanism of chip formation when machining titanium alloys,” *Wear*, vol. 69, no. 2, pp. 179–188, 1981.
- [23] A. Vyas and M. C. Shaw, “Mechanics of saw-tooth chip formation in metal cutting,” 1999.
- [24] B. Dodd, *Adiabatic Shear Localization: Frontiers and Advances*. 2012.
- [25] R. F. Recht, “Catastrophic thermoplastic shear,” *J. Appl. Mech. Trans. ASME*, vol. 31, no. 2, pp. 189–193, 1964.
- [26] T. Childs, “Adiabatic shearing in metal machining,” *CIRP Encycl. Prod. Eng.*, pp. 27–33, 2014.
- [27] M. H. Miguélez, X. Soldani, and A. Molinari, “Analysis of adiabatic shear banding in orthogonal cutting of Ti alloy,” *Int. J. Mech. Sci.*, vol. 75, pp. 212–222, 2013.
- [28] M. Cotterell and G. Byrne, “Dynamics of chip formation during orthogonal cutting of titanium alloy Ti-6Al-4V,” *CIRP Ann. - Manuf. Technol.*, vol. 57, no. 1, pp. 93–96, 2008.

- [29] A. E. Bayoumi and J. Q. Xie, "Some metallurgical aspects of chip formation in cutting Ti-6wt.%Al-4wt.%V alloy," *Mater. Sci. Eng. A*, vol. 190, no. 1–2, pp. 173–180, 1995.
- [30] S. Sun, M. Brandt, and M. S. Dargusch, "Characteristics of cutting forces and chip formation in machining of titanium alloys," *Int. J. Mach. Tools Manuf.*, vol. 49, no. 7–8, pp. 561–568, 2009.
- [31] A. N. Grearson and P. A. Dearnley, "Evaluation of principal wear mechanisms of carbides and ceramics used for machining," *Mater. Sci. Technol.*, vol. 2, no. January, pp. 47–58, 1986.
- [32] P. A. Dearnley, "New technique for determining temperature distribution in cemented carbide cutting tools," *Met. Technol.*, vol. 10, no. 1, pp. 205–214, 1983.
- [33] R. Li and A. J. Shih, "Spiral point drill temperature and stress in high-throughput drilling of titanium," *Int. J. Mach. Tools Manuf.*, vol. 47, no. 12–13, pp. 2005–2017, 2007.
- [34] A. C. Hoyne, C. Nath, and S. G. Kapoor, "On cutting temperature measurement during titanium machining with an atomization-based cutting fluid spray system," *J. Manuf. Sci. Eng. Trans. ASME*, vol. 137, no. 2, pp. 1–6, 2015.
- [35] D. Schrock, X. Wang, and P. Kwon, "An analysis of the wear of tungsten carbide and polycrystalline diamond inserts turning Ti-6Al-4V," *ASME 2011 Int. Manuf. Sci. Eng. Conf. MSEC 2011*, vol. 1, pp. 197–204, 2011.
- [36] M. Calamaz, D. Coupard, and F. Girot, "A new material model for 2D numerical simulation of serrated chip formation when machining titanium alloy Ti-6Al-4V," *Int. J. Mach. Tools Manuf.*, vol. 48, no. 3–4, pp. 275–288, 2008.
- [37] M. Sima and T. Özel, "Modified material constitutive models for serrated chip formation simulations and experimental validation in machining of titanium alloy Ti-6Al-4V," *Int. J. Mach. Tools Manuf.*, vol. 50, no. 11, pp. 943–960, 2010.
- [38] T. Özel and D. Uluhan, "Prediction of machining induced residual stresses in turning of titanium and nickel based alloys with experiments and finite element simulations," *CIRP Ann. - Manuf. Technol.*, vol. 61, no. 1, pp. 547–550, 2012.
- [39] F. Ducobu, E. Rivière-Lorphèvre, and E. Filippi, "Material constitutive model and chip separation criterion influence on the modeling of Ti6Al4V machining with experimental validation in strictly orthogonal cutting condition," *Int. J. Mech. Sci.*, vol. 107, pp. 136–149, 2016.
- [40] Y. Karpat, "Temperature dependent flow softening of titanium alloy Ti6Al4V: An investigation using finite element simulation of machining," *J. Mater. Process. Technol.*, vol. 211, no. 4, pp. 737–749, 2011.
- [41] P. A. Dearnley, M. Schellewald, and K. L. Dahm, "Characterisation and wear response of metal-boride coated WC-Co," *Wear*, vol. 259, no. 7–12, pp. 861–869, 2005.

- [42] L. N. López De Lacalle, J. Pérez, J. I. Llorente, and J. A. Sánchez, “Advanced cutting conditions for the milling of aeronautical alloys,” *J. Mater. Process. Technol.*, vol. 100, no. 1, pp. 1–11, 2000.
- [43] S. H. I. Jaffery and P. T. Mativenga, “Wear mechanisms analysis for turning Ti-6Al-4V-towards the development of suitable tool coatings,” *Int. J. Adv. Manuf. Technol.*, vol. 58, no. 5–8, pp. 479–493, 2012.
- [44] Z. Liu, Q. An, J. Xu, M. Chen, and S. Han, “Wear performance of (nc-AlTiN)/(a-Si₃N₄) coating and (nc-AlCrN)/(a-Si₃N₄) coating in high-speed machining of titanium alloys under dry and minimum quantity lubrication (MQL) conditions,” *Wear*, vol. 305, no. 1–2, pp. 249–259, 2013.
- [45] K. H. Park, P. Kwon, and D. W. Kim, “Wear characteristic on BAM coated carbide tool in drilling of composite/titanium stack,” *Int. J. Precis. Eng. Manuf.*, vol. 13, no. 7, pp. 1073–1076, 2012.
- [46] D. Nguyen, P. Kwon, V. Voznyuk, and D. Kim, “Performance evaluation of superhard coatings in drilling of Ti-6Al-4V alloy,” *ASME 2017 12th Int. Manuf. Sci. Eng. Conf. MSEC 2017 collocated with JSME/ASME 2017 6th Int. Conf. Mater. Process.*, vol. 4, pp. 1–8, 2017.
- [47] A. S. Varadarajan, P. K. Philip, and B. Ramamoorthy, “Investigations on hard turning with minimal pulsed jet of cutting fluid,” in *Proceedings of the International seminar on Manufacturing Technology beyond*, 2000, pp. 173–179.
- [48] N. N. N. Hamran, J. A. Ghani, R. Ramli, and C. H. C. Haron, “A review on recent development of minimum quantity lubrication for sustainable machining,” *J. Clean. Prod.*, vol. 268, p. 122165, 2020.
- [49] N. R. Dhar, M. T. Ahmed, and S. Islam, “An experimental investigation on effect of minimum quantity lubrication in machining AISI 1040 steel,” *Int. J. Mach. Tools Manuf.*, vol. 47, no. 5, pp. 748–753, 2007.
- [50] Y. K. Hwang and C. M. Lee, “Surface roughness and cutting force prediction in MQL and wet turning process of AISI 1045 using design of experiments,” *J. Mech. Sci. Technol.*, vol. 24, no. 8, pp. 1669–1677, 2010.
- [51] D. A. Stephenson, S. J. Skerlos, A. S. King, and S. D. Supekar, “Rough turning Inconel 750 with supercritical CO₂-based minimum quantity lubrication,” *J. Mater. Process. Technol.*, vol. 214, no. 3, pp. 673–680, 2014.
- [52] M. Sarıkaya and A. Güllü, “Multi-response optimization of minimum quantity lubrication parameters using Taguchi-based grey relational analysis in turning of difficult-to-cut alloy Haynes 25,” *J. Clean. Prod.*, vol. 91, pp. 347–357, 2015.
- [53] T. Nguyen, “FUNDAMENTAL TOOL WEAR STUDY IN TURNING OF Ti-6Al-4V ALLOY (Ti64) AND NANO-ENHANCED MINIMUM QUANTITY LUBRICATION

(MQL) MILLING,” 2015.

- [54] M. K. Gupta, P. K. Sood, and V. S. Sharma, “Optimization of machining parameters and cutting fluids during nano-fluid based minimum quantity lubrication turning of titanium alloy by using evolutionary techniques,” *J. Clean. Prod.*, vol. 135, pp. 1276–1288, 2016.
- [55] S. Sartori, A. Ghiotti, and S. Bruschi, “Solid Lubricant-assisted Minimum Quantity Lubrication and Cooling strategies to improve Ti6Al4V machinability in finishing turning,” *Tribol. Int.*, vol. 118, no. July 2017, pp. 287–294, 2018.
- [56] Di. Nguyen, P. H. Lee, Y. Guo, K. H. Park, and P. Kwon, “Wear Performance Evaluation of Minimum Quantity Lubrication with Exfoliated Graphite Nanoplatelets in Turning Titanium Alloy,” *J. Manuf. Sci. Eng. Trans. ASME*, vol. 141, no. 8, pp. 1–8, 2019.
- [57] C. R. Cunningham, A. Shokrani, and V. Dhokia, “Edge trimming of carbon fibre reinforced plastic,” *Procedia CIRP*, vol. 77, pp. 199–202, 2018.
- [58] N. Geier, J. P. Davim, and T. Szalay, “Advanced cutting tools and technologies for drilling carbon fibre reinforced polymer (CFRP) composites: A review,” *Compos. Part A Appl. Sci. Manuf.*, vol. 125, p. 105552, 2019.
- [59] J. Xu, C. Li, S. Mi, Q. An, and M. Chen, “Study of drilling-induced defects for CFRP composites using new criteria,” *Compos. Struct.*, vol. 201, pp. 1076–1087, 2018.
- [60] A. Faraz, D. Biermann, and K. Weinert, “Cutting edge rounding: An innovative tool wear criterion in drilling CFRP composite laminates,” *Int. J. Mach. Tools Manuf.*, vol. 49, no. 15, pp. 1185–1196, 2009.
- [61] X. Wang, P. Y. Kwon, C. Sturtevant, and J. Lantrip, “Tool wear of coated drills in drilling CFRP,” *J. Manuf. Process.*, vol. 15, no. 1, pp. 127–135, 2013.
- [62] S. Rawat and H. Attia, “Wear mechanisms and tool life management of WC–Co drills during dry high speed drilling of woven carbon fibre composites,” *Wear*, vol. 267, no. 5–8, pp. 1022–1030, 2009.
- [63] M. Henerichs, R. Voß, F. Kuster, and K. Wegener, “Machining of carbon fiber reinforced plastics: Influence of tool geometry and fiber orientation on the machining forces,” *CIRP J. Manuf. Sci. Technol.*, vol. 9, pp. 136–145, Feb. 2015.
- [64] N. K. M. Khairussaleh, C. H. C. Haron, and J. A. Ghani, “Study on wear mechanism of solid carbide cutting tool in milling CFRP,” *J. Mater. Res.*, vol. 31, no. 13, pp. 1893–1899, 2016.
- [65] M. Hagino, T. Inoue, D. U. Department of Material and Environmental Engineering 10-3 Takiharu-cho, Minami-ku, Nagoya 457-8530, Japan, and D. U. Department of Mechanical Engineering 10-3 Takiharu-cho, Minami-ku, Nagoya 457-8530, Japan, “Effect of Carbon Fiber Orientation and Helix Angle on CFRP Cutting Characteristics by End-Milling,” *Int. J. Autom. Technol.*, vol. 7, no. 3, pp. 292–299, Feb. 2013.

- [66] D. Nguyen, M. S. Bin Abdullah, R. Khawarizmi, D. Kim, and P. Kwon, “The effect of fiber orientation on tool wear in edge-trimming of carbon fiber reinforced plastics (CFRP) laminates,” *Wear*, vol. 450, p. 203213, 2020.
- [67] J. L. Merino-Pérez, R. Royer, E. Merson, A. Lockwood, S. Ayvar-Soberanis, and M. B. Marshall, “Influence of workpiece constituents and cutting speed on the cutting forces developed in the conventional drilling of CFRP composites,” *Compos. Struct.*, vol. 140, pp. 621–629, 2016.
- [68] J. L. Merino-Pérez, R. Royer, S. Ayvar-Soberanis, E. Merson, and A. Hodzic, “On the temperatures developed in CFRP drilling using uncoated WC-Co tools Part I: Workpiece constituents, cutting speed and heat dissipation,” *Compos. Struct.*, vol. 123, pp. 161–168, 2015.
- [69] J. L. Merino Perez, A. Hodzic, E. Merson, and S. Ayvar-Soberanis, “Induced thermo-mechanical damage in the drilling of thermoplastic-toughened CFRP composites,” in *Proceedings of*, 2015.
- [70] A. Hodzic, S. Ayvar-Soberanis, E. Merson, and J. L. Merino-Pérez, “The applicability of Taylor’s model to the drilling of CFRP using uncoated WC-Co tools: the influence of cutting speed on tool wear,” *Int. J. Mach. Mach. Mater.*, vol. 16, no. 2, pp. 95–112, 2014.
- [71] N. Feito, A. Diaz-Alvarez, J. L. Cantero, M. Rodriguez-Millan, and H. Miguelez, “Experimental analysis of special tool geometries when drilling woven and multidirectional CFRPs,” *J. Reinf. Plast. Compos.*, vol. 35, no. 1, pp. 33–55, 2016.
- [72] J. Xu, Q. An, X. Cai, and M. Chen, “Drilling machinability evaluation on new developed high-strength T800S/250F CFRP laminates,” *Int. J. Precis. Eng. Manuf.*, vol. 14, no. 10, pp. 1687–1696, 2013.
- [73] W.-C. Chen, “Some experimental investigations in the drilling of carbon fiber-reinforced plastic (CFRP) composite laminates,” *Int. J. Mach. Tools Manuf.*, vol. 37, no. 8, pp. 1097–1108, 1997.
- [74] S. Chand, “Carbon fibers for composites,” *J. Mater. Sci.*, vol. 35, no. 6, pp. 1303–1313, 2000.
- [75] M. G. Huson, “High-performance pitch-based carbon fibers,” *Struct. Prop. High-Performance Fibers*, pp. 31–78, Jan. 2017.
- [76] P. Morgan, *Carbon Fibers and Their Composites*. CRC Press, 2005.
- [77] R. Naslain, “Carbon Fibers From Pan and Pitch,” in *Advanced Inorganic Fibers: Process - Structure - Properties - Applications*, F. T. Wallenberger, R. Naslain, J. B. Macchesney, H. D. Ackler, and F. T. Wallenberger, Eds. Boston, MA: Springer US, 2000, pp. 233–264.
- [78] M. Inagaki, *New carbons-control of structure and functions*. Elsevier, 2000.

- [79] A. Attanasio, M. Gelfi, A. Pola, E. Ceretti, and C. Giardini, "Influence of material microstructures in micromilling of Ti6Al4V alloy," *Materials (Basel)*, vol. 6, no. 9, pp. 4268–4283, 2013.
- [80] O. Hatt, P. Crawforth, and M. Jackson, "On the mechanism of tool crater wear during titanium alloy machining," *Wear*, vol. 374–375, pp. 15–20, 2017.
- [81] J. A. Olortegui-Yume and P. Y. Kwon, "Crater wear patterns analysis on multi-layer coated carbides using the wavelet transform," *Wear*, vol. 268, no. 3–4, pp. 493–504, 2010.
- [82] M. E. Merchant, "Basic Mechanics of the Metal-Cutting Process," *J. Appl. Mech.*, vol. 11, no. 3, pp. A168–A175, 1944.
- [83] A. Molinari, C. Musquar, and G. Sutter, "Adiabatic shear banding in high speed machining of Ti-6Al-4V: Experiments and modeling," *Int. J. Plast.*, vol. 18, no. 4, pp. 443–459, 2002.
- [84] T. W. Wright and H. Ockendon, "Research note: A scaling law for the effect of inertia on the formation of adiabatic shear bands," *Int. J. Plast.*, vol. 12, no. 7, pp. 927–934, 1996.
- [85] R. Pederson, "Microstructure and Phase Transformation of Ti-6Al-4V," pp. 27–30, 2002.
- [86] Y. Cengel and T. M. Heat, "A practical approach," *Second edi*, 2003.
- [87] G. Sridhar, V. V. Kutumbarao, and D. S. Sarma, "The influence of heat treatment on the structure and properties of a near- α titanium alloy," *Metall. Trans. A*, vol. 18, no. 6, pp. 877–891, 1987.
- [88] X. Li *et al.*, "Phase transformation and microstructure evolution of Ti6Al4V-0.55Fe alloy with different initial microstructure during continuous heating," *J. Mater. Res. Technol.*, vol. 18, pp. 1704–1716, 2022.
- [89] F. Ducobu, E. Rivière-Lorphèvre, and E. Filippi, "Numerical contribution to the comprehension of saw-toothed Ti6Al4V chip formation in orthogonal cutting," *Int. J. Mech. Sci.*, vol. 81, pp. 77–87, 2014.
- [90] W. S. Lee and C. F. Lin, "High-temperature deformation behaviour of Ti6Al4V alloy evaluated by high strain-rate compression tests," *J. Mater. Process. Technol.*, vol. 75, no. 1–3, pp. 127–136, 1998.
- [91] D. Umbrello, "Finite element simulation of conventional and high speed machining of Ti6Al4V alloy," *J. Mater. Process. Technol.*, vol. 196, no. 1–3, pp. 79–87, 2008.
- [92] F. Wang, J. Zhao, N. Zhu, and Z. Li, "A comparative study on Johnson-Cook constitutive modeling for Ti-6Al-4V alloy using automated ball indentation (ABI) technique," *J. Alloys Compd.*, vol. 633, pp. 220–228, 2015.
- [93] T. Jain, "Principial Stress Analysis using 3x3 Stress Tensor," *MATLAB Central File*

- Exchange*, 2022. [Online]. Available: <https://www.mathworks.com/matlabcentral/fileexchange/76992-principal-stress-analysis-using-3x3-stress-tensor>. [Accessed: 10-Jun-2021].
- [94] J. Hua and R. Shivpuri, "A cobalt diffusion based model for predicting crater wear of carbide tools in machining titanium alloys," *J. Eng. Mater. Technol. Trans. ASME*, vol. 127, no. 1, pp. 136–144, 2005.
- [95] E. A. Brandes and G. B. Brook, "Smithells Metals Reference Book: Seventh Edition," *Smithells Met. Ref. B. Seventh Ed.*, pp. 1–1800, 2013.
- [96] H. Nakajima, "Diffusion of Cobalt in Single Crystal α -Titanium," vol. 24, no. 10, p. 240, 1983.
- [97] A. Graves *et al.*, "On the mechanism of crater wear in a high strength metastable β titanium alloy," *Wear*, vol. 484–485, no. May, p. 203998, 2021.
- [98] B. Lux, C. Colombier, H. Altena, and K. Stjernberg, "Preparation of alumina coatings by chemical vapour deposition," *Thin Solid Films*, vol. 138, no. 1, pp. 49–64, 1986.
- [99] H. G. Prengel, W. R. Pfouts, and A. T. Santhanam, "State of the art in hard coatings for carbide cutting tools," *Surf. Coatings Technol.*, vol. 102, no. 3, pp. 183–190, 1998.
- [100] T. Polcar and A. Cavaleiro, "High-temperature tribological properties of CrAlN, CrAlSiN and AlCrSiN coatings," *Surf. Coatings Technol.*, vol. 206, no. 6, pp. 1244–1251, 2011.
- [101] N. Canter, "BAM: Antiwear and friction-reducing coating," *Tribol. Lubr. Technol.*, vol. 65, no. 3, p. 14, 2009.
- [102] M. Lępicka and M. Grldzka-Dahlke, "The initial evaluation of performance of hard anti-wear coatings deposited on metallic substrates: Thickness, mechanical properties and adhesion measurements - A brief review," *Rev. Adv. Mater. Sci.*, vol. 58, no. 1, pp. 50–65, 2019.
- [103] B. A. Cook, J. L. Haringa, T. L. Lewis, A. M. Russell, and Y. Lee, "Processing studies and selected properties of ultra-hard AlMgB14," *J. Adv. Mater.*, vol. 36, no. 3, pp. 56–63, 2004.
- [104] M. Bar-Hen and I. Etsion, "Experimental study of the effect of coating thickness and substrate roughness on tool wear during turning," *Tribol. Int.*, vol. 110, pp. 341–347, 2017.
- [105] R. M. Khawarizmi, J. Lu, D. S. Nguyen, T. R. Bieler, and P. Kwon, "The Effect of Ti-6Al-4V Microstructure, Cutting Speed, and Adiabatic Heating on Segmented Chip Formation and Tool Life," *JOM*, vol. 74, no. 2, pp. 526–534, 2022.
- [106] S.-H. Lee, I.-H. Ko, and T.-Y. Kim, "Surface failure analysis of AlCrN coating on WC substrate subjected to high-temperature oxidation in glass-molding machine," *Appl. Surf.*

- Sci.*, vol. 452, pp. 210–216, 2018.
- [107] H. Okamoto, “Cr-Ti (chromium-titanium),” *J. Phase Equilibria*, vol. 4, no. 23, pp. 382–383, 2002.
- [108] M. Enomoto, “The Si-Ti-V system (silicon-titanium-vanadium),” *J. phase equilibria*, vol. 13, no. 2, pp. 201–205, 1992.
- [109] J. L. Murray, “The Ti– Zr (Titanium-Zirconium) system,” *Bull. Alloy Phase Diagrams*, vol. 2, no. 2, pp. 197–201, 1981.
- [110] H. Nakajima and M. Koiwa, “Diffusion in Titanium,” *ISIJ International*, vol. 31, no. 8, pp. 757–766, 1991.
- [111] S. V. Divinski, F. Hisker, T. Wilger, M. Friesel, and C. Herzig, “Tracer diffusion of boron in α -Ti and γ -TiAl,” *Intermetallics*, vol. 16, no. 2, pp. 148–155, 2008.
- [112] J. F. Shackelford and W. Alexander, *CRC materials science and engineering handbook*. CRC press, 2000.
- [113] L. Aihua, D. Jianxin, C. Haibing, C. Yangyang, and Z. Jun, “Friction and wear properties of TiN, TiAlN, AlTiN and CrAlN PVD nitride coatings,” *Int. J. Refract. Met. Hard Mater.*, vol. 31, pp. 82–88, 2012.
- [114] C.-S. Chen, C.-P. Liu, C.-Y. Tsao, and H.-G. Yang, “Study of mechanical properties of PVD ZrN films, deposited under positive and negative substrate bias conditions,” *Scr. Mater.*, vol. 51, no. 7, pp. 715–719, 2004.
- [115] N. H. Cook and P. N. Nayak, “The thermal mechanics of tool wear,” *J. Manuf. Sci. Eng. Trans. ASME*, vol. 88, no. 1, pp. 93–110, 1966.
- [116] P. S. Sreejith and B. K. A. Ngoi, “Dry machining: Machining of the future,” *J. Mater. Process. Technol.*, vol. 101, no. 1, pp. 287–291, 2000.
- [117] B. Davoodi and A. H. Tazehkandi, “Experimental investigation and optimization of cutting parameters in dry and wet machining of aluminum alloy 5083 in order to remove cutting fluid,” *J. Clean. Prod.*, vol. 68, pp. 234–242, 2014.
- [118] A. Attanasio, M. Gelfi, C. Giardini, and C. Remino, “Minimal quantity lubrication in turning: Effect on tool wear,” *Wear*, vol. 260, no. 3, pp. 333–338, 2006.
- [119] Ç. V. Yıldırım, M. Sarıkaya, T. Kıvak, and Ş. Şirin, “The effect of addition of hBN nanoparticles to nanofluid-MQL on tool wear patterns, tool life, roughness and temperature in turning of Ni-based Inconel 625,” *Tribol. Int.*, vol. 134, no. December 2018, pp. 443–456, 2019.
- [120] N. Talib, H. Sasahara, and E. A. Rahim, “Evaluation of modified jatropha-based oil with hexagonal boron nitride particle as a biolubricant in orthogonal cutting process,” *Int. J.*

- Adv. Manuf. Technol.*, vol. 92, no. 1–4, pp. 371–391, 2017.
- [121] U. M. R. Paturi, Y. R. Maddu, R. R. Maruri, and S. K. R. Narala, “Measurement and Analysis of Surface Roughness in WS₂ Solid Lubricant Assisted Minimum Quantity Lubrication (MQL) Turning of Inconel 718,” *Procedia CIRP*, vol. 40, pp. 138–143, 2016.
- [122] Y. Zhang, C. Li, D. Jia, D. Zhang, and X. Zhang, “Experimental evaluation of MoS₂ nanoparticles in jet MQL grinding with different types of vegetable oil as base oil,” *J. Clean. Prod.*, vol. 87, no. C, pp. 930–940, 2015.
- [123] A. Uysal, F. Demiren, and E. Altan, “Applying Minimum Quantity Lubrication (MQL) Method on Milling of Martensitic Stainless Steel by Using Nano MoS₂ Reinforced Vegetable Cutting Fluid,” *Procedia - Soc. Behav. Sci.*, vol. 195, pp. 2742–2747, 2015.
- [124] W. Z. Teo, E. L. K. Chng, Z. Sofer, and M. Pumera, “Cytotoxicity of exfoliated transition-metal dichalcogenides (MoS₂, WS₂, and WSe₂) is lower than that of graphene and its analogues,” *Chem. Eur. J.*, vol. 20, no. 31, pp. 9627–9632, 2014.
- [125] O. Hatt, H. Larsson, F. Giuliani, P. Crawforth, B. Wynne, and M. Jackson, “Predicting Chemical Wear in Machining Titanium Alloys Via a Novel Low Cost Diffusion Couple Method,” *Procedia CIRP*, vol. 45, pp. 219–222, 2016.
- [126] R. M. A. N. D. Tomashov and G. P. Chernova, “Passivity and Corrosion Resistance of Titanium and Its Alloy,” *J. Electrochem. Soc.*, vol. 108, p. 113, 1961.
- [127] N. S. K. R. and M. Nouari, “The influence of solid lubricant for improving tribological properties in turning process,” *Lubr. Sci.*, vol. 23, pp. 49–59, 2011.
- [128] B. Podgornik, T. Kosec, A. Kocijan, and Donik, “Tribological behaviour and lubrication performance of hexagonal boron nitride (h-BN) as a replacement for graphite in aluminium forming,” *Tribol. Int.*, vol. 81, pp. 267–275, 2015.
- [129] S. Swan, T. Yuksel, D. Kim, and H. Gurocak, “Automation of the vacuum assisted resin transfer molding process for recreational composite yachts,” *Polym. Compos.*, vol. 38, no. 11, pp. 2411–2424, 2017.
- [130] S.-Y. Kim, C. S. Shim, C. Sturtevant, and H. C. Song, “Mechanical properties and production quality of hand-layup and vacuum infusion processed hybrid composite materials for GFRP marine structures,” *Int. J. Nav. Archit. Ocean Eng.*, vol. 6, no. 3, pp. 723–736, 2014.
- [131] A. Hammami and B. R. Gebart, “Analysis of the vacuum infusion molding process,” *Polym. Compos.*, vol. 21, no. 1, pp. 28–40, 2000.
- [132] J. Ahmad, “Introduction to polymer composites,” in *Machining of Polymer Composites*, Springer, 2009, pp. 1–35.
- [133] Toray Composite Materials America, “T300 Standard Modulus Carbon Fibers,” *J. Fiber*

Sci. Technol., 2018.

- [134] Hexcel, “HexTow ® IM7 Product Data Sheet,” vol. 000, pp. 1–2, 2016.
- [135] M. Information, P. Information, G. Properties, M. Properties, T. Properties, and E. Properties, “MITSUBISHI DIALEAD™ K13312,” pp. 1–2, 2019.
- [136] R. Zitoune, V. Krishnaraj, B. Sofiane Almabouacif, F. Collombet, M. Sima, and A. Jolin, “Influence of machining parameters and new nano-coated tool on drilling performance of CFRP/Aluminium sandwich,” *Compos. Part B Eng.*, vol. 43, no. 3, pp. 1480–1488, Mar. 2012.
- [137] S. Swan, M. S. Bin Abdullah, D. Kim, D. Nguyen, and P. Kwon, “Tool wear of advanced coated tools in drilling of CFRP,” *J. Manuf. Sci. Eng. Trans. ASME*, vol. 140, no. 11, 2018.
- [138] D. Nguyen, V. Voznyuk, M. S. Bin Abdullah, D. Kim, and P. Y. Kwon, “Tool wear of superhard ceramic coated tools in drilling of CFRP/Ti stacks,” in *International Manufacturing Science and Engineering Conference*, 2019, vol. 58752, p. V002T03A089.
- [139] L. S. Lasdon, A. D. Waren, A. Jain, and M. Ratner, “Design and Testing of a Generalized Reduced Gradient Code for Nonlinear Programming,” *ACM Trans. Math. Softw.*, vol. 4, no. 1, pp. 34–50, 1978.
- [140] P. Kwon and R. Kountanya, “Experimental observations on flank wear in machining spherodized plain carbon steels,” *Tribol. Trans.*, vol. 42, no. 2, pp. 265–272, 1999.
- [141] J. Flöck, K. Friedrich, and Q. Yuan, “On the friction and wear behaviour of PAN-and pitch-carbon fiber reinforced PEEK composites,” *Wear*, vol. 225, pp. 304–311, 1999.
- [142] M. Ramulu, D. Kim, and G. Choi, “Frequency analysis and characterization in orthogonal cutting of glass fiber reinforced composites,” *Compos. Part A Appl. Sci. Manuf.*, vol. 34, no. 10, pp. 949–962, 2003.
- [143] Y. Xie, L. Lu, Z. Hou, Y. Tang, L. Miao, and X. Liu, “Fracture behavior of PAN-based carbon fiber tow in a chopping process on an elastic support,” *Fibers Polym.*, vol. 17, no. 8, pp. 1262–1268, 2016.
- [144] H. Hocheng, *Machining technology for composite materials: principles and practice*. Elsevier, 2011.